Observation of new Ξ_c^0 states decaying to $\Lambda_c^+ K^-$, and development of the TORCH time-of-flight detector.

Emmy Pauline Maria Gabriel

Doctor of Philosophy
The University of Edinburgh
2 March 2020

Abstract

Using a data sample of proton-proton collisions at center-of-mass energy of 13 TeV corresponding to an integrated luminosity of 5.6 fb^{-1} collected by the LHCb experiment, the $\Lambda_c^+ K^-$ mass spectrum is studied. Three new, excited Ξ_c^0 states are observed and their masses and natural widths are measured to be

$$\begin{aligned} m(\Xi_c(2923)^0) &= 2923.04 \pm 0.25 \pm 0.18 \pm 0.14\,\mathrm{MeV}, \\ \Gamma(\Xi_c(2923)^0) &= 7.09 \pm 0.79 \pm 1.39\,\mathrm{MeV}, \\ \\ m(\Xi_c(2939)^0) &= 2938.55 \pm 0.21 \pm 0.17 \pm 0.14\,\mathrm{MeV}, \\ \Gamma(\Xi_c(2939)^0) &= 10.22 \pm 0.77 \pm 1.04\,\mathrm{MeV}, \\ \\ m(\Xi_c(2965)^0) &= 2964.88 \pm 0.26 \pm 0.14 \pm 0.14\,\mathrm{MeV}, \\ \Gamma(\Xi_c(2965)^0) &= 14.07 \pm 0.91 \pm 1.34\,\mathrm{MeV}, \end{aligned}$$

where the uncertainties are statistical, systematic and the third one is due to the knowledge of the Λ_c^+ mass. All peaks have significances greatly exceeding 5σ. Though the mass of $\Xi_c(2965)^0$ is close to the known $\Xi_c(2970)^0$, its natural width differs significantly and therefore it is interpreted as a different baryon.

Furthermore, this thesis summarises the status of the TORCH time-of-flight detector by describing the characterisation of Micro-Channel Plate Photomultiplier tubes (MCP-PMTs), outlining the recent beam test campaigns as well as an analysis comparing the photon yield in simulation and data.

Lay Summary

The Standard Model is the theory which, to our current knowledge, best describes the fundamental particles that make up our universe along with their interactions. The spectrum of ground state particles has long been theorised in the quark model and most of the expected particles have been confirmed experimentally. Ground state particles can reach excited states in which they are in a higher energy level. In the last decades, a plethora of excited particles have been found at high energy particle physics experiments. This has lead to an upsurge in both theoretical and experimental interest, where both communities work hand in hand to understand excited particles.

The LHCb experiment, at the Large Hadron Collider at CERN, was built to perform heavy flavour physics measurements. The research presented in this thesis uses data collected by the LHCb detector in 2016 to 2018 to search for new heavy baryons containing a charm quark.

Particle detector upgrades are imperative to keep pushing the boundaries of experimental physics. The second half of this thesis describes the status of the TORCH time-of-flight detector, which will be installed as a subdetector in the LHCb experiment within the next decade. The TORCH detector helps to differentiate between particle species.

Declaration

I declare that this thesis was composed by myself, that the work contained herein is my own except where explicitly stated otherwise in the text, and that this work has not been submitted for any other degree or professional qualification except as specified.

(*Emmy Pauline Maria Gabriel, 2 March 2020*)

Acknowledgements

I would like to start by thanking my supervisor Franz Muheim for his feedback and guidance throughout my PhD. I would also like to thank my second supervisor Matt Needham for his help, particularly during the first year of my PhD when I was working on the $B_s^0 \to \phi\phi$ analysis. Furthermore, I would like to thank Thierry Gys for his supervision while I was on LTA working for the TORCH collaboration. His patience and guidance in the laboratory and during beam tests were incredibly valued. And to Marco Pappagallo, I would like to say thank you for introducing me to spectroscopy and teaching me an incredible amount during the final year of my PhD. Finally, I am grateful to the members of the BnoC working group, the Charm working group and the TORCH collaboration for the many fruitful discussions.

Thanks must go to CERN, the LHCb collaboration, the University of Edinburgh and SUPA for the resources and funding to make the past 3.5 years happen.

I would like to thank my friends, ones I made in Edinburgh, LTA friends and friends from before I started my PhD, for always providing a listening ear when I needed one. And finally, my parents and my brother deserve all my gratitude for always supporting me.

Contents

List of Figures

List of Tables

Chapter 1

Introduction

To our current knowledge, the Standard Model (SM) best describes the elementary particles that make up our universe along with their interactions. The quark model has been well established and mostly confirmed experimentally to describe the spectrum of ground state particles. The spectra of excited particles are still largely unknown due to the theoretical difficulty to predict these states, and hence there are many questions to be answered. In the last decades, a plethora of excited particles have been found at high energy particle physics experiments. This has lead to a boom in both theoretical and experimental interest, where both communities work alongside each other to understand excited particles. The research presented in this thesis uses heavy flavour physics data collected by the LHCb experiment to search for excited charmed baryons.

Chapter 2 gives an overview of the theoretical background behind the physics analysis described in this thesis. The SM is described, along with the quark model. Furthermore, single charmed baryons, which are the topic of the analysis presented in this thesis, are introduced. The data analysed have been taken by the LHC detector at the Large Hadron Collider at CERN. In Chapter 3 the LHCb detector is described in more detail.

The next three chapters focus on the search for excited Ξ_c^0 particles decays to the $\Lambda_c^+ K^-$ final state. Chapter 4 describes the current experimental status of searches for excited Ξ_c^0 particles. Recent searches by the Belle and Babar collaborations are discussed. Chapters 5 and 6 detail the analysis performed. In the first chapter, the selection requirements in the analysis are discussed. Consequently, the observation of several excited Ξ_c^0 baryons is described in chapter 6, which concludes with a discussion of the results.

The second part of this thesis focuses on detector development. Particle detector upgrades are imperative to keep pushing the boundaries of experimental physics. Chapter 7 outlines the design of the TORCH time-of-flight detector along with the physics it is based on. In chapter 8, the laboratory work performed as part of this thesis is described in detail. Furthermore, a summary of recent beam test campaigns is given. Finally, chapter 9 details the photon counting analysis of the data taken in several beam test campaigns. The studies described in these chapters has been published by the TORCH collaboration [1].

Concluding remarks on the research presented in this thesis is given in chapter 10.

In addition to the studies presented in this thesis, I have performed integral work on the analysis on $B_s^0 \to \phi\phi$ decays [2]. A brief summary of my work can be found in App. C.

Chapter 2

Theory

The aim of this chapter is to introduce the theoretical framework surrounding baryon spectroscopy. The analysis described later in this thesis discusses the observation of excited $\mathit{\Xi}_c^0$ resonances, hereafter referred to as Ξ_c^{**0}, in the $\Lambda_c^+K^-$ mass spectrum as detailed in Chapters 4, 5 and 6. Therefore the focus of this chapter is the theory of charmed baryons.

First, a brief overview of the Standard Model (SM) of particle physics is given, including an introduction to group theory relevant to the SM. Secondly, the quark model is discussed to explain the expected spectrum of ground state mesons and baryons. The ground state singly charmed baryons are discussed in detail. Finally, we look into the spectrum of excited states, specifically excited $\mathit{\Xi}_c^0$ states.

2.1 The Standard Model of particle physics

The Standard Model of particle physics is a theoretical framework used to describe three of the four fundamental forces in the universe, as well as organising all known elementary particles and their interactions. The three fundamental forces described by this model are the electromagnetic force, as well as the weak and the strong force. The gravitational force, which is negligible on the scale of fundamental particle physics, is not included in the SM.

The elementary particles in the SM consist of six quarks, six leptons, four gauge bosons and the Higgs boson. To our knowledge, elementary particles cannot be divided into smaller constituents. Composite particles are made up of several elementary particles. The elementary particles can be divided into bosons and fermions, depending on their spin. Bosons have integer spin, and describe the elementary particles that govern the fundamental forces. Fermions have half-integer spin and are the elementary constituents of matter. These particle groups behave differently. The Pauli exclusion principle holds in Fermi-Dirac statistics, preventing multiple particles to be in the same quantum state. Bosons adhere to Bose-Einstein statistics, where such a restriction is not imposed. These restrictions imply that the wave function for fermions is anti-symmetric under the interchange of two identical particles, whereas the boson wave function is symmetric under this interchange. Every type of particle has an antiparticle of equal mass, but with reversed additive quantum numbers, i.e. the charge, Q, lepton number, $\mathcal{L}$, and baryon number, $\mathcal{B}$, are reversed. The spin is a vector quantity and thus remains unchanged.

Fermions are further divided into quarks and leptons, where quarks undergo strong interactions and fermions are not affected by the strong force. Table 2.1 summarises the fermions in the SM, along with their electric charge (in units of e), their spin, the most up to date mass measurement average and the forces they interact with, where S represents the strong force, W is the weak force and the electromagnetic force is indicated by EM. The uncertainties on the quark masses are relatively large, since they are hard to measure. This is because quarks only appear in bound states, called hadrons, through a process known as hadronisation. Hadrons are classified according to their baryon number, $\mathcal{B}$. The most common particles are mesons, which consist of a $q\bar{q}$ pair and have baryon number $\mathcal{B} = 0$, and (anti-) baryons which consists of three (anti-) quarks with baryon number $\mathcal{B} = 1$ ($\mathcal{B} = -1$). More complex states consisting of more quarks are possible, such as pentaquarks, ($q\bar{q}qqq$) which have been observed by the LHCb collaboration [3].

Table 2.1 also lists three generations for both the quarks and the leptons. Quarks in the same generation are much more likely to interact with each other than an interaction between generations. The same rule holds for the leptons. Every quark generation contains an ‘up’-type quark with electric charge $Q = +2/3$ and a ‘down’-type quark with charge $Q = -1/3$. The likelihood of quark flavour changes, governed by the weak force, is given by the matrix elements in the

Table 2.1 *A summary of the properties of fermions, where the quarks are given in the top section of the table, and the leptons in the bottom. The masses are taken from the PDG [6], where the top quark mass measurement only considers direct measurements.*

Name	Charge (e)	Mass (MeV/c^2)	Forces	Generation
up	+2/3	$2.16^{+0.49}_{-0.26}$	S,W,EM	1
down	-1/3	$4.67^{+0.48}_{-0.17}$	S,W,EM	1
charm	+2/3	1270 ± 20	S,W,EM	2
strange	-1/3	93^{+11}_{-5}	S,W,EM	2
top	+2/3	172900 ± 400	S,W,EM	3
bottom	-1/3	4180^{+30}_{-20}	S,W,EM	3
electron	-1	0.51 ± 0.00	W,EM	1
electron neutrino	0	< 0.000002	W	1
muon	-1	105.66 ± 0.00	W,EM	2
muon neutrino	0	< 0.19	W	2
tau	-1	1776.86 ± 0.12	W,EM	3
tau neutrino	0	< 18.2	W	3

Cabbibo-Kobayashi-Maskawa matrix,

$$V_{CKM} \equiv \begin{pmatrix} V_{ud} & V_{us} & V_{ub} \\ V_{cd} & V_{cs} & V_{cb} \\ V_{td} & V_{ts} & V_{tb} \end{pmatrix}, \tag{2.1}$$

where the diagonal matrix elements describing the interactions within each generation have a magnitude close to one. The leptons have a similar generation structure, where each lepton particle (electron, muon and tau) has a neutral light neutrino partner. Lepton flavour changes are not allowed in the SM, but searches for lepton flavour universality violation are being performed, for example at LHCb [4, 5].

Table 2.2 lists the four gauge bosons and the Higgs boson, along with their electric charge and mass. The gauge bosons are force mediators. The strong force is governed by gluons. Photons carry electromagnetism, and the weak force is governed by the W- and Z-boson.

Table 2.2 *A summary of the properties of bosons, where the gauge bosons are given in the top section of the table, and the Higgs boson in the bottom. The masses are taken from the PDG [6].*

Name	Charge (e)	Spin	Mass (MeV/c^2)	Forces
gluon	0	1	0	S
photon	0	1	$< 1 \times 10^{-24}$	EM
W-boson	± 1	1	80379 ± 12	W
Z-boson	0	1	91187.6 ± 2.1	W
Higgs boson	0	0	125100 ± 140	-

2.2 Group theory

The SM theory can be described in a very minimalist and elegant way using group theory. A brief introduction to group theory is given, loosely based on the explanation in [7], after which a group theory perspective of the SM is described.

A group is comprised of a finite or infinite number of elements $G = \{g_1, g_2, ...\}$ with an operation $\diamond$. The group elements adhere to a certain set of axioms:

- *Closure*: If g_1, $g_2 \in G$, then $g_1 \diamond g_2 \in G$.
- *Identity*: $\exists\ I \in G$ such that $I \diamond g_i = g_i\ \forall\ g_i \in G$.
- *Inverse*: Every $g_i \in G$ has a $g_i^{-1} \in G$ such that $g_i \diamond g_i^{-1} = I$.
- *Associativity*: If $g_1, g_2, g_3 \in G$, then $(g_1 \diamond g_2) \diamond g_3 = g_1 \diamond (g_2 \diamond g_3)$.

An example of a simple group is all integers with addition as the group operation. A group is abelian if $g_1 \diamond g_2 = g_2 \diamond g_1$.

In particle physics, a group is typically made up of a set of transformations, described by a set of complex matrices where the group operation is matrix multiplication. As a result of group theory mathematics, every group G can be represented by a set of matrices, called the *representation* of the group. For every $g_i \in G$, there exists a matrix M_g such that $g_1 \diamond g_2 = g_3$ implies that $M_{g_1} M_{g_2} = M_{g_3}$. Some noteworthy properties of representations are:

- Representations are not unique in the sense that a given group G has infinitely many representations.

- Representations are not by default faithful. A faithful representation means there is a one-to-one correspondence between the group elements and the representation matrices.
- A group of matrices is a faithful representation of itself, called the fundamental representation.
- It is straightforward to generate infinitely many representations by combining two representations of the same group into a new one. Any non-redundant set of matrices that can represent a group is called the irreducible representation.

A *Lie group* is a group in which the group elements are smooth (continuous and differentiable) functions of some finite set of parameters $\theta_a \in \mathbb{R}$ and in which $\diamond$ depends smoothly on those parameters. More rigorously, this implies that

- If $g \in G$, g is a function of θ_i as $g = g(\theta_1, ..., \theta_N) = \exp[i\theta_a T^a] = \exp[i\vec{\theta} \cdot \vec{T}]$ where $a = 1, ..., N$ and $\{\theta_a\}$ are continuous parameters.

Here, the T^a's are the *generators* of the group. There are N generators, and if you know all of them it is possible to generate all elements of G. Thus, the generators carry all relevant information about the group in a very concise manner.

Nearly all of the important symmetry groups in particle physics are Lie groups, most notably the unitary and orthogonal groups. Several examples of Lie groups in particle physics are given in Tab. 2.3, some of which are discussed in more detail in the next section, where the SM is explained in the context of group theory.

2.2.1 A group theory perspective of the Standard Model

Particle interactions can be seen as rotations belonging to a group, depending on the force that governs them. This is depicted in Fig. 2.1, and explained in more detail in this subsection.

Particle interactions induced by the electromagnetic force are described using quantum electrodynamics (QED). The rules governing QED require a $U(1)$ gauge symmetry. This is the simplest gauge symmetry. An example of

Table 2.3 *Lie groups in particle physics.*

Group	Property	Example
U(n)	n×n unitary matrices ($U^\dagger U = 1$)	U(1) electromagnetism
SU(n)	n×n unitary matrices ($U^\dagger U = 1$) with det $U = 1$	SU(2) weak interactions SU(3) strong interactions
O(n)	n×n orthogonal matrices ($O^T O = 1$)	O(3) rotations and reflections
SO(n)	n×n orthogonal matrices ($O^T O = 1$) with det $O = 1$	SO(3) rotations

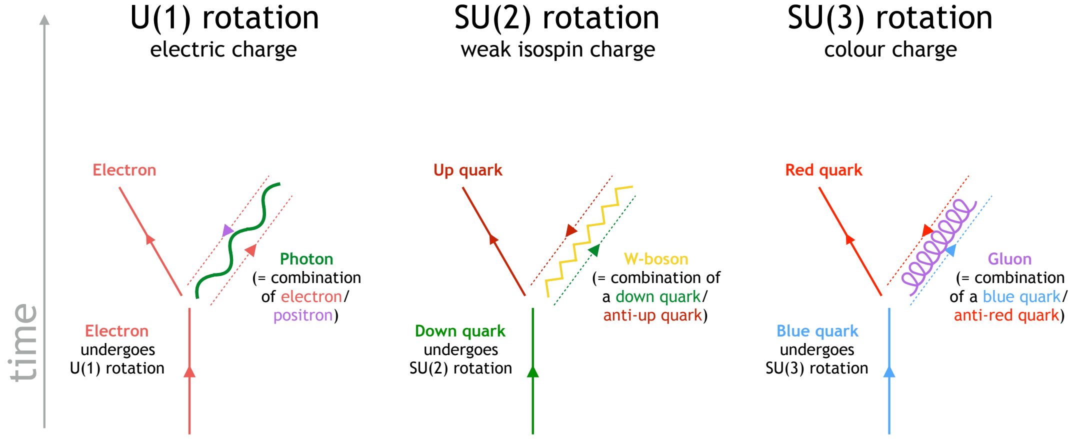

Figure 2.1 *Depiction of the $U(1)$, $SU(2)$ and $SU(3)$ rotations described by the electromagnetic, weak and strong forces, respectively, in the SM.*

an electromagnetic interaction is an electron emitting a boson, which can equivalently be described as an electron undergoing a $U(1)$ transformation. A $U(1)$ transformation is mathematically described as a simple rotation, with elements of the form $e^{i\theta}$ where $\theta \in \mathbb{R}$ and the group operation is multiplication. The Lagrangian is required to be invariant under such rotations. Lagrangian invariance gives rise to conserved quantities following Noether's theorem, such that the global electromagnetic $U(1)$ gauge symmetry gives rise to electric charge conservation, and the local gauge symmetry indicates the need for a massless mediator boson. Consequently, we find that the electromagnetic force is mediated through photons and all charged particles can interact electromagnetically.

The next Lie group required to understand the SM is the $SU(2)$ group. There are several $SU(2)$ groups in the SM. The most important ones will be discussed here. In group theory, the $SU(2)$ group is a special unitary group of dimension two, described by 2 × 2 hermitian, traceless matrices, as shown in Tab. 2.3. One of the $SU(2)$ transformations induces quark flavour changes, i.e. an up-quark can transform into a down-quark by undergoing an $SU(2)$ transformation. The only fundamental force allowed to transform a quarks flavour is the weak force, which gives us an indication that $SU(2)$ describes weak interactions. In addition, this is the only force that allows neutrinos to interact. It is mediated by W- and Z-bosons. The weak force has an interaction strength much smaller than the other two fundamental forces, but due to its unique properties it is no less important.

The "charge" of the weak $W^{\pm}$ interaction is described by the weak isospin (T), quantised along the T_3 axis. Left-handed fermions, which have negative helicity, are chosen to have $T = +1/2$. Helicity is defined as the sign of the spin vector of a particle projected on its momentum vector. In this description, left-handed neutrinos and 'up'-type quarks have $T_3 = +1/2$ and left-handed fermions and 'down'-type quarks have $T_3 = -1/2$. Right-handed fermions, which have positive helicity, have $T = 0$. This theory leads to a suppression of interactions with right-handed massive fermions, and is denoted as $SU(2)_L$. The weak isospin symmetry is exact. The generators of this group are the 2 × 2 Pauli matrices, given in Eq. 2.2.

$$\sigma_1 = \begin{pmatrix} 0 & 1 \\ 1 & 0 \end{pmatrix}, \quad \sigma_2 = \begin{pmatrix} 0 & -i \\ i & 0 \end{pmatrix}, \quad \sigma_3 = \begin{pmatrix} 1 & 0 \\ 0 & -1 \end{pmatrix} \tag{2.2}$$

These act on so-called 2-component spinors to transform them as follows:

$$\sigma_i \begin{pmatrix} u_L \\ d_L \end{pmatrix} \rightarrow \begin{pmatrix} u_L^{'} \\ d_L^{'} \end{pmatrix} \tag{2.3}$$

The equation above transforms a flavour doublet consisting of a left-handed up-quark and a left-handed down-quark, from now on referred to as the flavour doublet. There exists another doublet, consisting of a left-handed neutrino and its left-handed lepton counterpart. Since right-handed particles do not interact weakly, they form singlets in this theory.

The electromagnetic and weak forces are unified in an electroweak gauge theory described by the groups $SU(2)_L \times U(1)_Y$. Here, $U(1)_Y$ the Y subscript denotes the hypercharge, a quantum number defined as $Y = 2(Q - T_3)$, linking the electric charge Q and the weak isospin (T, T_3).

There is another SU(2) group in particle physics, describing the strong isospin (I) symmetry. This symmetry is broken. Within this symmetry, up and down quarks have $I = 1/2$, where the up quark has $I_3 = +1/2$ and the down quark has $I_3 = -1/2$. All other quarks have $I = 0$ and thus also $I_3 = 0$. Hadrons have strong isospin $I_3 = 1/2(n_u - n_d)$ where n_u is the number of up quarks in the hadron and n_d denoted the number of down quarks. This allows for particles with the same quark content, but different strong isospin quantum numbers, depending on whether the isospin values of the constituents are flavour aligned or have opposite flavour directions, leading to isospin multiplets.

Now that we have a description of the weak and electromagnetic force in the SM, let us consider the strong force. The gluon is the mediator of the strong force. The strong force describes interactions between all colour charged particles, the quarks. The strong interactions are described by a theory called quantum chromodynamics (QCD). This is similar to QED since it acts on charged particles by exchange of a massless boson. However, colour charge comes in three varieties: red, R, green, G, and blue, B. Thus, the theory requires an $SU(3)$ group. The $SU(3)$ colour group, denoted $SU(3)_C$, has 8 generators, required to be 3×3 hermitian, traceless matrices. The generators, T_a, are described using the Gell-Mann matrices, λ_a, as $T_a = \lambda_a/2$. The Gell-Mann matrices are given by

$$\lambda_i = \begin{pmatrix} & \sigma_i & & 0 \\ & & & 0 \\ 0 & & 0 & 0 \end{pmatrix} \text{ for } i = 1,2,3; \quad \lambda_4 = \begin{pmatrix} 0 & 0 & 1 \\ 0 & 0 & 0 \\ 1 & 0 & 0 \end{pmatrix}; \quad \lambda_5 = \begin{pmatrix} 0 & 0 & -i \\ 0 & 0 & 0 \\ i & 0 & 0 \end{pmatrix};$$

$$\lambda_6 = \begin{pmatrix} 0 & 0 & 0 \\ 0 & 0 & 1 \\ 0 & 1 & 0 \end{pmatrix}; \quad \lambda_7 = \begin{pmatrix} 0 & 0 & 0 \\ 0 & 0 & -i \\ 0 & i & 0 \end{pmatrix}; \quad \lambda_8 = \frac{1}{\sqrt{3}} \begin{pmatrix} 1 & 0 & 0 \\ 0 & 1 & 0 \\ 0 & 0 & -2 \end{pmatrix}. \tag{2.4}$$

This notation makes it easy to see that $SU(2)$ group generated by the Pauli matrices forms a subgroup of $SU(3)$.

In the $SU(3)_C$ symmetry, every gluon has a colour and an anti-colour and can be grouped in an octet and a singlet as

$$\mathbf{3} \otimes \bar{\mathbf{3}} = \mathbf{8} \oplus \mathbf{1}, \tag{2.5}$$

where **3** defines the three colours, and $\bar{\mathbf{3}}$ describes the three anti-colours. The right hand side of this equation, $\mathbf{8} \oplus \mathbf{1}$, represents the two irreducible representations of this group. Naively, one would expect there to be nine gluons that interact in strong interactions. However, due to mathematical restrictions that require linear independence of the generator matrices, we get eight coloured gluons in addition to one colourless, completely symmetric singlet which cannot participate in QCD interactions. The eight coloured gluons are:

$$R\bar{B}, R\bar{G}, G\bar{B}, G\bar{R}, B\bar{G}, B\bar{R}, \frac{1}{\sqrt{2}}(R\bar{R} - G\bar{G}), \frac{1}{\sqrt{6}}(R\bar{R} + G\bar{G} - 2B\bar{B}) \qquad (2.6)$$

and the colourless singlet is $\frac{1}{\sqrt{3}}(R\bar{R} + G\bar{G} + B\bar{B})$. The method to calculate the multiplets is further detailed in the next section for the $SU(3)_F$ flavour symmetry group of the three lightest quarks, as shown in Fig. 2.2. Note that the $SU(3)_C$ symmetry is exact and thus forms a gauge symmetry.

Combining all the information in this section, the Standard Model can be described as

$$SU(3)_C \times SU(2)_L \times U(1)_Y. \qquad (2.7)$$

2.3 The quark model

As mentioned in the previous section, quarks are confined to bound states, called hadrons. This is a consequence of QCD. The expected spectrum of ground state mesons and baryons can be described using the constituent quark model. This section describes the classification of baryons according to the constituent quark model. However, this is not an exact model since it neglects the fact that baryons are not pure 3-quark objects. In addition, mixing of states with the same conserved quantum numbers is not included. Nevertheless, it has been proven that this model yields a fairly accurate description of the ground state baryons. Several models exist to predict the spectrum of excited baryons. One of these models used to describe the excited states is the heavy quark effective theory. This is further discussed in Sec. 2.4.2.

Mesons

Light mesons, made up of u, d and s quarks follow a $SU(3)$ flavour symmetry, denoted $SU(3)_F$, which can be grouped in an octet and a singlet as follows:

$$\mathbf{3} \otimes \bar{\mathbf{3}} = \mathbf{8} \oplus \mathbf{1}, \tag{2.8}$$

as depicted in Fig. 2.2. Note that this figure shows the pseudoscalar mesons with quantum numbers $L = 0$ and $S = 0$. An equivalent diagram can be drawn for vector mesons with $L = 0$ and $S = 1$. Furthermore, note that the structure in the $SU(3)$ flavour symmetry states shown in Fig. 2.2 is the same as that for the $SU(3)_C$ colour symmetry discussed above. The inclusion of this diagram is purely for pedagogical purposes, as the expansion into multiplets forms a big part of this section.

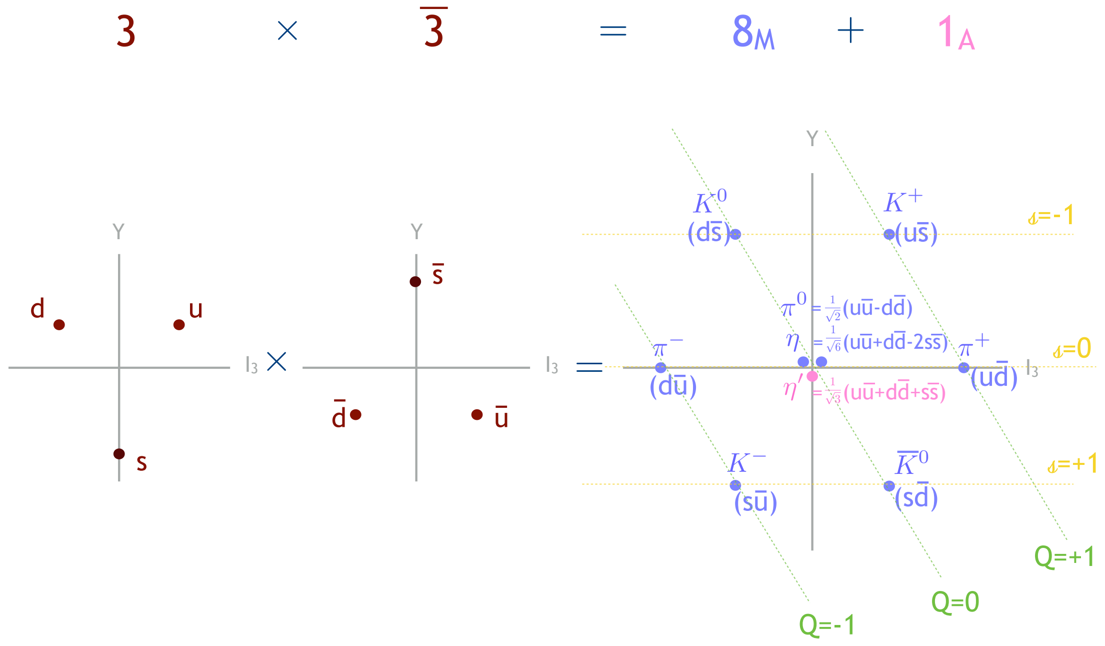

Figure 2.2 *Diagram multiplication of $\mathbf{3} \otimes \bar{\mathbf{3}}$ into a mixed symmetry octet and an anti-symmetric singlet in the plane Y vs. I_3. This diagram shows the ground state pseudoscalar mesons with quantum numbers $L = 0$, $S = 0$ and $J^P = 0^-$.*

Here $\mathbf{3}$ defines the three quark flavours, and $\bar{\mathbf{3}}$ equivalently describes the three anti-quark flavours. The SU(3) symmetry includes three SU(2) subgroups, namely isospin symmetry, U-spin symmetry and V-spin symmetry, each of which can be described using a linear representation of the Gell-Mann matrices. The Gell-Mann matrices describe the fundamental representation of the meson SU(3) symmetry. This symmetry can be expanded to include a fourth quark, c, by extending SU(3) to SU(4). However, the large mass of the c quark implies that this symmetry is badly broken. Even so, the SU(4) classification yields 16 mesons in a 15-plet and a singlet:

$$\mathbf{4} \otimes \bar{\mathbf{4}} = \mathbf{15} \oplus \mathbf{1}, \tag{2.9}$$

Baryons

Extending the meson model to baryons requires adding an extra quark. The light baryons are made up of the three lightest quarks, u, d and s. The three flavours give an approximate $SU(3)$ flavour symmetry. Again, this symmetry is broken since the quarks do not have equal masses. The multiplets of this symmetry can be calculated by expanding $\mathbf{3} \otimes \mathbf{3} \otimes \mathbf{3}$ as shown below. Note that

$$\mathbf{3} \otimes \mathbf{3} = \mathbf{6}_S \oplus \bar{\mathbf{3}}_A \text{ and } \mathbf{3} \otimes \mathbf{6} = \mathbf{10}_S \oplus \mathbf{8}_M \tag{2.10}$$

such that

$$\mathbf{3} \otimes \mathbf{3} \otimes \mathbf{3} = \mathbf{3} \otimes (\mathbf{6} \oplus \bar{\mathbf{3}}) = (\mathbf{3} \otimes \mathbf{6}) \oplus (\mathbf{3} \otimes \bar{\mathbf{3}}) = \mathbf{10}_S \oplus \mathbf{8}_M \oplus \mathbf{8}_M \oplus \mathbf{1}_A. \tag{2.11}$$

Here the subscripts M and A indicate mixed-symmetric or anti-symmetric states under interchange of any two quarks. The S subscript implies a symmetric state. The light ground state baryons belong to the multiplets on the right side of Eq. 2.11.

Adding a c quark to this symmetry expands the $SU(3)$ flavour symmetry in an $SU(4)$ symmetry. The multiplets expected in this flavour symmetry are

$$\mathbf{4} \otimes \mathbf{4} \otimes \mathbf{4} = \mathbf{20}_S \oplus \mathbf{20}'_M \oplus \mathbf{20}'_M \oplus \mathbf{4}_A. \tag{2.12}$$

This symmetry is broken more severely than the $SU(3)$ flavour symmetry, since the c quark has a mass much larger than the three light quarks. Figure 2.3 shows the SU(4) baryon multiplets. All particles in a given SU(4) multiplet have the same spin and parity. Their bottom levels consist of SU(3) multiplets, as expanded in Eq. 2.11. The symmetric $\mathbf{20}_S$ multiplet shown in Fig. 2.3(a) has an $SU(3)$ decuplet as its bottom level, with quantum numbers $J^P = \frac{3}{2}^+$. The states in the mixed symmetry $\mathbf{20}'_M$ multiplet (Fig. 2.3(b)) have $J^P = \frac{1}{2}^+$ and the

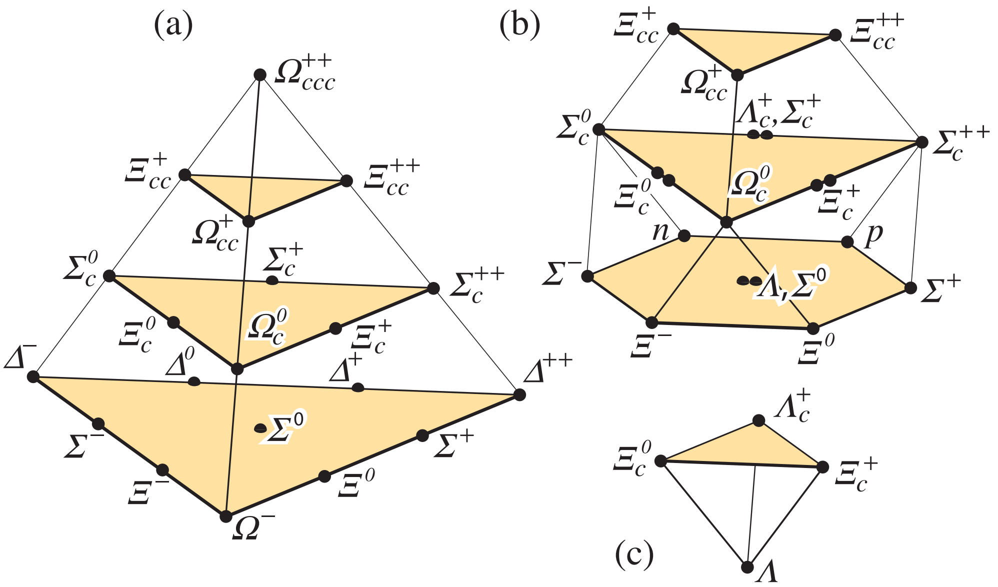

Figure 2.3 *SU(4) multiplets of baryons made of u, d, s, and c quarks. (a) The* $\mathbf{20}_S$*-plet with an SU(3) sextet on the second level from the bottom. (b) The* $\mathbf{20'}_M$*-plet with an SU(3) symmetric sextet and an anti-symmetric SU(3) antitriplet on the second level. (c) The* $\mathbf{4}_A$*-plet with the SU(3) triplet at the top [8].*

bottom level is made up of an $SU(3)$ flavour symmetry octet. Finally, the ground state of the $\mathbf{4}_A$ (Fig. 2.3(c)) is the SU(3) singlet with quantum numbers $J^P = \frac{1}{2}^+$.

The baryon wave function can be described in four parts: colour, space, spin and flavour. The colour part consists of the SU(3) QCD singlet which is anti-symmetric in the three colours. Since quarks are fermions, the baryon wave function is expected to be anti-symmetric under the interchange of two equal mass quarks. According to the (broken) isospin symmetry, the up and down quarks have equal mass. The wave function can be denoted as

$$|qqq\rangle_A = |\text{colour}\rangle_A \times |\text{space, spin, flavour}\rangle_S \tag{2.13}$$

where the subscripts S and A indicate symmetry or anti-symmetry under interchange of any two equal-mass quarks.

For ground state baryons, where $L = 0$, the spatial part of the wavefunction is symmetric. The ground states baryons in the $\mathbf{4}_A$-plet are fully anti-symmetric in flavour. To get a fully anti-symmetric wave function, the spin part is required to be anti-symmetric. This is not possible, such that Fermi statistics, forbid $\mathbf{4}_A$-plet states in the ground state.

2.4 Singly charmed baryons

The singly charmed baryons consist of a c quark and a light $q\bar{q}$ pair. Assuming isospin symmetry, these baryons can be classified according to the light quark pair configurations as shown in Tab. 2.4.

Particle	Quark content	Isospin
Λ_c^+	cud	0 (flavour anti-symmetric)
$\Sigma_c^{0/+/++}$	cqq'	1 (flavour symmetric)
$\Xi_c^{0/+}$	cqs	$\frac{1}{2}$ (either)
Ω_c^0	css	0 (flavour symmetric)

Table 2.4 *Classification of the charmed baryons according to the strong isospin of the light quark pair, where $q, q' \in u, d$.*

Within the flavour SU(3) subgroups, the ground-state heavy baryons containing a single heavy quark belong to

- an antitriplet of flavour anti-symmetric states consisting of $\mathit{\Lambda}_c^+$, $\mathit{\Xi}_c^+$ and $\mathit{\Xi}_c^0$, Fig. 2.4(a).
- a sextet of flavour symmetric states comprising the $\Sigma_c^{++}, \Sigma_c^+, \Sigma_c^0, \Xi_c'^+, \Xi_c'^0$ and Ω_c^0, shown in Fig. 2.4(b).
- a sextet of states composed of the $\Sigma_c^{*++}, \Sigma_c^{*+}, \Sigma_c^{*0}, \Xi_c^{*+}, \Xi_c^{*0}$ and Ω_c^{*0}, displayed in Fig. 2.4(c).

The first two multiplets in this list sit on the middle layer of the mixed-symmetric $\mathbf{20'}_M$ of SU(4) of Fig. 2.3(b). The final sextet has quantum numbers $J^P = \frac{3}{2}^+$ and can be found on the second level of the symmetric $\mathbf{20}_S$ (Fig. 2.3(a))[1].

The $\mathit{\Xi}^0$ baryon has a quark composition of dss. One of the two strange quarks is replaced with a charm to make a $\mathit{\Xi}_c^0$ baryon, such that it has a quark composition of dcs. Note that there are three ground state $\mathit{\Xi}_c^0$ baryons with different quantum numbers: the $\mathit{\Xi}_c^{*0}$ in the SU(3) sextet of the $\mathbf{20}_S$-plet with $J^P = 3/2^+$ and $j_{qq} = 1$, and both the $\mathit{\Xi}_c'^0$ and the $\mathit{\Xi}_c^0$ in the second layer of the mixed symmetric $\mathbf{20'}_M$ with $J^P = 1/2^+$ and $j_{qq} = 1$ and $j_{qq} = 0$ respectively. The quantum number j_{qq} is defined as the angular momentum of the light diquark system, as shown in

---

[1] Fig. 2.3(a) misses the "*" in the names of the single charm baryons. Please see Fig. 2.4 for a more conventional naming scheme.

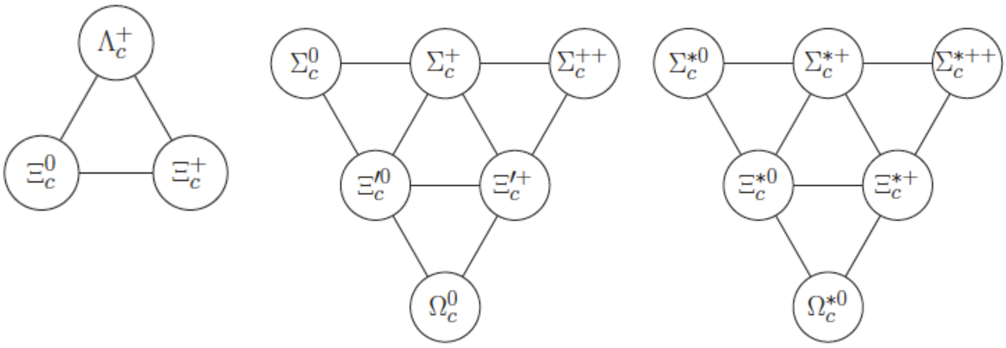

(a) $j_{qq} = 0$ $J^P = \frac{1}{2}^+$ **(b)** $j_{qq} = 1$ $J^P = \frac{1}{2}^+$ **(c)** $j_{qq} = 1$ $J^P = \frac{3}{2}^+$

Figure 2.4 *The SU(3) multiplets containing the ground state charmed baryons, grouped according to the spin j of the light diquark and the spin-parity J^P of the baryon.*

Fig. 2.5. Further quantum numbers of the quark-diquark system will be discussed in the next section. Remember that the ground state of the Ξ_c^0 in the SU(3) triplet of the $\mathbf{4}_A$-plet (Fig. **??**(c)) is forbidden. Because of this ambiguity, a direct comparison between the Ξ^0 and Ξ_c^0 spectra might not be accurate. In addition, since all three quark flavours are different for the Ξ_c^0 baryon, a richer spectrum of excited resonances is expected. These states can be classed in two groups; states for which the light diquark wavefunction is flavour-anti-symmetric (analogous to the Λ_c^+) and states were the light diquark wavefunction is flavour-symmetric (analogous to the Σ_c) for the ground states.

2.4.1 Quantum numbers of singly heavy baryons

Singly heavy baryons are bound states that are made up of two light quarks (u, d and s) combined with a heavy c quark or b quark. A single heavy baryon can be modelled as a diquark-quark system. In this model, the two light quarks make up the diquark and the heavy quark is considered alone, as shown for the case of the singly charmed Ξ_c^0 baryon in Fig. 2.5. Such a model restricts the number of physical states, since a model with three independent quark degrees of freedom would allow for a richer spectrum. The diquark-quark system is characterised by the following quantum numbers: the orbital angular momentum between the two light quarks ($\vec{\ell}_\rho$), the orbital angular momentum between the heavy quark and the diquark system ($\vec{\ell}_\lambda$), the total orbital angular momentum ($\vec{L} = \vec{\ell}_\rho + \vec{\ell}_\lambda$), the sum of the light quarks spins ($\vec{s}_{qq} = \vec{s}_{q_1} + \vec{s}_{q_2}$), the spin of the heavy quark ($\vec{s}_{Q=b,c}$), the angular momentum of the diquark system ($\vec{j}_{qq} = \vec{L} + \vec{s}_{qq}$) and the total angular momentum of the heavy baryon ($\vec{J} = \vec{j}_{qq} + \vec{s}_Q$).

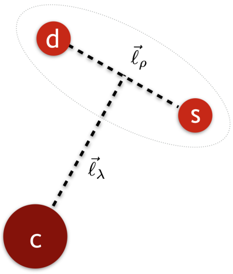

$\vec{\ell}_\rho$	Orbital angular momentum between the two light quarks
$\vec{\ell}_\lambda$	Orbital angular momentum between the heavy quark and the diquark system
$\vec{L} = \vec{\ell}_\rho + \vec{\ell}_\lambda$	Total orbital angular momentum
$\vec{s}_{qq} = \vec{s}_{q_1} + \vec{s}_{q_2}$	Sum of light quarks spins
$\vec{s}_{Q=b,c}$	Spin of the heavy quark
$\vec{j}_{qq} = \vec{L} + \vec{s}_{qq}$	Angular momentum of the diquark system
$\vec{J} = \vec{j}_{qq} + \vec{s}_Q$	Total angular momentum of the heavy meson

Figure 2.5 *Diquark-quark model of single heavy baryon and definition of the relative quantum numbers.*

The quark model coupling scheme can be summarised using the following equation [9]:

$$|J^P, L, s_{qq}\rangle = \left|\left[(\ell_\rho \ell_\lambda)_L \, (s_{qq} s_Q)_S\right]_J\right\rangle \tag{2.14}$$

where the notation $(ab)_c$ means angular momentum c is formed by vector addition from angular momenta a and b and where the parity P is $(-1)^L = (-1)^{\ell_\rho + \ell_\lambda}$. Expanding this equation leads to the quantum number definitions given in Fig. 2.5.

Each diquark system can be described as a boson with quantum numbers ${j_{qq}}^P$, where $j_{qq} = \{0, 1, 2, ...\}$ and $P = \pm 1$. For every diquark system, there is a degenerate heavy baryon doublet, which has several sets of quark model quantum numbers associated to it, leading to the same final state. These may include radially excited states as well. They can be described using

$$|j_{qq}, J\rangle = |L, s_{qq}, S, J\rangle \tag{2.15}$$

where the right hand side quantum numbers are found using the equations in Fig. 2.5. Here, S is the total spin of the three quarks. Note that these hold for either parity configuration. All states in a given multiplet have the same spin and parity. Starting with the singlet states (Fig. 2.3(c)), $|j_{qq} = 0, J^P = \frac{1}{2}^+\rangle$, the expansion gives two ways these can be reconstructed.

$$\begin{aligned} \left|0, \frac{1}{2}\right\rangle &= \left|0, 0, \frac{1}{2}, \frac{1}{2}\right\rangle, \\ \left|0, \frac{1}{2}\right\rangle &= \sqrt{\frac{2}{3}}\left|1, 1, \frac{3}{2}, \frac{1}{2}\right\rangle - \sqrt{\frac{1}{3}}\left|1, 1, \frac{1}{2}, \frac{1}{2}\right\rangle \end{aligned} \qquad (2.16)$$

The top state corresponds to the $L = 0$ option, and the bottom equation gives the $L = 1$ vector states. The coefficients under the square root are Clebsch-Gordan coefficients [6].

The $SU(3)$ flavour multiplets are expanded into states with $J = (\frac{1}{2}, \frac{3}{2})$. They are given by

$$\begin{aligned} &\left|1, \frac{1}{2}\right\rangle = \left|0, 1, \frac{1}{2}, \frac{1}{2}\right\rangle, \quad \left|1, \frac{3}{2}\right\rangle = \left|0, 1, \frac{3}{2}, \frac{3}{2}\right\rangle, \\ &\left|1, \frac{1}{2}\right\rangle = \left|1, 0, \frac{1}{2}, \frac{1}{2}\right\rangle, \quad \left|1, \frac{3}{2}\right\rangle = \left|1, 0, \frac{1}{2}, \frac{3}{2}\right\rangle, \\ &\left|1, \frac{1}{2}\right\rangle = \sqrt{\frac{2}{3}}\left|1, 1, \frac{1}{2}, \frac{1}{2}\right\rangle + \sqrt{\frac{1}{3}}\left|1, 1, \frac{3}{2}, \frac{1}{2}\right\rangle, \quad \left|1, \frac{3}{2}\right\rangle = -\sqrt{\frac{1}{6}}\left|1, 1, \frac{1}{2}, \frac{3}{2}\right\rangle + \sqrt{\frac{5}{6}}\left|1, 1, \frac{3}{2}, \frac{3}{2}\right\rangle, \\ &\left|1, \frac{1}{2}\right\rangle = \left|2, 1, \frac{3}{2}, \frac{1}{2}\right\rangle, \quad \left|1, \frac{3}{2}\right\rangle = \sqrt{\frac{1}{2}}\left(-\left|2, 1, \frac{1}{2}, \frac{3}{2}\right\rangle + \left|2, 1, \frac{3}{2}, \frac{3}{2}\right\rangle\right), \end{aligned} \qquad (2.17)$$

Further expansions to states with different quantum numbers can be made in a similar fashion.

2.4.2 Heavy quark effective theory

Theoretical predictions of excited charmed baryons spectra are very complicated. Since lattice-based methods are time consuming and require a lot of CPU, many of the calculations employ models, built on simplifications of the theory. Heavy quark effective theory (HQET) is used to estimate the spectrum of excited baryons containing one heavy quark. In HQET, the large difference between the masses of the heavy quark and the lighter quarks is exploited. It holds for heavy quarks Q where $\Lambda_{QCD} << m_Q$, where Λ_{QCD} is the QCD coupling constant and m_Q is the mass of the heavy quark. The excited heavy baryon masses are calculated in the limit where $m_Q \to \infty$. Afterwards, higher order term corrections in powers of $1/m_Q$ are applied. In this limit, the spin and parity quantum numbers of the light degrees of freedom in the hadron are conserved. In addition, the spin and parity of the heavy quark is also conserved. Thus, strong decays of excited heavy baryons depend only on the light diquark system. The light degrees of freedom are used to derive the selection rules for these decays. However, to extrapolate the rules for the physical baryon states, the heavy quark needs to be considered as well.

When the light diquark system has spin $j_{qq} > 0$, the spin of the total system is given by $J = j_{qq} \pm 1/2$. This allows for two possible options, generating a doublet of heavy hadrons with total spins (J_1, J_2). The two states in each doublet are nearly degenerate, their masses split only by a chromomagnetic interaction, which is suppressed by the large mass of the heavy quark.

In the framework of HQET, the states are assumed to have the coupling scheme:

$$|J^P, j_{qq}\rangle = \left| \left\{ \left[(\ell_\rho \ell_\lambda)_L \, s_{qq} \right]_j s_Q \right\}_J \right\rangle . \tag{2.18}$$

In this scheme the ground states of the single charmed baryons are characterised by the quantum numbers $|j_{qq} = 0, J^P = \frac{1}{2}^+\rangle$, $|j_{qq} = 1, J^P = \frac{1}{2}^+\rangle$ and $|j_{qq} = 1, J^P = \frac{3}{2}^+\rangle$ (Fig. 2.4).

In summary, in the framework of HQET, J^P and j_{qq} are good quantum numbers and they must be preserved during the strong decays of one state into another. The question arises is to what extent the experimentally observed excited heavy baryon states match the theoretical predictions formed using HQET. We hope to shed some light on this question with the search for excited Ξ_c^0 baryons in the $\Lambda_c^+ K^-$ spectrum described in Chapter 6.

2.4.3 The orbitally excited $L = 1$ states

The P-wave ($L = 1$) excited states can be obtained by an excitation of the angular momentum between the light quarks ($\ell_\rho = 1$ and $\ell_\lambda = 0$) or between the charm quark and the two light quark system ($\ell_\rho = 0$ and $\ell_\lambda = 1$). Using the equations given in Fig. 2.5, we calculate 14 expected orbitally excited ($L = 1$)

Ξ_c^0 states (Fig. 2.6): six with $J^P = 1/2^-$, six with $J^P = 3/2^-$ and two with $J^P = 5/2^-$. The notation in Fig. 2.6 is as follows: $\bar{3}_C(A)$ denotes the anti-symmetric $SU(3)_C$ colour symmetry. The subscript F denotes the states belong to a flavour multiplet. The notations $6_F(A)$ and $\bar{3}_F(A)$ correspond to the symmetric flavour sixtet and anti-symmetric flavour triplet given by the flavour symmetry between the two light states, as shown in Fig. 2.11. The final classification on the right of the figure gives a summary of the obtained states, in terms of [multiplet $\in 6_F(A), \bar{3}_F(A), j_{qq}, s_{qq}, \rho$ if $l_\rho = 1$ and λ if $l_\lambda = 1$].

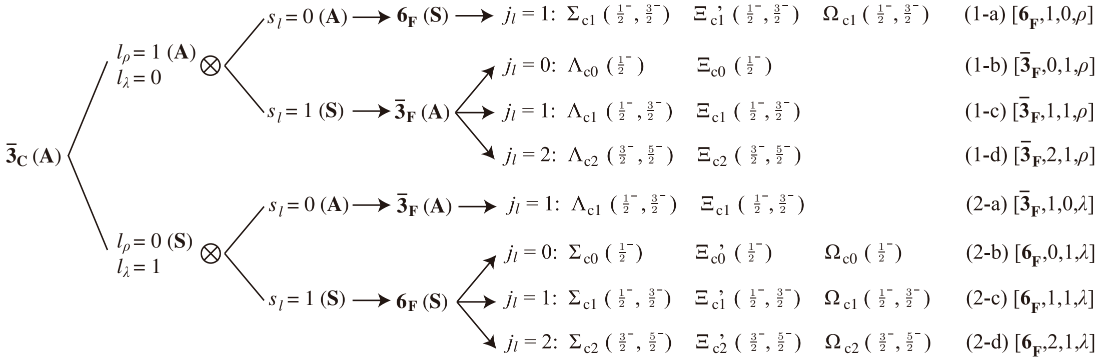

Figure 2.6 *The notations for P-wave charmed baryons.* $\mathbf{6}_F$ *(*$\mathbf{S}$*) and* $\bar{\mathbf{3}}_F$ *(*$\mathbf{A}$*) denote the* $SU(3)$ *flavour representations.* $\bar{\mathbf{3}}_C$ *(*$\mathbf{A}$*) denotes the* $SU(3)$ *colour representation.* $s_l = s_{qq}$ *is the spin angular momentum of the two light quarks, and* $j_l = j_{qq} = l_\lambda \otimes l_\rho \otimes s_l$ *is the total angular momentum of the two light quarks [10].*

Predictions for the masses of the $\Xi_c^{(*)0}$ states and higher excitations spread over a wide range of values, as shown in Fig. 2.7 [11]. The mass predictions are shown with respect to the D_s mass and are based on lattice calculations. The size of the boxes correspond to the uncertainties in the computation. The states on the left side of the figure in the dotted box consist of excited D-wave and radially excited states. The excited P-wave states are in the dotted box on the right, and are comparable to the 14 P-wave excited ($L = 1$) states calculated in Fig. 2.6 [10].

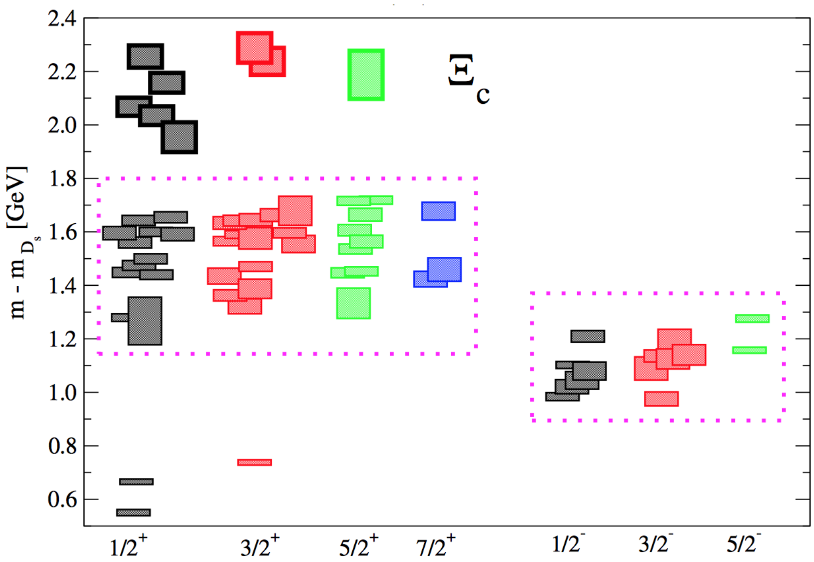

Figure 2.7 *Mass predictions of the excited Ξ_c states with respect to the D_s mass based on lattice calculations. The states in the dotted box on the left side consist of excited D-wave and radially excited states. The excited P-wave states are in the dotted box on the right. The size of the boxes correspond to the uncertainties in the computation. Figure taken from [10].*

Chapter 3

The LHCb Detector

3.1 The Large Hadron Collider

The Large Hadron Collider (LHC) [12] is a particle accelerator, built within a tunnel of 27 km circumference, roughly 100 m underground. The LHC project was approved by the CERN council in December 1994. The tunnel had previously been built for the Large Electron-Positron (LEP) collider [13]. The LHC is located at the European Organisation for Nuclear Research (CERN) on the French-Swiss border. The collider was built with the aim of discovering the Higgs particle and to measure rare events that only occur at very high energies. The LHC is capable of accelerating protons to a centre-of-mass energy of $\sqrt{s} = 14$ TeV, making it the most powerful particle accelerator at the time the data analysed in this thesis was taken.

Figure 3.1 shows the chain of accelerators at CERN. The protons pass through several accelerators, gaining energy at each stage, before they are energetic enough to be injected into the LHC. The protons used in the LHC are obtained by passing hydrogen gas through an electric field, such that the electrons are stripped off through ionisation. The protons are accelerated from the source in the LINear ACcelerator 2 (LINAC2), a linear accelerator making use of radiofrequency cavities to charge cylindrical conductors. Neighbouring conductors are oppositely charged, therefore pushing and pulling the protons to increase their velocity. When they reach the end of LINAC2, the protons have reached an energy of 50 MeV, and are injected in the Proton Synchotron Booster (PSB). The injection

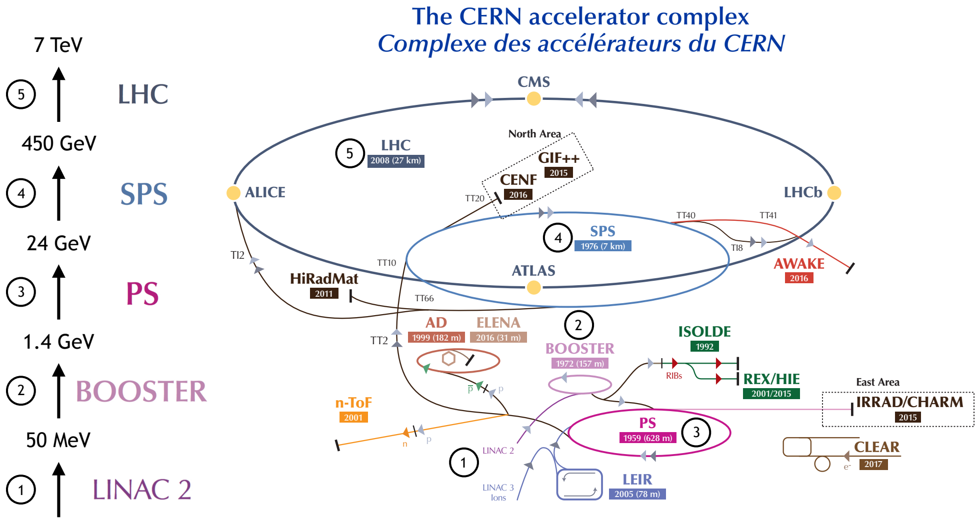

Figure 3.1 *Illustration of the CERN complex, displaying the accelerators used at the LHC along with the energies the particles reach as they pass through them. Figure adapted from [14].*

occurs every 100 ms, providing groups of up to 1×10^{11} protons, called bunches, used in the LHC collisions. The PSB consists of four superimposed synchotron rings and accelerates the bunches up to an energy of 1.4 GeV. The next stage is the Proton Synchotron (PS). The TORCH prototype, discussed in Chapters 7 and 8, is validated in a beam of particles stemming from PS, since it provides particles of the required momentum to test the TORCH time-of-flight principle. The PS has a circumference of 628 m, where 277 electromagnets bend the beams around the ring to accelerate the protons to 24 GeV. After PS, the particles are injected into the Super Proton Synchotron (SPS), where energies up to 450 GeV are reached. With a 7 km circumference, SPS is the second largest accelerator in the LHC and directly provides a beam to several experiments, including NA61/SHINE [15], NA62 [16], the COMPASS experiment [17] and soon the AWAKE experiment [18]. The SPS provides the beam for the LHC, where before injection the particles are separated into two beams travelling in opposite directions.

Along the LHC ring, the beams are allowed to collide at four interaction points. Four physics detectors are placed at the beam crossing points to detect the resulting physics processes. Two of them are general purpose detectors, measuring all detectable processes over the full solid angle experiments: the Compact Muon Solenoid (CMS) [19] and A Toroidal LHC ApparatuS (ATLAS) [20]. A Lead Ion Collision Experiment (ALICE) [21] is the third physics detector, measuring collisions of lead nuclei which circulate inside the LHC during special operational periods. The final detector built at a proton-proton collision point is LHC beauty (LHCb), which is described in detail in this section. The LHC accelerator houses three more experiments, not situated at interaction points: the TOTEM experiment [22], the LHCf experiment [23] and the Monopole and Exotics Detector at the LHC (MoEDAL) [24].

3.2 The LHCb Detector

The LHCb detector [25] is a single-arm forward spectrometer designed to observe interactions involving the heavy charm (c) and beauty (b) quarks.

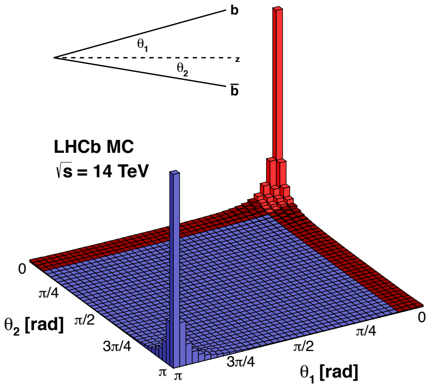

Figure 3.2 *The angular distribution of the production of $b\bar{b}$ quark-antiquark pairs at $\sqrt{s} = 14$ TeV. The LHCb detector acceptance is indicated by the red shaded area [25].*

Figure 3.2 shows the angular distribution of $b\bar{b}$ quark-antiquark production at $\sqrt{s} = 14$ TeV, where the LHCb detector acceptance is indicated in red. The LHCb geometry exploits the fact that $b\bar{b}$ pairs are predominantly produced at angles close to the beam pipe. The primary production mechanism of $b\bar{b}$ pairs at LHCb is gluon fusion. Considering one of the high energy LHC protons in its lab frame, its gluons have highly asymmetric momenta. Gluon fusion occurs when two such high-momentum gluons collide in the pp interaction. The newly formed

$b\bar{b}$ pair is boosted in the direction of the high momentum gluon, which is along the beam pipe. This motivates LHCb's pseudorapidity range of $1.9 < \eta < 4.9$. At LHCb, the $b\bar{b}$ production cross section is roughly 500 μb at an energy of 14 TeV, leading to an expected production of 10^{12} $b\bar{b}$ pairs in one year of data taking at a luminosity of $\mathcal{L} = 2 \times 10^{32}\text{cm}^{-2}\text{s}^{-1}$. Run I of data taking at the LHC includes data taken between 2010-2012, which at LHCb corresponds to a total recorded integrated luminosity of 3 fb^{-1} of data recorded at an energy of 7 TeV (2010,2011) and 8 TeV (2012). Run II data has been recorded between 2015-2018 at a centre-of-mass energy of 13 TeV. A total of 6.1 fb^{-1} of data was recorded during Run II of data taking at LHCb. Figure 3.3 shows the recorded integrated luminosity at the LHCb experiment in pp collisions, per data taking year. The total amount of data recorded currently is 9.1 fb^{-1}.

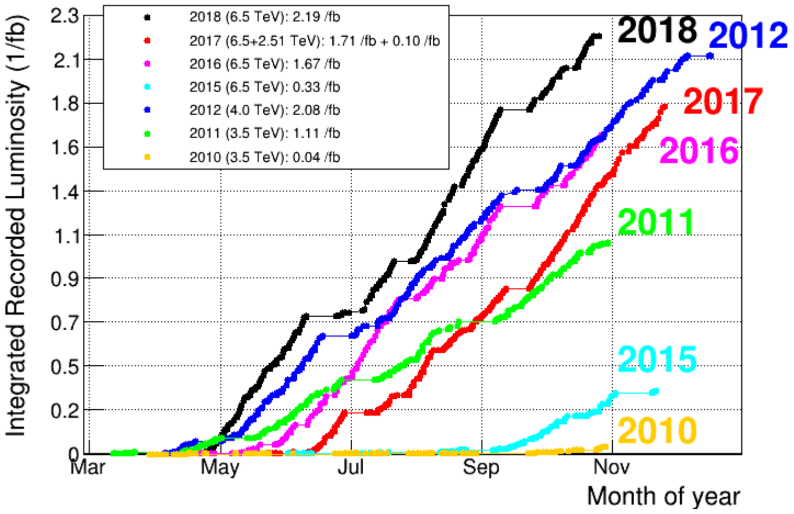

Figure 3.3 *The integrated luminosity recorded at the LHCb experiment in pp collisions, given by year [25].*

A cross-section of the LHCb detector is given in Fig. 3.4, along with the coordinate system used in this chapter to describe it. The z-axis is defined along the length of the detector, such that it increases as the beams pass through the detector. The y-axis is perpendicular to the z-axis in the vertical plane, where the positive direction is upwards. Finally, the x-axis lies in the horizontal, where the positive direction points to the centre of the LHC ring. The pp collision takes place inside the VErtex LOcator (VELO) at coordinates $(x, y, z) = (0, 0, 0)$, where accurate tracking of the initial particle interactions is performed. The particles travel downstream through the first of two Ring Imaging CHerenkov (RICH) detectors, used for particle identification (PID). Next, they traverse the Tracker Turicensis (TT), after which the particles pass through a powerful magnet in which charged particle paths are bent. Three more tracking stations (T1-T3) are placed after the magnet, in addition to the second RICH detector. Finally, the particles pass through the calorimeter system, consisting of the hadronic calorimeter (HCAL) and the electromagnetic calorimeter (ECAL), followed by the muon chambers (M1-M5). The sub-detectors serve two main functions, tracking the particles and identifying the particles. A more detailed description of each of these sub-systems follows in this chapter, starting with the sub-detectors necessary for tracking, after which the particle identification systems are described.

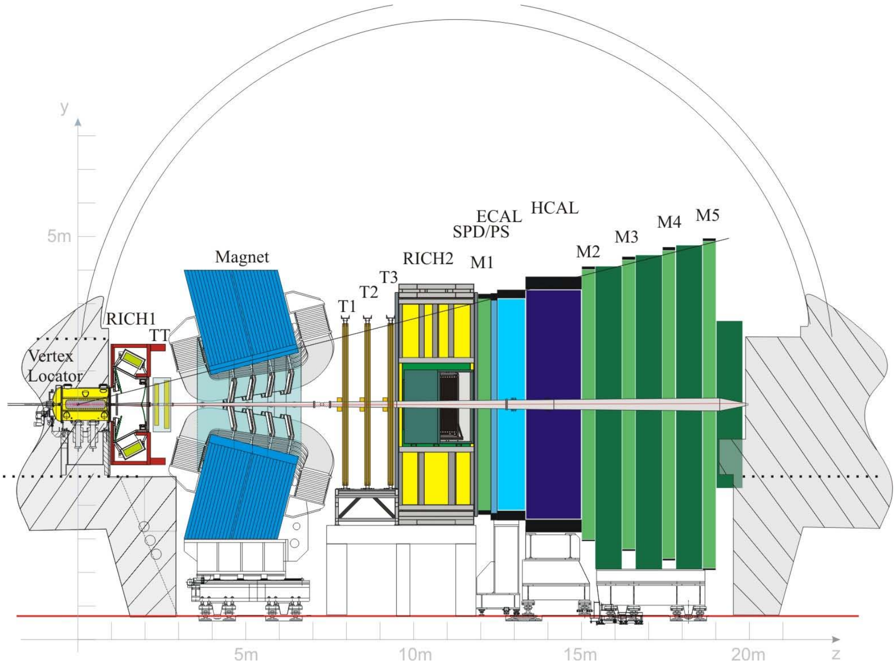

Figure 3.4 *Illustration of the LHCb detector, where the coordinate system is displayed and the sub-detector systems are labelled [25].*

3.3 The Tracking System

The aim of LHCb's tracking system is to track the particles passing through the detector. It consists of the VELO, to determine the decay vertex of heavy mesons; the two Silicon sensor Trackers, Tracking Turicensis (TT) and the Inner Tracker (IT), and finally the Outer Tracker (OT) which is based on a drift-time principle.

3.3.1 Vertex Locator

The VELO [26] is a tracking detector, made up of silicon sensors, placed around the *pp* interaction point inside the LHCb detector. Figure 3.5 gives a schematic overview of the VELO. The 21 silicon modules are placed close together around the *pp* interaction region to obtain a high Primary Vertex (PV) reconstruction, where the PV is defined as the *pp* interaction point. The VELO aims to distinguish between PVs and Secondary Vertices (SV), which is where the long lived hadrons typically produced in the LHCb detector decay. At LHCb, a PV resolution of roughly 150 μm is achieved if there are 10 tracks in the PV [27].

Due to the proximity of the VELO to the LHC beam line, the sub-detector was built with radiation hardness in mind. Additionally, the VELO consists of two structures which are capable of separating. During beam injection into the LHC the VELO is fully opened, such that the closest part of the detector is 29 mm removed from the beam line. After stable beams have been achieved, the two parts are carefully brought together, such that a small region of overlap is attained. When the VELO is fully closed, the closest silicon sensors are merely 8.2 mm away from the beam line.

The silicon micro-strips contain two types of sensors, the R-type sensor which measures the radius from the beam line and the ϕ-sensor, which determines the azimuthal angle. This is shown in Fig. 3.6. The z-coordinate can be extracted by determining the module that registered the hit. Figure 3.5 shows the R sensors in red and the ϕ sensors in blue.

3.3.2 Magnet

A large dipole magnet with a field strength of approximately 4 T·m allows for momentum determination of charged particles passing through. The magnet consists of a 150 ton iron yoke and two saddle shaped coils weighing 54 tons, placed above and below the beam line. The magnet is placed between the TT and the T1-T3 tracking stations, such that the curvature of the particles can be reconstructed using information from the tracking systems. Using this information the momentum of the particle can be determined for particles up to a momentum of 200 GeV/c with an accuracy of 1.0%.

During data taking, data is collected in two separate configurations: magnet up,

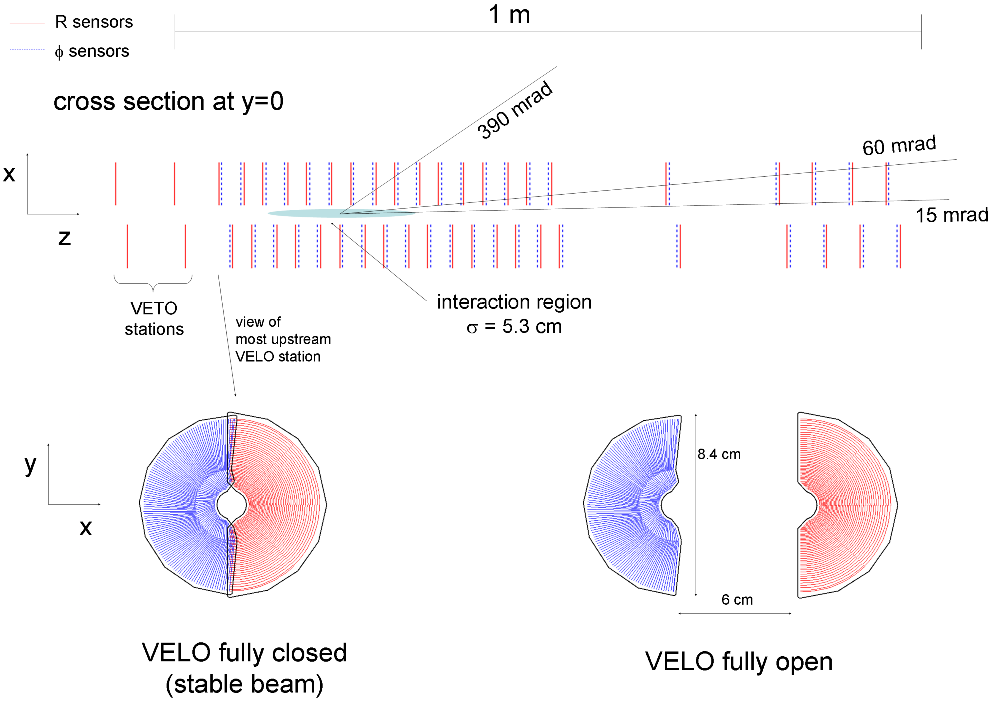

Figure 3.5 *Schematic view of the VELO modules, where the R sensors are given in red and the ϕ sensors in blue [26].*

where the field points in the positive y-direction, and magnet down, where the field points in the $-y$ direction. This mitigates potential detector asymmetry effects for example due to detector inefficiency.

3.3.3 Tracker Turicensis and Inner Tracker

The Tracker Turicensis (TT) and Inner Tracker (IT) are often discussed simultanously in LHCb documents, since they are both part of the joint Silicon Tracker (ST) project. The TT and the IT, which comprises the inner parts of the T1-T3 trackers, are made of radiation-hard silicon strips.

The TT, shown in Fig. 3.7 is a tracker of dimensions 1.5 m × 1.3 m, covering the full LHCb acceptance upstream of the magnet. The tracker consists of four layers, where the middle two layers are rotated at $+5^\circ$ and -5° to maximise the spatial resolution in the x-direction. The TT consists of 500 μm thick, single sided p^+-on-n silicon sensors with a pixel pitch of 200 μm. Each TT sensor has 512 readout strips, and a resolution of 50 μm is achieved. Each TT half module consists of 7 silicon sensors, as shown in Fig. 3.7. To account for a higher occupancy near

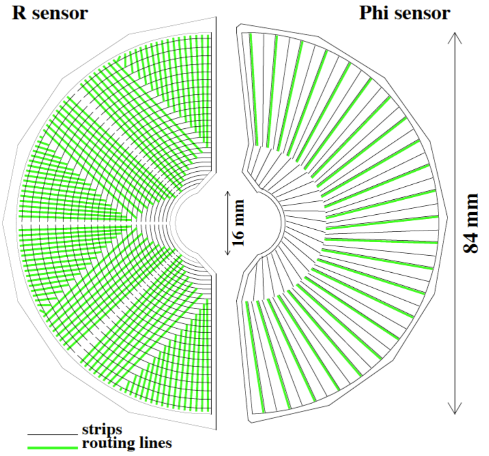

Figure 3.6 *Schematic view of the R and ϕ sensors in the VELO sub-detector. The routing lines are orientated perpendicular (R-type) and parallel (ϕ-type) to the silicon strips [26].*

the beam line, the different tones of brown in the figure indicate a difference in readout systems.

The IT, shown in Fig. 3.8, has a cross-shaped configuration and is of dimensions 1.2 m × 0.4 m. It comprises the inner region of the tracking stations T1-T3, close to the beam pipe, downstream of the magnet. The cross shape accounts for a higher occupancy in the vertical direction due to bending of charged particles in the magnet. The IT consists of p^+-on-n silicon sensors with 384 readout strips. The tracker has one sensor of thickness 320 μm or two sensors 410 μm thick, depending on their position. The pitch of the sensors is 193 μm and a spatial resolution of 50 μm is achieved.

3.3.4 Outer tracker

The Outer Tracker (OT) [28] consists of the outer regions of the tracking stations T1-T3. Each tracker is comprised of four layers, which are set up in the same configuration as the TT such that the middle two layers are rotates by $+5°$ and $-5°$. This is shown in Fig. 3.9. The tracker sensors contains gaseous straw tubes, allowing for a drift time measurement to determine charged particle trajectories. The outer boundaries of the OT correspond to a 300 mrad acceptance horizontally, and a 250 mrad acceptance vertically.

Gaseous straw tubes provide a cost effective method to measure the particle paths in the regions farther away from the beam line where occupancy is lower.

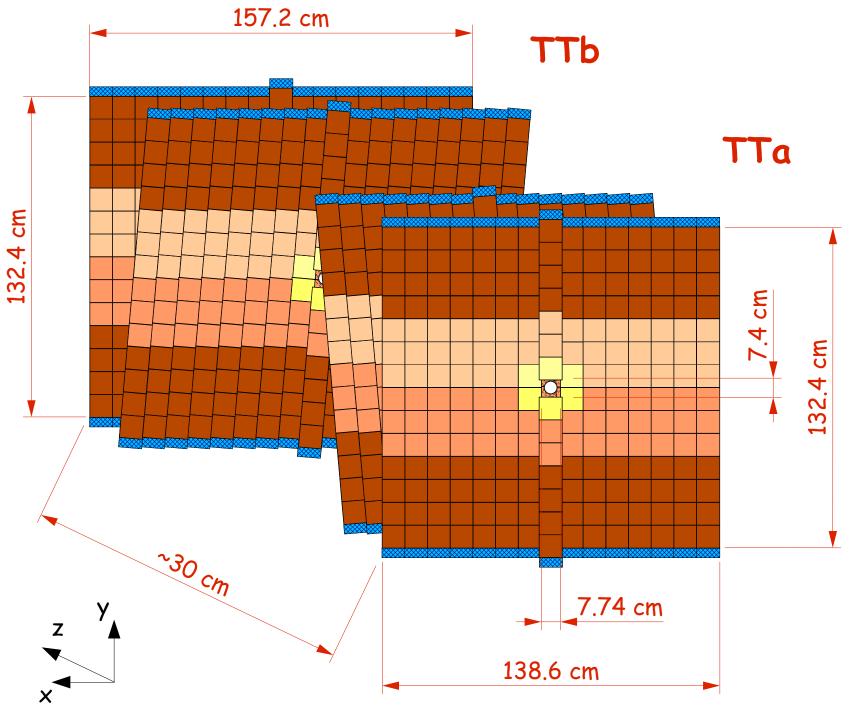

Figure 3.7 *Layout and dimensions of the four layers in the Tracker Turicensis, where the sensor placement is indicated by the different shades of brown [25].*

Figure 3.10 gives a cross section of an outer tracker module. Each module consists of two layers of drift tubes with a diameter of 4.9 mm. The drift tubes contain a cathode on the outer edge, an anode wire in the middle and the volume is filled with a gas mixture of 70 % argon and 30 % CO_2. As charged particle pass through the drift chambers, the gas ionises, such that the electrons are accelerated to the anode where the signal can be measured. The OT has a drift time resolution of 2.6 ns and a spatial drift resolution of 179 μm. Combining the drift time and drift velocity, the position of charged particle tracks is reconstructed.

3.4 Particle Identification

When a particle passes through the LHCb detector, it is crucial that it can be identified. Two Ring Imaging CHerenkov (RICH) detectors enable identification of charged particles with momenta between 2 to 100 GeV/c. Furthermore, two calorimeter systems, the Electromagnetic CALorimeter (ECAL) and Hadronic CALorimeter (HCAL) determine the energy deposited by electrons or photons,

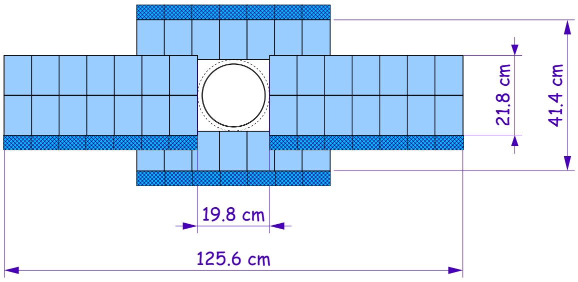

Figure 3.8 *Layout and dimensions of the T1-T3 trackers displaying the placement of the straw tube modules [25].*

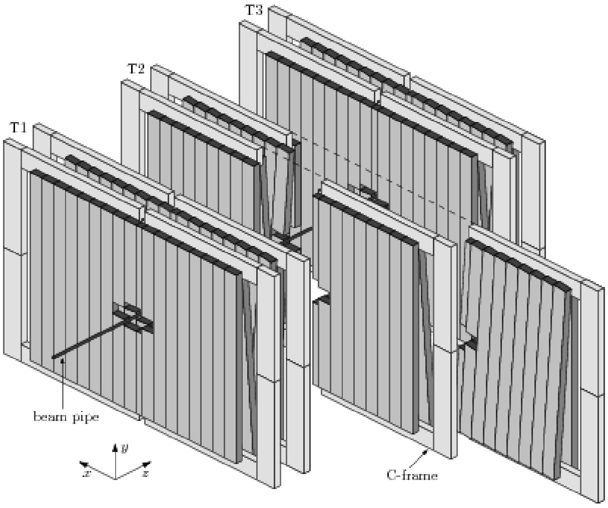

Figure 3.9 *Layout of the Outer Tracker system [25].*

and hadrons, respectively. Finally, a set of five muon chambers identify muons passing through.

3.4.1 The RICH detectors

The Ring Imaging CHerenkov (RICH) detectors at LHCb are based on the principle of Cherenkov radiation. Note that the TORCH detector described in Chapter 7 also employs Cherenkov light. Cherenkov radiation occurs when a charged particle travels through a medium faster than the speed of light in that medium. Cherenkov photons are emitted in a cone shape with opening angle θ_c with respect to the direction of the particles momentum as

$$\cos\theta_c = \frac{1}{n\beta}, \tag{3.1}$$

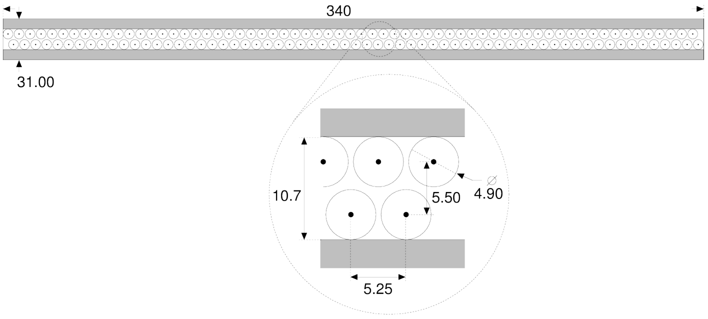

Figure 3.10 *Schematic depiction of an outer tracker module, where the two-layer arrangement of gas-filled drift tubes is shown [25].*

where n is the refractive index of the medium and $\beta = v/c$, where v is the velocity of the particle and c is the speed of light in a vacuum. The angle θ_c, in mrad, of Cherenkov photons produced from different particle species over a momentum range of 1-100 GeV/c for aerogel and the gases in RICH1 (C_4F_{10}) and RICH2 (CF_4) is shown in Fig. 3.11. The plot clearly displays that θ_c reaches a plateau once the momentum is large enough. The gas in the RICH1 detector provides good particle identification for lower momenta particles, whereas the CF_4 gas used in the RICH2 detector gives a good separation between kaons and pions of higher momenta. The aerogel shows great PID possibilities at low momenta. The aerogel block was removed from the detector before Run II of data taking commenced, since it did not improve the PID performance. The TORCH detector 7 aims to improve LHCb's PID performance at low momenta.

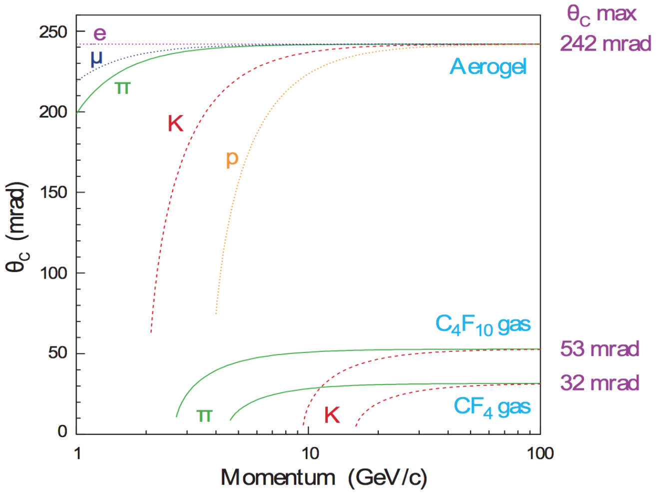

Figure 3.11 *The Cherenkov angle, θ_c, in mrad, of Cherenkov photons produced from different particle species over a momentum range of 1-100 GeV/c for aerogel and the gases in RICH1 (C_4F_{10}) and RICH2 (CF_4) [29].*

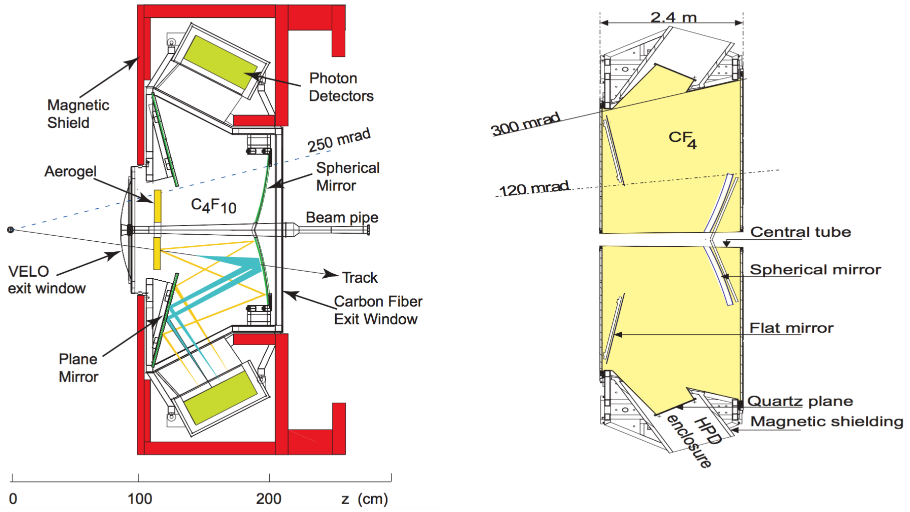

Figure 3.12 *Schematic overview of the RICH1 (left) and RICH2 (right) detectors [25].*

The RICH1 detector is positioned between the VELO and the TT. It covers the full angular momentum and provides PID for particles between 1-60 GeV/c. The photodetector planes are split into two halves, one above the beam line and one below the beam line. The RICH2 covers the full LHCb angular acceptance. The RICH 2 sub-detector is placed between the third tracking station, T3, and the first muon station, M1. It successfully distinguishes particles with momenta between 15 and 100 GeV/c. Since high momentum particles are less bent by the magnet, the RICH2 detector covers a smaller angular acceptance of 15 mrad up to 100 (120) mrad in the vertical (horizontal) plane. The RICH2 detector plane is also made up of two sections, placed at either horizontal side of the beam line. The layout of the RICH detectors is given in Fig. 3.12. The Cherenkov radiation is emitted and reflected out of the detector acceptance by a spherical mirror and a flat mirror. They are focused on detection planes, where the Cherenkov photons are detected using Hybrid Photon Detectors (HPDs). Each half of RICH1 (RICH2) is equipped with 98 (144) HPDs. The particles velocity is reconstructed by identifying rings of Cherenkov photons. In combination with the momentum information from the tracking stations, the mass is determined, and the particle can be identified.

3.4.2 Calorimeter systems

Calorimetry at LHCb is performed through four sub-systems; the Pre-Shower (PS), the Scintillator Pad Detector (SPD), the Electromagnetic CALorimeter (ECAL) and the Hadronic CALorimeter (HCAL). The detectors uses scintillating media, exploiting the fact that the amount of released photons is dependent on the energy loss of the particle over a given path length.

The ECAL is used to trigger on electrons and photons, as they interact primarily through the electromagnetic force. The ECAL is crucial within LHCb for neutral particle reconstruction. It comprises a 2 mm lead layer, stopping the particle to produce an electromagnetic shower, in a 4 mm thick scintillation material. The layout of the ECAL is shown on the left in Fig. 3.13. Light is generated in the scintillation pads, which are read out by wavelength-shifting (WLS) fibres. The photons from the fibres are read out by photo-multiplier tubes (PMTs). The total depth of the ECAL is 42 cm, corresponding to 25 radiation lengths. The cell structure is shown in Fig. 3.14(left), where the cell size increases in two stages as the distance from the beam line increases. This ensures a low particle occupancy across the calorimeter.

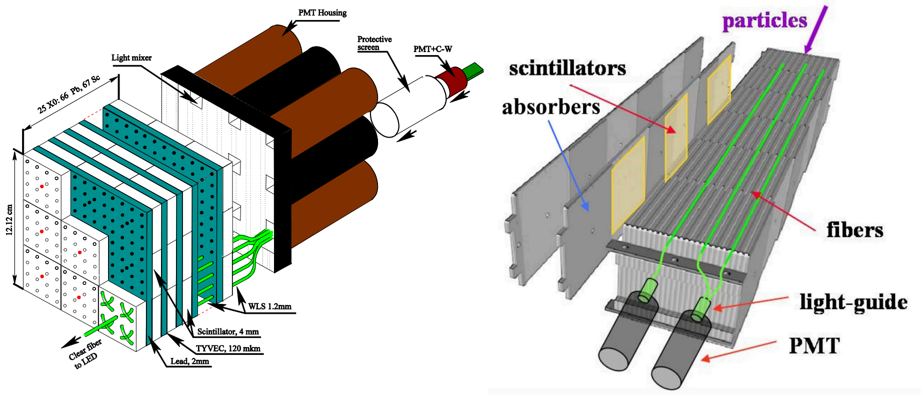

Figure 3.13 *Schematic layout of the ECAL module (left) and the HCAL module (right) [25].*

In front of the ECAL is the Pre-Shower (PS) and the Scintillating Pad Detector

(SPD). The PS detects electromagnetic showers to distinguish between electrons and photons. The SPD discriminated between hadrons and neutrally charged particles. Both the PS and SPD consist of a 15 mm lead converter sandwiched between two scintillators. The size of the detector is 6.2 m in height by 7.6 m in width. The ECAL cells correspond on a one-to-one basis with those in the PS and SPD. Similarly to the ECAL, the light from the scintillating layers in the PS and SPD are collected using WLS fibres and read out using multi-anode PMTs.

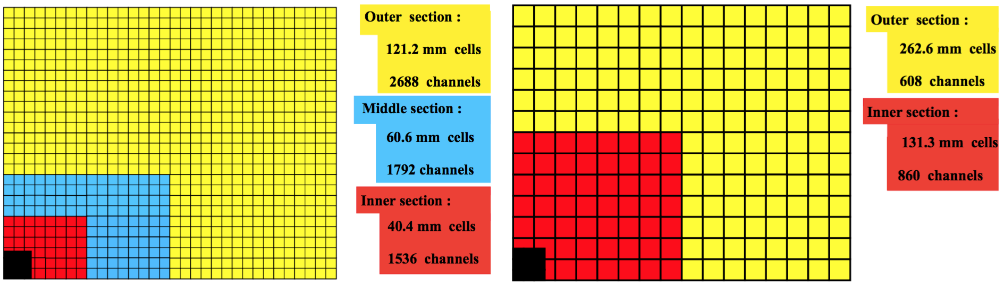

Figure 3.14 *Segmentation design of the SPD, PS and ECAL (left) / HCAL (right). The black square indicates the beam pipe [25].*

In the HCAL, the position and energy of hadrons, interacting through the strong force are measured. It is divided into cells of two different sizes, rather than the three configurations used in the ECAL, as shown in Fig. 3.14(right). The HCAL modules are located parallel to the z-axis, whereas the ECAL modules are perpendicular to the z-axis. The HCAL contains plates of 1 cm thick iron plate absorbers, with 3 mm of scintillators. The thickness of the HCAL corresponds to 5.6 hadronic interaction lengths. As in the other calorimeter systems, the photons are collected by optical fibres and read out using PMTs. The layout of the HCAL is shown on the right in Figure 3.13, where the absorbers, scintillators, PMTs and WLS fibres are shown, along with the PMT used to read out the signal.

3.4.3 Muon Chambers

In the muon chambers, the position muons passing through the detector are measured. Since muons are heavier than electrons and lose less energy due to Bremsstrahlung compared to electrons, they tend to pass through the full LHCb detector. This explains the fact that the muon stations are placed at the end of the detector. Five rectangular stations make up the muon chambers, where the first one, M1, is placed before the calorimetry system, and M2-M5 are situated behind the calorimeters (Fig. 3.15). The first muon chamber is placed closer to the pp interaction point to provide a better muon momentum measurement. Between each of the downstream muon chambers, an 80 cm thick iron absorber is placed. This ensures no hadrons pass through the muon chambers, and provides a method to classify muons into momentum bins depending on how far in the detector they reach. Muons of momenta 3 GeV/$c < p <$ 6 GeV/c are expected to provide hits in M2 and M3. If the momentum is between 6 and 10 GeV/c, hits are expected in M2, M3 and either M4 or M5. Muons with a momentum larger than 10 GeV/c should provide hits in all muon stations. The muon chambers increase in size as they are placed further downstream such that the angular acceptance for all systems is the same as 20 (16) by 306 (258) mrad in the horizontal (vertical) direction. Similar to the calorimetry system, the system is divided in regions depending on the distance from the beam line. These are labelled R1-R4, as shown in Fig. 3.15. The granularity increases as the regions are further removed from the beam line, such that the occupancy along the detector is comparable.

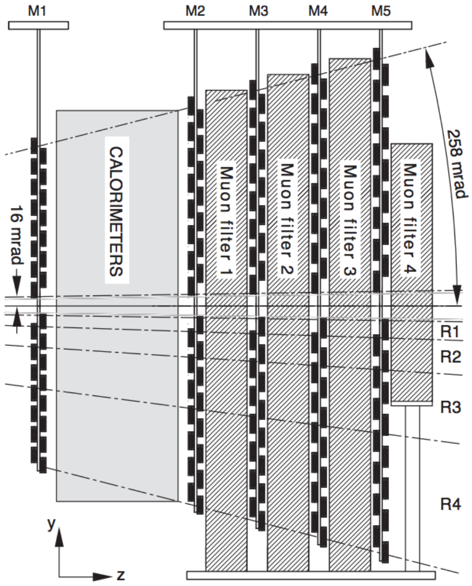

Figure 3.15 *Schematic overview of the five muon chambers [25].*

The detection mechanism in the muon chambers is based on Multi-Wire Proportional Chambers (MWPCs). The MWPCs are filled with a gas mixture, comprised of CO_2 (55%), Ar (40%) and CF_4 (5%). As the muon passes through the detector, the gas is ionised. The ionisation electrons are collected on a gold-plated tungsten wire of diameter 30 μm. A drift-time resolution of 5 ns is achieved.

In the region closest to the beam line in M1, 12 Gas Electron Multiplier (GEM) chambers are used rather than the MWPCs. The GEM chambers are more resistant to radiation which is necessary in the high occupancy region of the muon chambers. The GEM chambers consist of a cathode, and electrode and three GEM foils. It is filled with the same gases as the MWPCs, but with different proportions: CO_2 (15%), Ar (45%) and CF_4 (40%). A drift time resolution of 3 ns is achieved in the GEMs.

3.5 The LHCb trigger system

The relevant physics processes stemming from the pp collision at the LHCb detector need to be disentangled from the large amount of data produced. The LHCb trigger [30] provides the first steps to reducing the size of the data stored. The trigger system consists of three stages, an initial hardware trigger followed by two high-level software triggers, as shown in Fig. 3.16.

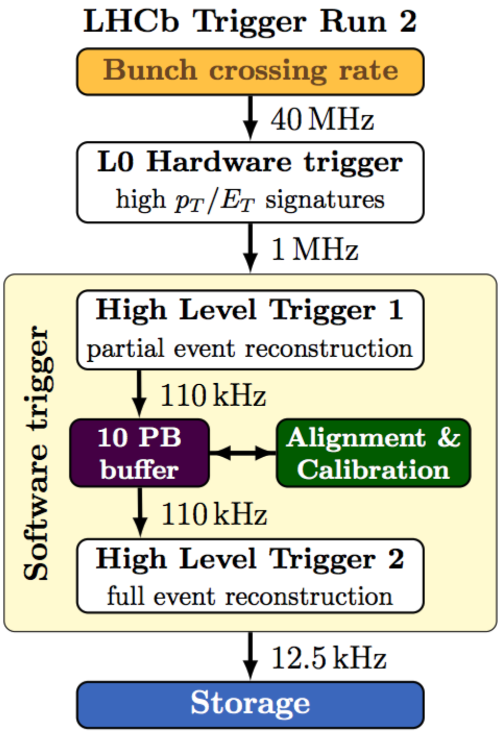

Figure 3.16 *The LHCb trigger system during Run II of data taking at the LHCb detector [30].*

The level 0 (L0) hardware trigger recused the pp bunch crossing rate of 40 MHz to 1 MHz within 6 μs. Due to the fast timing, it only uses information from the

VELO, calorimeters and muon chambers. Simple signatures of large transverse energy and momentum tracks are signs of heavy flavour interactions.

After readout, a 27.000 core CPU farm receives the events where they are further processed. The high-level trigger (HLT) 1 has 40 times more time than the L0 trigger and further reduces the rate to 100kHz. Fast reconstruction is performed to obtain the primary vertices and tracks above $p_{\mathrm{T}} > 500$ MeV, where most of the physics is retrieved using 1- and 2-track multivariate algorithms. The HLT1 trigger is over 95% efficient for beauty and over 70% for charm decays.

The second high-level trigger, HLT2, focuses on full event reconstruction using information from the entire detector. Both long and downstream tracks are available, in addition to full particle identification. Many inclusive and exclusive selections exist resulting in data sets ranging from roughly 5 MB to several hundred MB sent to storage to be used for offline analysis.

Chapter 4

Experimental status of Ξ_c^{**0}

4.1 Motivation

In 2017, the LHCb collaboration published the observation of five new narrow Ω_c^0 states decaying to the $\Xi_c^+ K^-$ final state [31]. It is currently not understood why these resonances are so narrow [32, 33]. Investigating a different charmed mass spectrum could lead to new insights. A natural extension to that analysis is the study of the $\Lambda_c^+ K^-$ spectrum. Throughout this this chapter, natural units are used where $\hbar = c = 1$.

Searches for Ξ_c^0 resonances have previously been performed in the $\Lambda_c^+ K^-$ mass spectrum by the Belle collaboration as well as the BaBar collaboration, but this is the first time it is being investigated using data collected by the LHCb experiment. In 2008, the BaBar collaboration [34] was the first to observe a structure in the $\Lambda_c^+ K^-$ mass spectrum in $B^- \to K^- \Lambda_c^+ \overline{\Lambda}_c^-$ decays peaking at 2.93 GeV, see Fig. 4.1(a). However, they did not claim the observation of a new state due to the lack of an amplitude analysis and limited data. Later that year, the BaBar collaboration performed an analysis looking at strongly interacting prompt decays of charm-strange baryons to several final states, one of which being $\Lambda_c^+ K^-$ [35]. No resonances were reported in the $\Lambda_c^+ K^-$ mass spectrum (Fig. 4.1(b)). Later on, the Belle collaboration reported a study of the $B^- \to K^- \Lambda_c^+ \overline{\Lambda}_c^-$ decays. They observed a peaking structure in the $\Lambda_c^+ K^-$ spectrum compatible to what BaBar spotted ten years before (Fig. 4.1(c)) and interpreted it as a new excited Ξ_c^0 baryon, dubbed $\Xi_c(2930)^0$, by a one-dimensional analysis. Similarly Belle has

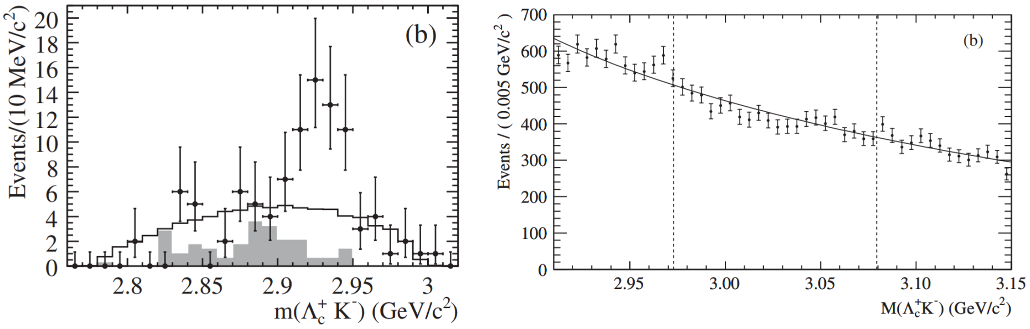

(a) *BaBar collaboration, 2008 [34].* **(b)** *BaBar collaboration, 2008 [35].*

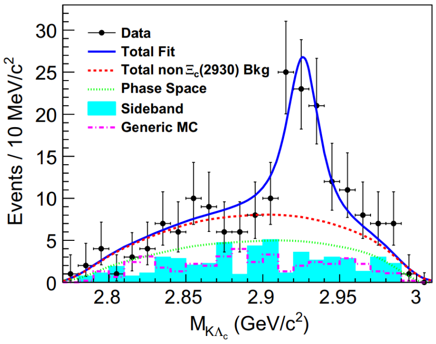

(c) *Belle collaboration, 2018 [37].*

Figure 4.1 *Previous studies performed on the $\Lambda_c^+ K^-$ mass spectrum by the Belle and BaBar collaborations, involving a prompt analysis (b), and the $\Lambda_c^+ K^-$ invariant mass spectrum from the $B^- \to K^- \Lambda_c^+ \overline{\Lambda}_c^-$ decays (a,c).*

also claimed the evidence of an isospin partner $\Xi_c(2930)^+$ in $\overline{B}^0 \to \overline{K}^0 \Lambda_c^+ \overline{\Lambda}_c^-$ decays [36].

Since the $\Lambda_c^+ K^-$ mass spectrum has not been investigated by the LHCb collaboration yet, it will be very interesting to see what we can add to these studies. In particular this analysis will focus on the search for excited Ξ_c^0 baryons in prompt production.

4.2 Experimental status

All singly-charmed ground states have been observed, however the quantum numbers of many of them are not measured. Excited states of Λ_c^+, Ξ_c, Σ_c and Ω_c^0 have been reported. The observed Ξ_c states, along with their measured masses and widths are listed in Tab. 4.1 [6]. The discovery of the $\Xi_c(3055)^0$ was claimed in 2016 by Belle [38] but has not been listed in the PDG.

Table 4.1 *List of observed excited Ξ_c states, along with their measured masses and widths. The spin-parities J^P are assigned according to the quark model and have not been measured for any state. A $****$ evidence denotes the existence of the particle is certain and its properties are fairly known. Three $***$ indicates a likely to certain existence but properties require further determinations. A state whose evidence of existence is only fair gets $**$, and one $*$ implies the evidence of existence is poor [6].*

Particle	Mass [MeV]	Width [MeV]	J^P	Evidence
Ξ_c^+	2467.93 ± 0.18	-	$1/2^+$	$***$
Ξ_c^0	2470.91 ± 0.25	-	$1/2^+$	$****$
$\Xi_c^{\prime +}$	2578.4 ± 0.5	-	$1/2^+$	$***$
$\Xi_c^{\prime 0}$	2579.2 ± 0.5	-	$1/2^+$	$***$
$\Xi_c(2645)^+$	2645.57 ± 0.26	2.14 ± 0.19	$3/2^+$	$***$
$\Xi_c(2645)^0$	2646.38 ± 0.21	2.35 ± 0.22	$3/2^+$	$***$
$\Xi_c(2790)^+$	2792.4 ± 0.5	8.9 ± 1.0	$1/2^-$	$***$
$\Xi_c(2790)^0$	2794.1 ± 0.5	10.0 ± 1.1	$1/2^-$	$***$
$\Xi_c(2815)^+$	2816.73 ± 0.21	2.43 ± 0.26	$3/2^-$	$***$
$\Xi_c(2815)^0$	2820.26 ± 0.27	2.54 ± 0.25	$3/2^-$	$***$
$\Xi_c(2930)^+$	2942 ± 5	15 ± 9	$?^?$	$**$
$\Xi_c(2930)^0$	$2929.7^{+2.8}_{-5.0}$	26 ± 8	$?^?$	$**$
$\Xi_c(2970)^+$	2969.4 ± 0.8	$20.9^{+2.4}_{-3.5}$	$?^?$	$***$
$\Xi_c(2970)^0$	$2967.8^{+0.9}_{-0.7}$	$28.1^{+3.4}_{-4.0}$	$?^?$	$***$
$\Xi_c(3055)^+$	3055.9 ± 0.4	7.8 ± 1.9	$?^?$	$***$
$\Xi_c(3055)^0$	3059.0 ± 1.1	6.4 ± 3.2	$?^?$	$***$
$\Xi_c(3080)^+$	3079.9 ± 1.4	5.6 ± 2.2	$?^?$	$***$
$\Xi_c(3080)^0$	3077.2 ± 0.4	3.6 ± 1.1	$?^?$	$***$
$\Xi_c(3123)^+$	3122.9 ± 1.3	4 ± 4	$?^?$	$*$

Table 4.2 *Decay modes of excited neutral Ξ_c^0 states. The $\Xi_c(3055)^0 \to \Lambda_c^+\pi^- K_s^0$ decay has not been observed. However the $\Xi_c(3055)^+ \to \Lambda_c^+\pi^+K^-$ decay has been reported.*

State	Decay modes
$\Xi_c'^0$	$\Xi_c^0\gamma$
$\Xi_c(2645)^0$	$\Xi_c^+\pi^-$
$\Xi_c(2790)^0$	$\Xi_c'^+\pi^-$
$\Xi_c(2815)^0$	$\Xi_c'^+\pi^-$ $\Xi_c(2645)^+\pi^-$
$\Xi_c(2930)^0$	$\Lambda_c^+K^-$
$\Xi_c(2970)^0$	$\Lambda_c^+\pi^-K_s^0$ $\to \Sigma_c(2455)^0K_s^0$ $\Xi_c'^+\pi^-$ $\Xi_c^0\pi^+\pi^-$ $\to \Xi_c(2645)^+\pi^-$
$\Xi_c(3055)^0$	ΛD^0 $\Lambda_c^+\pi^-K_s^0$ $\to \Sigma_c(2455)^0K_s^0$
$\Xi_c(3080)^0$	$\Lambda_c^+K_s^0\pi^-$ $\to \Sigma_c(2455)^0K_s^0$ $\to \Sigma_c(2520)^0K_s^0$ ΛD^0

4.2.1 Decays of the excited Ξ_c^0 states

Table 4.2 shows the decay modes that have been seen for the excited Ξ_c baryons. Note that some of these observations do not yet exceed the 5σ significance threshold.

The $\Xi_c(2970)$ baryon

The first mentioning of the $\Xi_c(2970)^+$ baryon appears in 2006 by the Belle collaboration [39]. The observation of the $\Xi_c(2970)^+$ state is reported in its decay to $\Lambda_c^+K^+\pi^-$, with a statistical significance of 5.7σ. They also search for the neutral isospin-partner, $\Xi_c(2970)^0$ in the $\Lambda_c^+K_S^0\pi^-$ final state. A small excess of events is seen around the expected $\Xi_c(2970)^0$ mass (Fig. 4.2(a)), however, the statistical significance is 1.5σ and therefore not sufficient to claim the observation

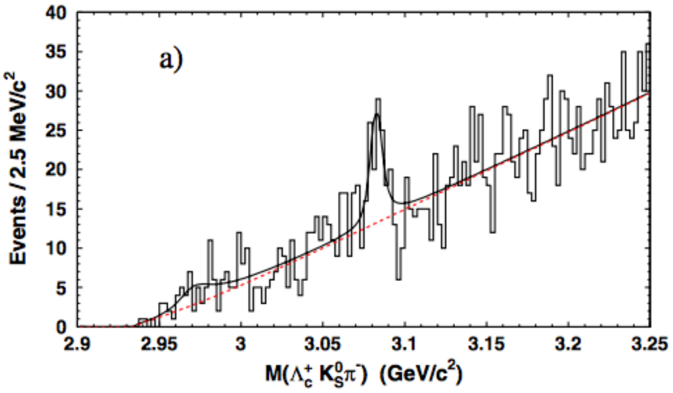

(a) *Belle collaboration [39].*

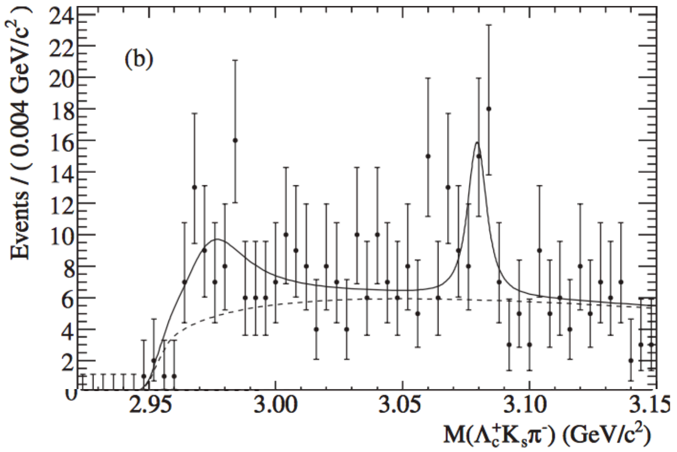

(b) *BaBar collaboration [40].*

Figure 4.2 *Search for the neutral $\Xi_c(2970)^0$ baryon in the invariant mass spectrum of the $\Lambda_c^+\pi^-K_S^0$ final state as performed by Belle (top), and the BaBar collaboration (bottom).*

of a new state.

Subsequently, in 2008, the BaBar collaboration searched for the neutral $\Xi_c(2970)^0$ baryon [40] in the same decay mode as Belle previously analysed. A statistically insignificant excess is seen with a significance of 1.7σ. This is the decay of the $\Xi_c(2970)^+ \to \Lambda_c^+ K^+ \pi^-$, the neutral isospin-partner (Fig. 4.2(b)).

Since the $\Xi_c(2970)^0$ baryon lies close to the $\Lambda_c^+ K_S^0 \pi^-$ mass threshold, this resonance is particularly difficult to model in this decay mode.

Another paper surrounding the $\Xi_c(2970)^0$ baryon was published by the Belle collaboration in 2008 [41], now studying the $\Xi_c(2645)^+\pi^-$ mass spectrum. The $\Xi_c(2970)^0$ baryon was found with a statistical significance of 6.1σ, as shown in Fig. 4.3. Additionally, the mass and width are measured. The mass is measured to be $2965.7 \pm 2.4(\mathrm{stat})^{+1.1}_{-1.2}(\mathrm{syst})\,\mathrm{MeV}/c$. The natural width of the resonance is found to be $\Gamma = 15 \pm 6 \pm 3$ MeV.

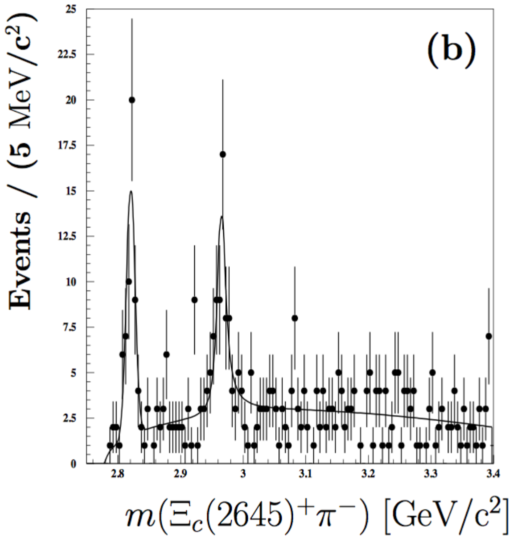

Figure 4.3 *Observation of the* $\Xi_c(2970)^0$ *baryon in the* $\Xi_c(2645)^+\pi^-$ *invariant mass spectrum by the Belle collaboration [41].*

An updated measurement on the $\Xi_c(2645)^+\pi^-$ mass spectrum was performed by Belle in 2016 [42]. The analysis studies the invariant mass spectrum from 2.84 to 3.10 GeV/c^2. In addition, the decay $\Xi_c(2970)^0 \rightarrow \Xi_c'^+\pi^-$ is observed (Fig. 4.4). The mass of the $\Xi_c(2970)^0$ is measured with respect to the mass of the Ξ_c^+ daughter particle as $M - M_{\Xi_c^+} = 499.9 \pm 0.7 \pm 0.2\,\mathrm{MeV}$, yielding a mass measurement of $2970.8 \pm 0.7 \pm 0.2^{+0.3}_{-0.4}\,\mathrm{MeV}$. The natural width is measured as $\Gamma = 28.1 \pm 2.4^{+1.0}_{-5.0}\,\mathrm{MeV}$. A small peak around 2920 MeV is observed and it is more apparent in the neutral channel. Including a signal component to account for the small excess of events around 2920 MeV slightly lowers the width of the $\Xi_c(2970)^0$ baryon, which has been taken into account during systematic studies. According to the Belle collaboration, this measurement was independent from the measurement published in 2008 [41].

The previous mass and width measurements of the $\Xi_c(2970)^0$ baryon, discussed in this subsection, are summarised in Tab. 4.3.

4.2.2 Search for Ξ_c^{**0} decaying to $\Lambda_c^+ K^-$

The study and observation of the excited Ξ_c^0 states will be of great interest to test the validity of HQET. In addition, by studying another charmed mass

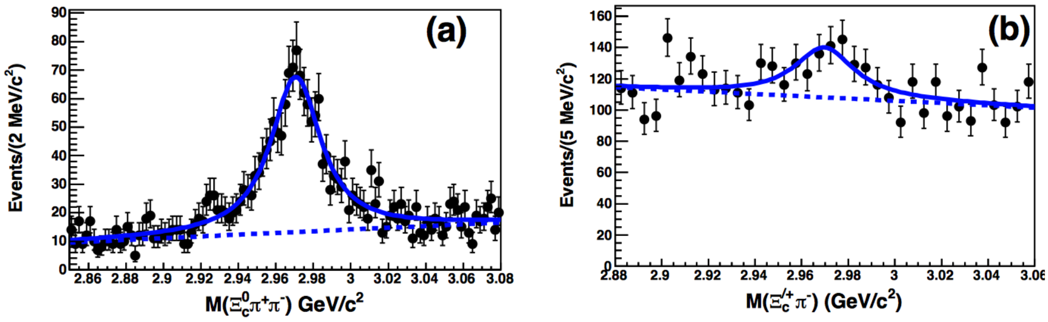

Figure 4.4 *Invariant mass spectrum for* $\Xi_c^0\pi^+\pi^-$ *candidates. The mass and width of the* $\Xi_c(2970)^0$ *baryon are measured in the decay (a)* $\Xi_c(2970)^0 \to \Xi_c(2645)^+(\to \Xi_c^0\pi^+)\pi^-$ *and (b)* $\Xi_c(2970)^0 \to \Xi_c'^+\pi^-$ *by the Belle collaboration [42]. Mass resolutions in this analysis are about 2* MeV*.*

Table 4.3 *Mass and width measurements of the* $\Xi_c(2970)^0$ *baryon, in chronological order.*

Collaboration	Decay Mode	Mass [MeV]	Width [MeV]	Significance	Reference
Belle	$\Lambda_c^+\pi^-K_S^0$	$2977.1 \pm 8.8 \pm 3.5$	-	1.5σ	[39]
Babar	$\Lambda_c^+\pi^-K_S^0$	$2972.9 \pm 4.4 \pm 1.6$	$31 \pm 7 \pm 8$	1.7σ	[40]
Belle	$\Xi_c(2645)^+\pi^-$	$2965.7 \pm 2.4^{+1.1}_{-1.2}$	$15 \pm 6 \pm 3$	6.1σ	[41]
Belle	$\Xi_c(2645)^+\pi^-$ $\Xi_c'\pi^-$	$2970.8 \pm 0.7 \pm 0.2^{+0.3}_{-0.4}$	$30.3 \pm 2.3^{+1.0}_{-1.8}$	$> 5\sigma$	[42]
PDG		$2967.8^{+0.9}_{-0.7}$	$28.1^{+3.4}_{-4.0}$		

spectrum, we might understand why the five new Ω_c^0 states decaying to $\Xi_c^+K^-$ final state [31] are so narrow. The equal spacing rule, formulated by Gell-Mann [43] and Okubo [44], could help us to interpret the excited state spectrum:

$$m(\Omega_c^{**}) - m(\Xi_c^{**}) = m(\Xi_c^{**}) - m(\Sigma_c^{**}). \tag{4.1}$$

For example the above formula, applied to the states in the $J^P = 3/2^+$ multiplet (Fig. 2.4(c)), returns:

$$m_{\Omega_c(2770)^0} - m_{\Xi_c(2645)} \simeq m_{\Xi_c(2645)} - m_{\Sigma_c(2520)} \simeq 125\,\text{MeV}. \tag{4.2}$$

The subject of this thesis is the $\Lambda_c^+K^-$ channel. The lowest mass excited states expected from theoretical predictions, as shown in Fig. 2.7, all lie above the $\Lambda_c^+K^-$ mass threshold. The lowest order Feynman diagram is shown in Fig. 4.5.

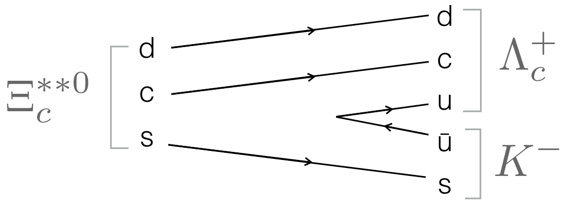

Figure 4.5 *The lowest order Feynman diagram of the* $\Xi_c^0 \to \Lambda_c^+ K^-$ *decay.*

Chapter 5

Selection of the $\Lambda_c^+ K^-$ candidates

In the following chapter, the observation of new excited Ξ_c^0 resonances is described. The aim of this analysis is to observe and study Ξ_c^{**0} states in their decay to the charmed Λ_c^+ baryon and a K^- meson, where the Λ_c^+ decays further into a proton, a K^- meson and a π^+ meson. This is the first time this mass spectrum is analysed using data collected at the LHCb detector. This chapter describes the process required to select the $\Lambda_c^+ K^-$ signal candidates. In chapter 6, the analysis of the selected candidates is discussed in detail.

5.1 Analysis strategy

The study described in this chapter requires a sample of $\mathit{\Lambda}_c^+ K^-$ candidates, where the $\mathit{\Lambda}_c^+$ baryon and the K^- meson are created at the pp interaction point. The $\mathit{\Lambda}_c^+$ baryon travels away from the Primary Vertex (PV) where it was created, before decaying further at the so-called Secondary Vertex (SV). In the LHCb detector, $\mathit{\Lambda}_c^+$ baryons travel on the order or 1 mm before decaying further. A so called prompt decay, where the daughter particles are created at the pp interaction point, typically has a higher amount of background events. To separate the signal events from background, a careful event selection is used. First, events are required to pass a Turbo line, which is essentially a collection of selection requirements. This greatly reduces the event size in real-time while data are being taken (Sec. 5.4). An offline pre-selection follows (Sec. 5.5), after which a high purity sample of $\mathit{\Lambda}_c^+ \to pK^-\pi^+$ decays is selected using a multivariate technique, as described in Sec. 5.6. This sample is combined with a K^- meson, from here on referred to as the bachelor kaon, to create the $\Lambda_c^+ K^-$ invariant mass spectrum of interest. Section 5.8 outlines further selections applied to the $\Lambda_c^+ K^-$ invariant mass spectrum. The selected data set is analysed in chapter 6, where a fit to the data is performed to extract the mass and width of the new states. Throughout this analysis, charge conjugate processes are also considered.

5.2 Data sets

The data samples used in this analysis were collected by the LHCb detector in pp collisions at $\sqrt{s} = 13$ TeV. The data set consists of $1.67\,\mathrm{fb}^{-1}$ collected in 2016, $1.71\,\mathrm{fb}^{-1}$ in 2017 and $2.19\,\mathrm{fb}^{-1}$ acquired in 2018, respectively, combining to a total sample consisting of $5.57\,\mathrm{fb}^{-1}$. The LHCb collaboration also collected data in 2011, 2012 and 2015. These data are not studied in this analysis since no dedicated Turbo line to select candidates exists.

5.2.1 Simulated data sets

In the LHCb experiment, simulated data sets are generated to model the decays used in each analysis. In the analysis described in this thesis, the simulated data samples are used to extract the detector mass resolution and to model the shape of the background samples. The pp collision is simulated using a package called Pythia [45], a general purpose generator, which is also responsible for the modelling of the hadronisation process. The particle decays are simulated using a different package, called EvtGen [46], where the decay products are generated across the entire available phase space. The generated signal events and all signal decay products are required to fall within the LHCb acceptance. The detector model used in the simulations is build using the Geant4 package [47].

Samples of $\Xi_c^{**0} \to \Lambda_c^+ K^-$ have been simulated with different masses and widths, as shown in the top section of Tab 5.1. All samples are simulated using the detector conditions from data taking at LHCb in the year 2016. Five samples are generated, including three samples of the decays of the resonances studied in this analysis. Two additional samples are simulated, where the lightest Ξ_c^{**0} mass chosen corresponds to the lightest known Ξ_c^{**0} above the $\Lambda_c^+ K^-$ threshold and the heaviest Ξ_c^{**0} sample generated corresponds to the currently heaviest known Ξ_c^{**0} resonance (3080 MeV). Note that we did not choose to generate the $\Xi_c(3123)$ since its existence is uncertain, as shown in Tab. 4.1. Since the analysis reports the observation of several new resonances, the masses of these resonances are unknown. Therefore, two separately simulated $\mathit{\Xi}_c(X)^0 \to \mathit{\Lambda}_c^+ K^-$ decays are generated, where X denotes the mass of the resonance which is estimated by performing a fit to the $\mathit{\Lambda}_c^+ K^-$ mass spectrum where the signal peaks are visible through a non-optimised selection, loosely based on the selection requirements used in the analysis of Ω_c resonances in the $\Xi_c^+ K^-$ mass spectrum [31]. The first set of generated MC simulations, generated with simulation version Sim08f, are produced in the decay chain

$$\Xi_c^{**}(X)^0 \to \mathit{\Lambda}_c^+(\to pK^-\pi^+)K^- \tag{5.1}$$

where X indicates the mass of the Ξ_c^{**0} resonance. The $\mathit{\Xi}_c(X)^{**0} \to \mathit{\Lambda}_c^+ K^-$ samples are used to calculate the mass resolution (Sec. 6.1).

As the analysis progressed, further MC samples were requested to model several background components (Sec. 6.2). These simulations are generated with simulation version Sim09h. The simulation version has changed with respect to the $\Xi_c^{**0} \to \Lambda_c^+ K^-$ samples due to their later generation, but the changes in the simulation version does not affect the decays studied in this analysis. The decays are produced in the decay chain

$$\Xi_c^{**}(X)^+ \to \Sigma_c^{(*)++}(\to \mathit{\Lambda}_c^+(\to pK^-\pi^+)\pi^+)K^- \tag{5.2}$$

To increase the statistics in the fully selection samples, larger numbers of $\mathit{\Xi}_c(3055)^+ \to \Sigma_c^{++} K^-$ and $\mathit{\Xi}_c(3080)^+ \to \Sigma_c^{++} K^-$ decays are used. A reasonably sized sample of events is required in the selected simulated data sets to model the shape of these two decays in the fit to the data (Sec. 6.3).

A process called truth-matching is applied to the simulated data. The simulated data consists of reconstructed objects, for example particle tracks, clusters in the calorimeters and hits in the RICH detectors. These objects need to be matched to the same generated objects. This process ensures the reconstructed tracks in the simulated data set are associated with the correct particle hypothesis.

Furthermore, a well known feature within the LHCb simulation is that it does not accurately model the data distributions of particle identification variables. To

Table 5.1 *Simulated data samples used in the analysis, where X indicates the mass of the Ξ_c^{**0} resonance.*

Description	Sample Size	$m(\Xi_c^{**0})$ [MeV]	$\Gamma(\Xi_c^{**0})$ [MeV]
$\Xi_c(2790)^0 \to \Lambda_c^+ K^-$	1M	2790	10
$\Xi_c(X)^0 \to \Lambda_c^+ K^-$	1M	2923	10
$\Xi_c(X)^0 \to \Lambda_c^+ K^-$	1M	2939	10
$\Xi_c(2970)^0 \to \Lambda_c^+ K^-$	1M	2968	28
$\Xi_c(3080)^0 \to \Lambda_c^+ K^-$	1M	3080	5.6
$\Xi_c(3055)^+ \to \Sigma_c^{++} K^-$	5M	3055	7.8
$\Xi_c(3080)^+ \to \Sigma_c^{++} K^-$	5M	3077	3.6
$\Xi_c(3080)^+ \to \Sigma_c^{*++} K^-$	1M	3077	3.6

counteract this, the PID variables are re-weighted using a corrective weighting. This software corrects the PID response for simulated data samples using PID calibration data. For hadrons, high-statistics calibration samples of $D^{*+} \to D^0\pi^+, \Lambda \to p\pi^-$ and $\Lambda_c^+ \to pK^-\pi^+$ decays are used. Muon PID is corrected by using the clean, low background $J/\psi \to \mu^+\mu^-$ decay, and electron PID is revised using $B^+ \to J/\psi(\to e^+e^-)K^+$ samples. The momentum and pseudorapidity of the signal tracks and the event multiplicity are used to generate the PID corrections.

5.3 Selection strategy

A typical event recorded at LHCb contains many tracks, resulting in an enormous amount of data gathered. It is essential to reduce the full data set to a smaller sample of a more manageable size whilst keeping the signal candidates. The kinematic and topological characteristics of the decay are exploited in the selection process to achieve this. This section describes the selection process, which consists of four stages:

- Selection at trigger level through Turbo lines.
- Offline pre-selection.
- A multivariate selection to select a high purity sample of $\Lambda_c^+ \to pK^-\pi^+$ decays.
- Selection of the bachelor kaon.

In addition to selecting a sample of $\Lambda_c^+ K^-$ candidates, the same selection requirements are applied to a sample of $\Lambda_c^+ K^+$ candidates. This is the so-called Wrong-Sign (WS) sample, where no resonant structures are expected. This is because the decay $\mathit{\Xi}_c^0 \rightarrow \Lambda_c^+ K^+$ violates charge conservation.

At the LHCb experiment, there are several decay properties which are typically exploited when events are selected. Tracks not originating from the PV are expected to have a large impact parameter, generally quantified using χ^2_{IP}. The impact parameter is defined at the transverse distance of closest approach between a particles path and a vertex. The χ^2_{IP} is defined as the difference in the vertex-fit χ^2 of a given PV reconstructed with and without the track being considered. Particles which do originate from the PV are required to have a small impact parameter. In addition, the decay of a heavy hadron usually leads to daughter particles with a relatively large transverse momentum, p_T, compared to background events. This is a consequence of the heavy mass of the parent. Furthermore, the LHCb detector provides excellent particle identification (PID) due to the RICH detectors. This is exploited to separate protons, kaons and pions, which is of utmost importance in hadronic decay modes such as the $\Xi_c^0 \rightarrow \Lambda_c^+ K^-$ decay.

5.4 Selection at trigger level (Turbo)

At trigger level, selected events are required to pass a Turbo line. In a pp interaction at LHCb, roughly 40 tracks are associated with the primary vertex, whereas only 2-6 tracks are typically necessary to reconstruct a heavy flavour decay. A Turbo line discards certain tracks to significantly reduce the event size whilst keeping the data required to perform the analysis. The turbo line used in this analysis selects Λ_c^+ candidates decaying to a proton, a negative kaon and a positive pion[1]. For data taken in 2016, this Turbo line is implemented using Turbo++ (Full Persistence). All candidates that fire on the turbo line including their full decay tree are saved. In addition, all long and downstream tracks, VELO tracks and PID objects are kept, as shown in the bottom of Fig. 5.1. In 2017 and 2018, the turbo line was changed to Turbo Selective Persistence (SP). For TurboSP, the candidate that triggered the line is stored, along with a further selection which can be specified in the Turbo line. This allows for a further

---

[1] The Turbo line used is called the **Hlt2CharmHadLcpToPpKmPipTurbo**

reduction in the event size. In this analysis, a subset of tracks coming from the PV associated to the Λ_c^+ candidate are saved, together with any tracks consistent with originating from the Λ_c^+.

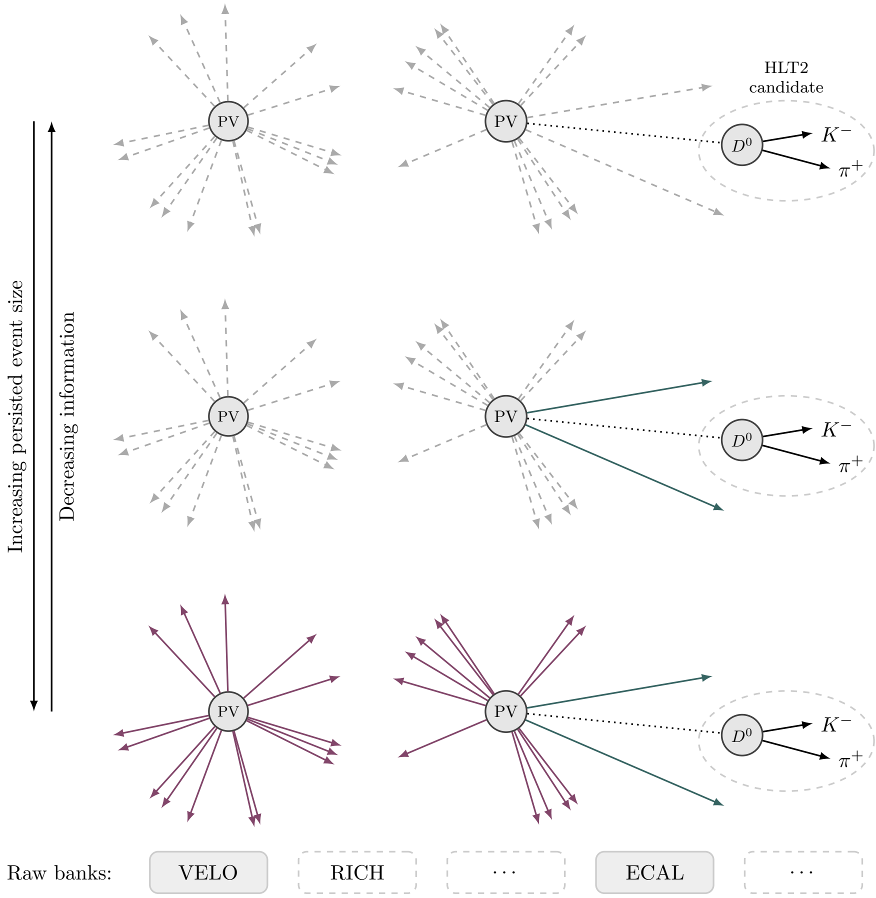

Figure 5.1 *The difference between the varying levels of persistence used at LHCb is shown for the same reconstructed event. The top plot shows Turbo, selective persistence is shown in the middle and a complete reconstruction (full) persistence is given in the bottom plot. In each case, the solid lines indicate which information is stored. Figure taken from [48].*

The Λ_c^+ selection criteria of the turbo line are shown in Tab. 5.2, where the difference in selection between 2016 and 2017/2018 data is indicated. Care is taken to mitigate any potential effect due to the difference in 2016 and 2017/2018 data taking (Sec. 5.3) by applying the requirements in the bottom half of Tab. 5.2 to the 2016 candidates offline.

Table 5.2 *Selection criteria implemented in the turbo line used for the optimisation of the Λ_c^+ selection (Hlt2CharmHadLcpToPpKmPipTurbo).*

Candidate	Variable	Requirement
Daughters of Λ_c^+	RICH information saved	yes
	Largest χ^2_{IP}	> 16
	Second largest χ^2_{IP}	>9
	Third largest χ^2_{IP}	> 6
	Largest P_T	> 1000 MeV
	Second largest P_T	> 400 MeV
	Third largest P_T	> 200 MeV
	Sum of daughter P_T	> 3000 MeV
	Proton PID	$PID_p > 5$
	Proton PID	$PID_p - PID_k > 5$
	Kaon PID	$PID_k > 5$
	Pion PID	$PID_k < 5$
	Proton momentum	$P_p > 10000$ MeV
Λ_c^+	Vertex quality	$\chi^2_{VTX}/ndf < 10$
	Decay time	$\tau > 0.15$ ps
	Cosine of direction angle	< 10 mrad
	χ^2 distance from related PV	> 25
	Invariant $pK^-\pi^+$ mass	[2211,2362] MeV

Only for 2017 and 2018 datasets

Λ_c^+	Decay time	$\tau > 0.3$ ps
	χ^2_{IP}	< 15
	Momentum	> 30000 MeV
	Transverse momentum	> 2000 MeV
Bachelor Kaon	χ^2_{IP}	< 15
	Track quality	$\chi^2_{TRACK} < 3$
	Ghost probability	< 0.4
	Transverse momentum	> 500 MeV
	Momentum	> 1000 MeV
	Kaon PID	$PID_k > 10$
Ξ_c^0 candidate	Vertex quality	$\chi^2_{VTX}/ndf < 10$
	Invariant mass	$m_{\Lambda_c^+ K^\mp} - m_{\Lambda_c^+} - m_{K^\mp} < 855$ MeV

Table 5.3 *Pre-selection criteria applied during offline processing.*

Candidate	Variable	Requirement
Λ_c^+ mother	χ^2_{IP}	< 9
Bachelor Kaon	χ^2_{IP}	< 9
	Ghost probability	< 0.3
	Kaon PID	$\mathrm{Prob}_k > 0.1$
	Transverse momentum	> 250 MeV
Kaon	Mass	$m_{\Lambda_c^+ K^\mp} - m_{\Lambda_c^+} < 1100$ MeV
	Vertex quality	$\chi^2_{VTX}/ndf < 20$

5.5 Offline processing

Only the events recorded by the Turbo trigger are selected for further processing. The number of events in the samples is reduced more through offline processing. The Λ_c^+ ($\Lambda_c^+ K^\mp$) candidates are refitted using the DecayTreeFitter tool [49]. This tool performs a simultaneous fit to the whole decay chain to improve the mass resolution. In addition, it constrains the Λ_c^+ (and $K^\mp$) candidates to stem from the primary vertex (PV). The track momenta are rescaled according to momentum scale calibration tools [50, 51] to further increase the decay reconstruction accuracy. In addition, several additional selection requirements are applied during the offline processing to reduce the size of the data samples. These are summarised in Tab. 5.3.

5.6 Λ_c^+ selection

The optimisation of the selection of $\Lambda_c^+ \to pK^-\pi^+$ events is performed on a small portion of all available $\Lambda_c^+ \to pK^-\pi^+$ events. Due to the large production cross-section of Λ_c^+ particles at the LHC there is an enormous amount of $\Lambda_c^+ \to pK^-\pi^+$ candidates. To reduce the size of the data set, a sub-sample consisting of approximately 20% of the 2016 data is utilised for the Λ_c^+ selection. All figures displayed in this section are created only using the small sample. Note that the analysis of the $\Lambda_c^+ K^-$ sample is performed on the full 2016 to 2018 data available.

After the Turbo selection and the offline pre-selection, a relatively clean sample of the $\Lambda_c^+ \to pK^-\pi^+$ decay is obtained with a peak around the Λ_c^+ mass in the $pK^-\pi^+$ invariant mass spectrum shown in Fig 5.2. A fit is superimposed, where the probability density function (PDF) for the signal Λ_c^+ peak consists of the sum

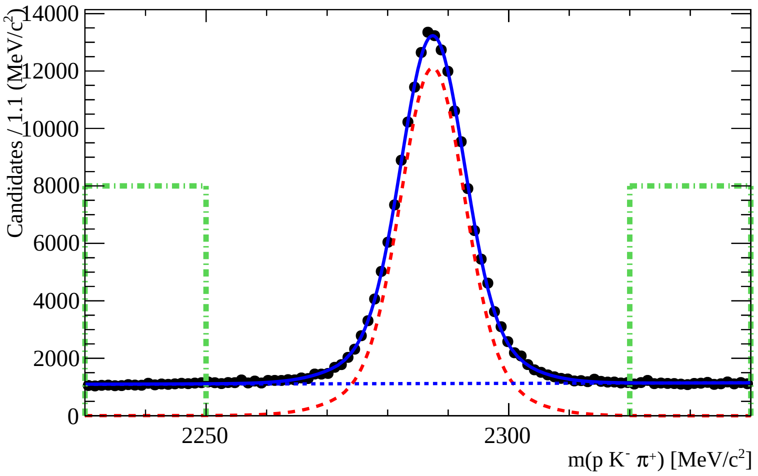

Figure 5.2 *Plot shows the $pK^-\pi^+$ invariant mass spectrum. The black dots are data. A fit to the data is superimposed, where the blue solid line gives the result of the fit. The dashed red line shows the $\Lambda_c^+ \to pK^-\pi^+$ contribution and consists of the addition of a Gaussian and a Crystal Ball function which share a mean. The combinatorial background is modelled using a first order Chebychev polynomial and is shown by the blue dotted line. The green dashed lines indicate the upper and lower sidebands used as input to the multivariate analysis.*

of a Gaussian function and a Crystal Ball function with a shared mean. A Crystal Ball function comprises a Gaussian core and a power-law lower mass radiative tail, where both the function and its first derivative are continuous [52] and is given by:

$$f(x;\alpha,n,\bar{x},\sigma) = N \times \begin{cases} \exp\left(-\frac{(x-\bar{x})^2}{2\sigma^2}\right), & \text{for } \frac{x-\bar{x}}{\sigma} > -\alpha \\ A \times \left(B - \frac{x-\bar{x}}{\sigma}\right)^{-n}, & \text{for } \frac{x-\bar{x}}{\sigma} \leq -\alpha \end{cases} \tag{5.3}$$

where

$$\begin{aligned} A &= \left(\frac{n}{|\alpha|}\right)^n \times \exp\left(-\frac{|\alpha|^2}{2}\right) \\ B &= \frac{n}{|\alpha|} - |\alpha| \\ N &= \frac{1}{\sigma(C+D)} \\ C &= \frac{n}{|\alpha|} \times \frac{1}{n-1} \times \exp\left(-\frac{|\alpha|^2}{2}\right) \\ D &= \sqrt{\frac{\pi}{2}}\left(1 + \operatorname{erf}\left(\frac{|\alpha|}{\sqrt{2}}\right)\right) \end{aligned} \tag{5.4}$$

The normalisation factor is N, and α, n, $\bar{x}$ and σ are fit parameters of the function. The combinatorial background is modelled using a first order Chebychev polynomial. The fit results are

$$m(\Lambda_c^+) = 2287.44 \pm 0.02\,\mathrm{MeV}/c^2, \quad \sigma = 6.72 \pm 0.30\,\mathrm{MeV}/c^2 \tag{5.5}$$

where σ is the resolution of the signal PDF, calculated using the width of the Gaussian function and the width of the Crystal Ball function as

$$\sigma = \sqrt{(1-f)\sigma_G^2 + f\sigma_{CB}^2}. \tag{5.6}$$

From the fit, we extract the width of the Gaussian function, σ_G as 9.82 ± 0.43 MeV and the width of the Crystal Ball function $\sigma_{CB} = 5.07 \pm 0.07$ MeV. The parameter $f = 0.73 \pm 0.03$ is the fraction of the Crystal Ball function in the signal yield. The Crystal Ball tail parameter, n, is fixed to one to ensure fit stability, and α is fitted to be 3.06 ± 0.24.

5.6.1 Multivariate selection

A multivariate selection process is used to further choose $\Lambda_c^+ \to pK^-\pi^+$ candidates. Combining the information from multiple input variables typically provides a more efficient method to discriminate signal from background events than the simple cut-based selections described earlier in this chapter. The multivariate selection is performed using a software package called 'A Toolkit for MultiVariate Analysis' (TMVA) [53]. This software package is integrated in the ROOT framework [54] and provides the evaluation of many different multivariate classification techniques, such as boosted decision trees and neural networks. The package yields a single response variable for each separate classification technique, to which a square cut-based selection can be applied. The TMVA tool requires a sample of signal-like candidates and a sample of background events to be trained on, such that the algorithm can learn their properties.

In most cases, simulated events are used as signal input to a multivariate analysis. Since at the time no simulation was available for the $\Lambda_c^+ \to pK^-\pi^+$ decay, the multivariate analysis described here utilises roughly 1% of the $\Lambda_c^+ \to pK^-\pi^+$ events as signal input. The background has been subtracted using the *sPlot* method [55] using the fit shown in Fig. 5.2. This generates so-called s-weights, where every event gets assigned a weight depending on its likelihood to be signal or background. Generally one should only use this method for cases where the variable of interest is uncorrelated with the variable used for the background subtraction. In the case of this analysis, these variable are the same and are thus fully correlated. This might introduce a slight bias in the selection of the $\mathit{\Lambda}_c^+ \to pK^-\pi^+$ sample. However, it should not affect the $\mathit{\Xi}_c^0$ candidates in the $\mathit{\Lambda}_c^+ K^-$

Table 5.4 *List of discriminating variables used in the multivariate selection of the $\Lambda_c^+ \to pK^-\pi^+$ candidates.*

	Variable	Definition
1	$\log(\chi^2_{VTX})$	Vertex fit quality (not χ^2_{VTX}/ndf)
2	$\log(\chi^2_{FD})$	χ^2 of the flight distance (FD) of the Ξ_c^0 from the PV.
3	$\log(1\text{-DIRA}_{\Lambda_c^+})$	Cosine of the direction angle (DIRA).
4	$\log(\chi^2_{IP})$	Impact parameter χ^2_{IP} of the Λ_c^+ candidate with respect to the primary vertex and the Λ_c^+ daughters with respect to the Λ_c^+ decay vertex.
5	$\log(p_T)$	Transverse momentum of the Λ_c^+ daughters, p, K^- and π^+.
6	$1\text{-}\sqrt{1-\text{Prob}_{p,K^-,\pi^+}}$	Probability that the daughter particles of the Λ_c^+ are correctly identified.

mass spectrum, which is the main subject of this analysis.

As background input to the BDT, the lower and upper sidebands of the $pK^-\pi^+$ invariant mass distribution, ranging from $2230 - 2250\,\text{MeV}/c^2$ and $2320 - 2340\,\text{MeV}/c^2$, are taken. The sideband regions are indicated by the green dashed lines in Fig. 5.2. Note the vertical lines in the lowest and highest bins.

In addition to a signal and a background sample, a list of discriminating variables is required. The variables provided to the multi-variate selection are carefully selected to have a relatively high discriminating power between the signal and background samples. The variables used are the vertex fit quality, the χ^2 of the flight distance of the Ξ_c^0 from the PV, the cosine of the direction angle, the impact parameter χ^2_{IP} of the Λ_c^+ candidate with respect to the primary vertex, the χ^2_{IP} of the Λ_c^+ daughter candidates with respect to the Λ_c^+ decay vertex, the transverse momentum, p_{T}, of the Λ_c^+ daughters and the particle identification probabilities of the Λ_c^+ daughter particles. The direction angle is defined as the angle between the direction of momentum of the Ξ_c^0 and the line between the PV and the SV. These variables are listed in Tab. 5.4. In most cases, the logarithm of the variable is chosen as the discriminating variable, to show their discriminating power. This is especially effective for variables that have many entries with values close to zero.

The comparison of signal and background distributions of the variables listed in Tab. 5.4 are shown in Fig. 5.3, and the correlations between the variables in both the signal and background samples are shown in Fig. 5.4. A larger difference between the two distributions implies the variable has a higher discriminating power.

The TMVA program randomly splits the signal and background samples into two separate subsets, one of which is used to train the multivariate classifiers and the other to test the response. The discriminating power of the various methods is displayed in a receiver operator characteristic (ROC)-curve (Fig. 5.5), which gives the signal efficiency in comparison to the background rejection of each method. As can be seen in the ROC-curve, the algorithms considered are a standard Boosted Decision Tree (BDT), a Gradient Boosted Decision Tree (BDTG) two different Multi-Layer Perceptron neural networks (MLP and MLPBNN) and a linear method, Fisher. The methods considered each perform comparably, and the choice was made to use the BDTG algorithm in the analysis.

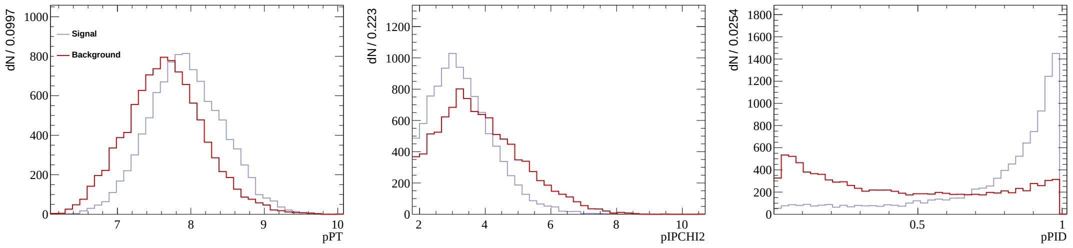

(a) *Proton* p_T **(b)** *Proton* χ^2_{IP} **(c)** PID_p

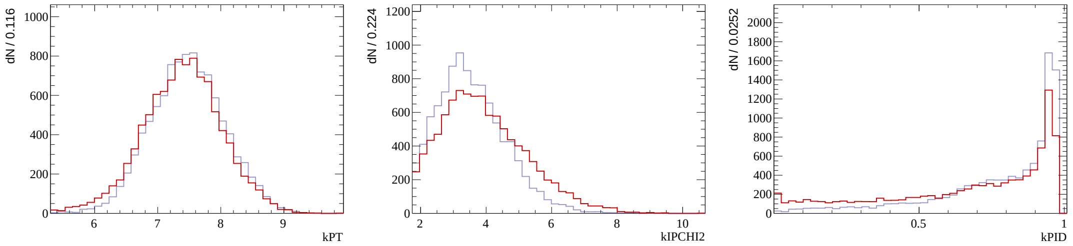

(d) *Kaon* p_T **(e)** *Kaon* χ^2_{IP} **(f)** PID_k

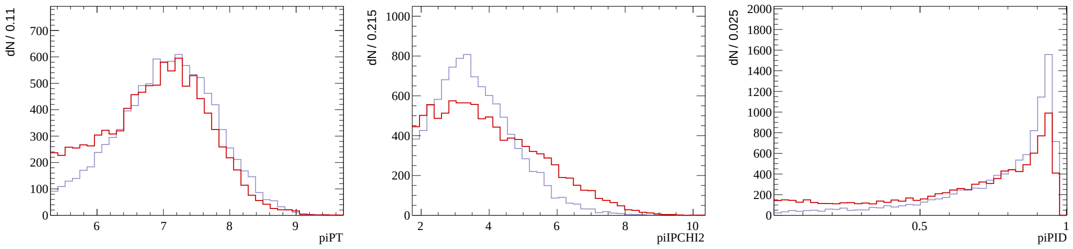

(g) *Pion* p_T **(h)** *Pion* χ^2_{IP} **(i)** PID_π

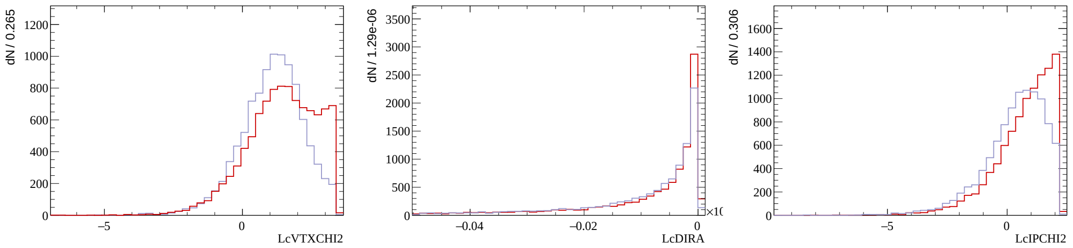

(j) χ^2_{VTX} *of the* Λ_c^+ **(k)** *DIRA of the* Λ_c^+ **(l)** Λ_c^+ χ^2_{IP}

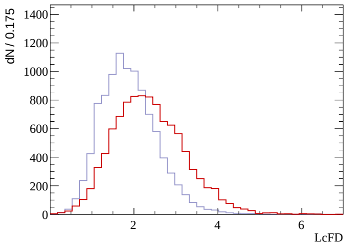

(m) *FD of the* Λ_c^+

Figure 5.3 *Distributions of the observables for signal (grey) and background (red) from the 2016 data sample used to train the multivariate selection.*

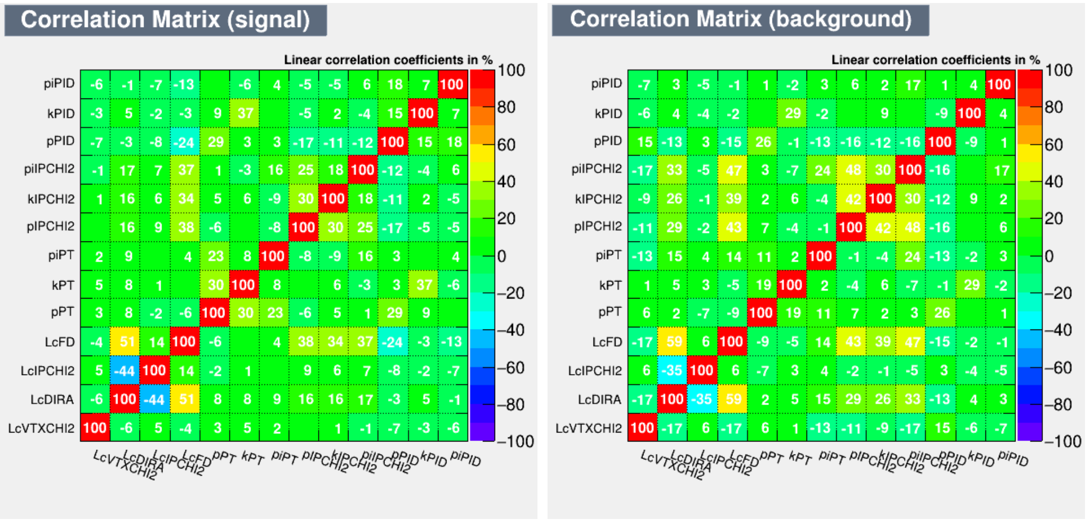

Correlation Matrix (signal)

Linear correlation coefficients in %

	LcVTXCHI2	LcDIRA	LcIPCHI2	LcFD	pPT	kPT	piPT	pIPCHI2	kIPCHI2	piIPCHI2	pPID	kPID	piPID
piPID	-6	-1	-7	-13		-6	4	-5	-5	6	18	7	100
kPID	-3	5	-2	-3	9	37		-5	2	-4	15	100	7
pPID	-7	-3	-8	-24	29	3	3	-17	-11	-12	100	15	18
piIPCHI2	-1	17	7	37	1	-3	16	25	18	100	-12	-4	6
kIPCHI2	1	16	6	34	5	6	-9	30	100	18	-11	2	-5
pIPCHI2		16	9	38	-6		-8	100	30	25	-17	-5	-5
piPT	2	9		4	23	8	100	-8	-9	16	3		4
kPT	5	8	1		30	100	8		6	-3	3	37	-6
pPT	3	8	-2	-6	100	30	23	-6	5	1	29	9	
LcFD	-4	51	14	100	-6		4	38	34	37	-24	-3	-13
LcIPCHI2	5	-44	100	14	-2	1		9	6	7	-8	-2	-7
LcDIRA	-6	100	-44	51	8	8	9	16	16	17	-3	5	-1
LcVTXCHI2	100	-6	5	-4	3	5	2		1	-1	-7	-3	-6

Correlation Matrix (background)

Linear correlation coefficients in %

	LcVTXCHI2	LcDIRA	LcIPCHI2	LcFD	pPT	kPT	piPT	pIPCHI2	kIPCHI2	piIPCHI2	pPID	kPID	piPID
piPID	-7	3	-5	-1	1	-2	3	6	2	17	1	4	100
kPID	-6	4	-4	-2		29	-2		9		-9	100	4
pPID	15	-13	3	-15	26	-1	-13	-16	-12	-16	100	-9	1
piIPCHI2	-17	33	-5	47	3	-7	24	48	30	100	-16		17
kIPCHI2	-9	26	-1	39	2	6	-4	42	100	30	-12	9	2
pIPCHI2	-11	29	-2	43	7	-4	-1	100	42	48	-16		6
piPT	-13	15	4	14	11	2	100	-1	-4	24	-13	-2	3
kPT	1	5	3	-5	19	100	2	-4	6	-7	-1	29	-2
pPT	6	2	-7	-9	100	19	11	7	2	3	26		1
LcFD	-17	59	6	100	-9	-5	14	43	39	47	-15	-2	-1
LcIPCHI2	6	-35	100	6	-7	3	4	-2	-1	-5	3	-4	-5
LcDIRA	-17	100	-35	59	2	5	15	29	26	33	-13	4	3
LcVTXCHI2	100	-17	6	-17	6	1	-13	-11	-9	-17	15	-6	-7

Figure 5.4 *Correlation matrix between the input variables for the multivariate analysis for the signal (left) sample and the background (right) sample..*

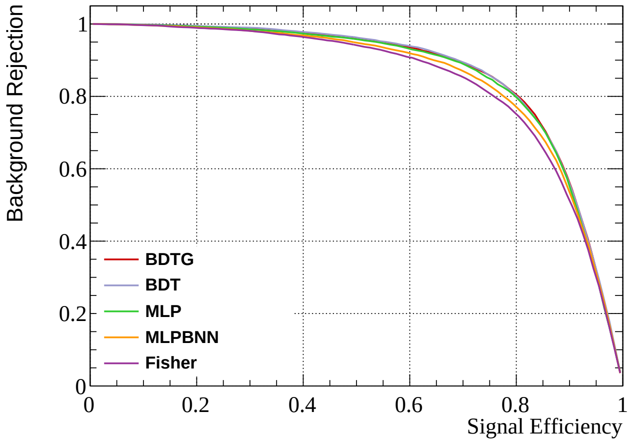

Figure 5.5 *ROC-curve used to determine the best multivariate method to select the $\Lambda_c^+ \to pK^-\pi^+$ signal events.*

While training an algorithm, one needs to be careful to check whether the training can be extrapolated to the full data set. Due to the relatively low number of events in the samples, an over-training check was performed, as shown in Fig. 5.6. This figure shows the distributions of the classifier response for the training and the testing sample, for the background events and the signal events. A good agreement between the training and testing samples, as is the case here, implies the sample size used is large enough.

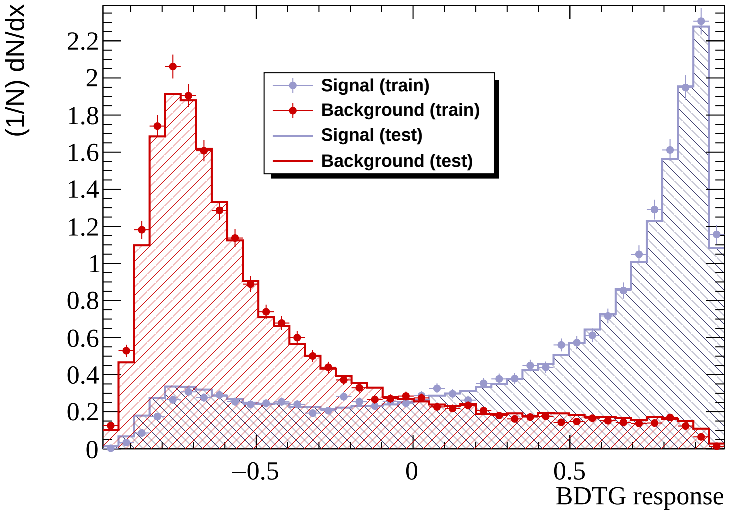

Figure 5.6 *The overtraining test for the BDTG method, where the training sample distributions are shown by the red (background) and grey (signal) points. The test sample distributions are indicated by the shaded histograms in red (background) and grey (signal). A good agreement between the training and testing sets is observed.*

5.6.2 Optimisation of the selection requirement

The requirement on the BDTG variable is optimised using a Figure of Merit (FoM):

$$\text{FoM} = \frac{S}{\sqrt{S+B}} \tag{5.7}$$

where S is the number of signal candidates, found by performing a fit to the $pK^-\pi^+$ mass spectrum where the number of signal events with a BDTG value higher than the requirement are extracted. The number of background events, B, is found by extrapolating the number of background events from the sidebands to the signal region. The optimal selection requirement was found to be BDTG>0.56, as shown in Fig. 5.7.

The $pK^-\pi^+$ invariant mass spectrum before (blue) and after (red) the BDTG requirement has been applied is shown in Fig 5.8. The purity of the signal in the sample, calculated as $S/S+B$, increases significantly to 93% after the BDTG requirement is applied.

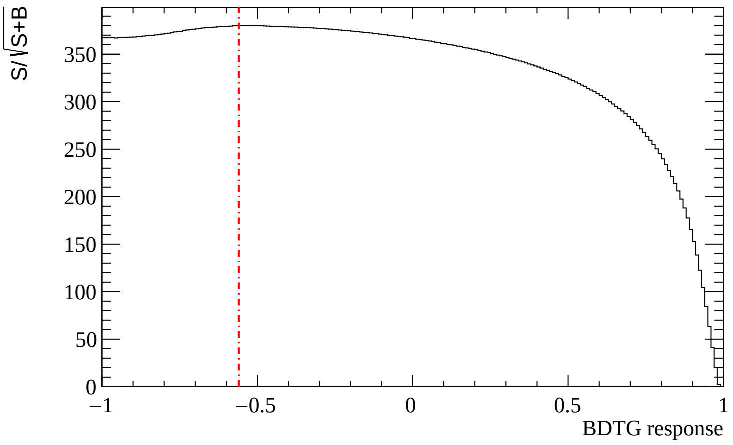

Figure 5.7 *The figure of merit, $S/\sqrt{S+B}$, shown as a function of the BDTG response. The red dashed line indicates the optimal selection requirement that was found.*

5.7 Background decay studies

This section describes the studies performed to understand the background decays that may contaminate the data sample. These decays can pollute the data for example when one or more of the daughter particles are misidentified, resulting in a final state with the same daughter particles as the decay being analysed. Furthermore, it is possible that decays with additional daughter particles are included when these additional particles are missing in the decay reconstruction. To ensure a good understanding of the mass spectrum studied in the analysis, we perform a cross-check by examining several possible sources of background resonances.

A comparison between the signal and background distributions for various particle hypotheses is made, where the background distribution is split into a low mass Λ_c^+ sideband (2230-2250 MeV) and a high mass Λ_c^+ sideband (2320-2340 MeV). The signal events are chosen as 20 MeV around the fitted Λ_c^+ mass, as found from the fit in Fig. 5.2.

The plots in Fig. 5.9 are made up of the following particle combinations:

(a) An $m(\pi^+K^+K^-)$ mass distribution of the three daughter particles of the Λ_c^+, where the proton has been misidentified as a positive kaon.

(b) An $m(\pi^+\pi^+K^-)$ mass distribution of the three daughter particles of the Λ_c^+,

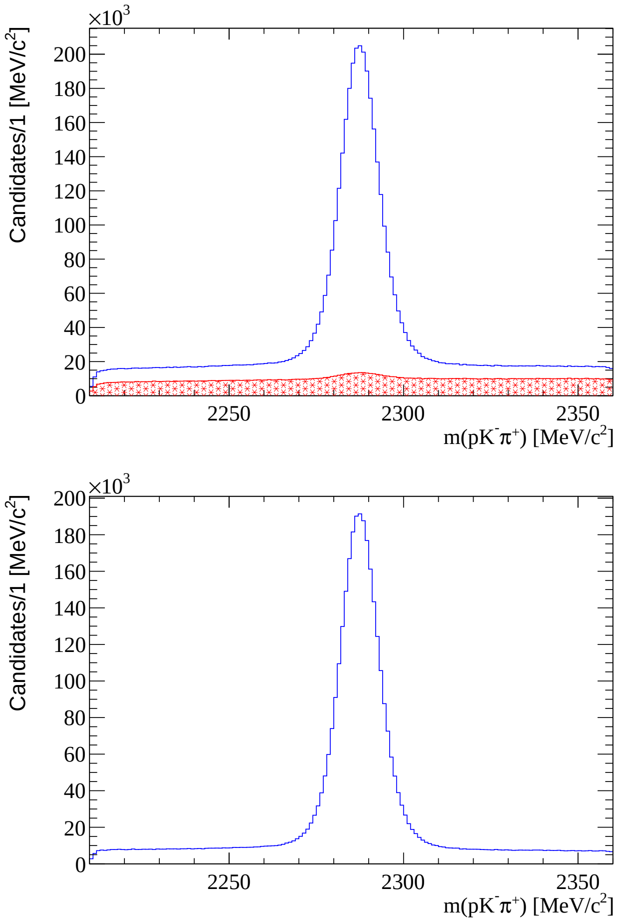

Figure 5.8 *The top figure shows the* $pK^-\pi^+$ *invariant mass distribution before the BDTG requirement in blue along with the event that will be removed by the BDT in red. The figure on the bottom shows the remaining events after the BDTG requirement. The 2016 data sample is used.*

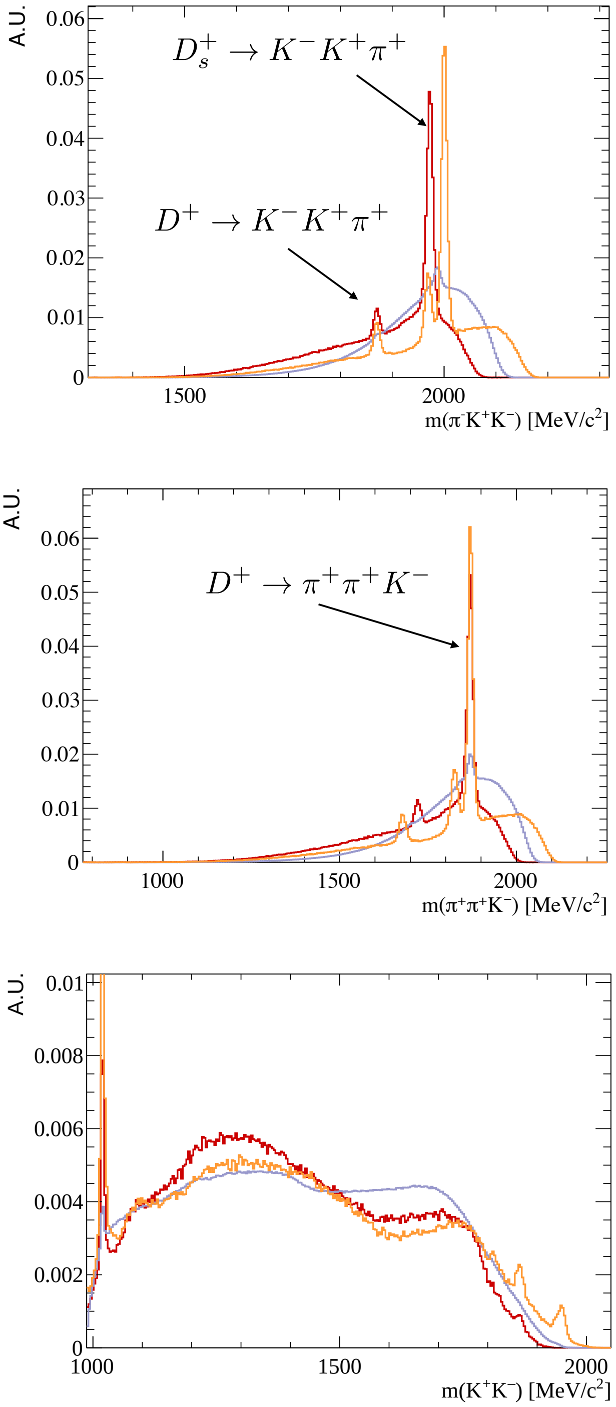

Figure 5.9 *Invariant mass distributions of the* $\pi^+K^+K^-$ *(top),* $\pi^+\pi^+K^-$ *(middle) and* K^+K^- *(bottom) mass hypotheses comparing* Λ_c^+ *signal region candidates to events in the* Λ_c^+ *sidebands. The lower sideband is given in red, the high mass sideband in orange and the signal distribution in grey.*

where the proton has been misidentified as a positive pion.

(c) A two kaon invariant mass distribution where kaon and proton daughter particles of the Λ_c^+ are taken, and the proton is misidentified as a kaon.

As can be seen in these plots, several sources of background contamination are present in the sample. Firstly, we observe three peaks in the background distribution when considering the $m(K^-K^+\pi^+)$ mass distribution, where the proton has been mis-identified as a kaon. The peaking structure around a mass of 1870 MeV corresponds to $D^+ \to K^-K^+\pi^+$ events. This decay has a branching fraction of $(9.93 \pm 0.24) \times 10^{-3}$ [6], indicating that roughly 1% of all D^+ decays to a $K^-K^+\pi^+$ final state. The second peak in the $m(K^-K^+\pi^+)$ invariant mass distribution, centred around 1970 MeV stems from $D_s^+ \to K^-K^+\pi^+$ contributions, which has a branching fraction of $(5.45 \pm 0.17)\%$, explaining the significantly larger contribution compared to the number of $D^+ \to K^-K^+\pi^+$ events. The third peak corresponds to $D^+ \to K^-\pi^+\pi^+$ events, which has a branching fraction of $(9.38 \pm 0.16)\%$. All three decays can be observed in both the $m(K^-K^+\pi^+)$ and $m(K^-\pi^+\pi^+)$ invariant mass distributions. Additionally, a clear contribution peaking around 1020 MeV of $\phi \to K^-K^+$ decays can be seen in the $m(K^+K^-)$ mass distribution.

In order to reduce the contributions to the background contamination in the data sample, a veto has been applied. The selection requirements applied are the proton's $\text{prob}_\pi < 0.25$, $\text{prob}_k < 0.5$, which are the probability that the proton is misidentified as a pion or a kaon, respectively. Furthermore, the $m(KK)$ mass, where the two kaons consist of the Λ_c^+ daughter kaon and Λ_c^+ daughter proton misidentified as a kaon, is required to be more than 10 MeV away from the known $\phi(1020)$ mass.

Fig. 5.10 shows the comparison between the signal and Λ_c^+ sideband distributions after the veto requirements have been applied. Although the background contamination is not fully removed by the requirements, tightening these was found to affect the signal efficiency drastically, such that the veto is optimised to 90% signal efficiency. The effect of these contaminations on the final fit parameters was checked, as described in Chapter 6.

Figure 5.11 shows the $m(pK^-\pi^+)$ invariant mass distribution before and after the veto, where the events removed by the veto are shown in red. Note that these plots are based on the full data-set, whereas the plots shown in Fig. 5.8 are

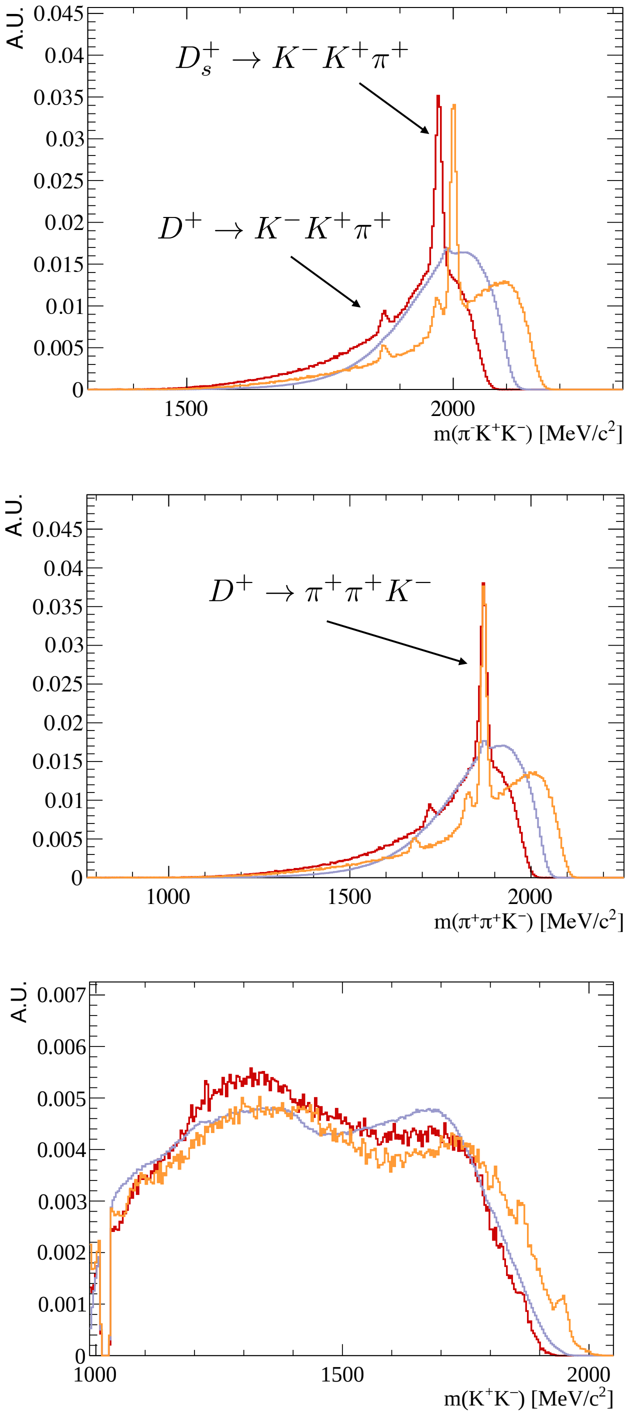

Figure 5.10 *Invariant mass distributions of the* $\pi^+K^+K^-$ *(top),* $\pi^+\pi^+K^-$ *(middle) and* K^+K^- *(bottom) mass hypotheses comparing* Λ_c^+ *signal region candidates to events in the* Λ_c^+ *sidebands, after the veto described in the text has been applied. The lower sideband is given in red, the high mass sideband in orange and the signal distribution in grey. The area underneath each curve is normalised to one.*

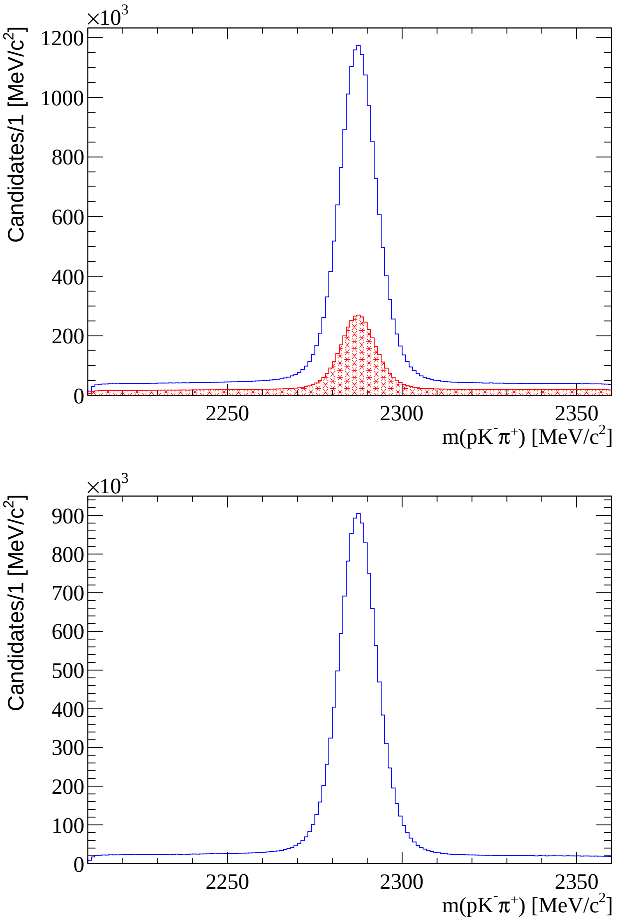

Figure 5.11 *The top figure shows the $pK^-\pi^+$ invariant mass distribution before the veto in blue along with the event that will be removed by the vetoes in red. The figure on the bottom shows the remaining events after the veto.*

based only on 2016 data. In addition, the BDT requirement has been applied in Fig. 5.11. Figure 5.11 shows that the veto removes some Λ_c^+ signal. The selection requirements are found to be 90% signal efficient, checked using simulated data samples (discussed in Chapter 6). Therefore the conclusion is made that the veto removes Λ_c^+ events that do not contribute to the excited Ξ_c^0 resonances found in this analysis.

5.8 Bachelor kaon selection

To further reduce the background, two variables are considered: the transverse momentum, p_{T}, of the $\Lambda_c^+K^-$ system and the particle identification information of the bachelor kaon, PID_K.

The Punzi FoM [56], given by

$$\frac{\epsilon_{MC}}{a/2+\sqrt{B}} \tag{5.8}$$

is used to optimise the selection requirement, where the signal efficiency, ϵ_{MC}, is extracted from the LHCb simulation sample. Several simulated samples have been produced in the decay chain $\Xi_c^{**}(X)^0 \to \Lambda_c^+(\to pK^-\pi^+)K^-$ (Tab. 5.1). Each of these could be used for this optimisation. We decided to choose the $\Xi_c(2939)^0 \to \Lambda_c^+K^-$ sample.

The desired level of significance, a, is chosen to be 5 since the analysis aims to observe new resonances. The Punzi FoM is typically used when trying to observe new particles or decays modes, as it does not depend on the number of signal candidates.

Finally, B is the number of background events in the signal region. The estimated number of background events in the signal region is extrapolated by considering a sideband in the $m(\Lambda_c^+K^-)$ spectrum. The width of this sideband corresponds to approximately $m(\Xi_c(2939)^0) \pm 3\sigma$, and is taken to be $3040\,\mathrm{MeV}/c^2 < m(\Lambda_c^+K^-) < 3070\,\mathrm{MeV}/c^2$. The background shape is assumed to be flat. This is an assumption which does not match the data perfectly. However, to first order the estimated number of background events should be accurate.

Performing an analysis where the decay products stem directly from the pp interaction point typically comes with a large number of background candidates. Hence, the optimal selection requirement is very tight. It was found that the highest possible signal purity could be achieved with a 2-dimensional optimisation using the Punzi FoM in the plane of the p_T of the $\Lambda_c^+K^-$ vs. the PID_K. Additional methods, such as optimising the selection individually for each variable and testing different FoM's were tried and yielded lower signal to background ratios.

Figure 5.12 shows the optimisation in terms of the p_T of the $\Lambda_c^+K^-$ and the PID_K of the bachelor kaon. For each point in the 2-dimensional plot, the Punzi figure of merit is calculated, assuming a selection requirement which keeps candidates with values larger than the value along both the X-axis and the Y-axis. The optimal selection is determined to be $\mathrm{PID}_k > 0.996$ and p_T $(\Lambda_c^+K^-) > 7350\,\mathrm{MeV}$, which is indicated by the black dashed lines in Fig. 5.12.

The 2-dimensional optimisation removes 95% of background while retaining 35% of the signal. This is an 18% relative signal increase with regards to the separate

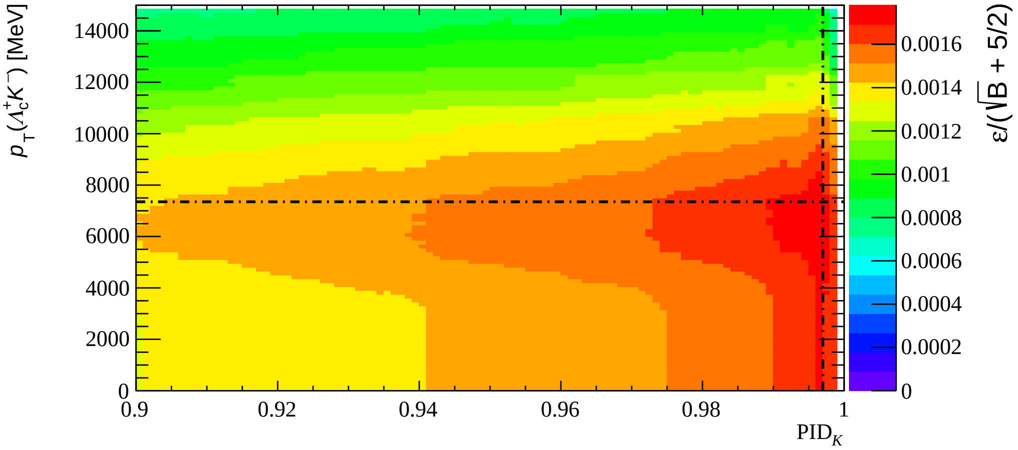

Figure 5.12 *The two-dimensional optimisation in terms of the p_{T} of the $\Lambda_c^+ K^-$ (y-axis) and the PID$_k$ of the bachelor kaon (x-axis). The z-axis shows the Punzi FoM calculated assuming a selection which keeps events with values larger than the value along the x-axis and the y-axis. The black dashed lines indicate the position where the optimal selection requirement is found.*

Table 5.5 *Selection requirements on the $\Lambda_c^+ K^\mp$ combinations.*

Particle	Requirement
Λ_c^+	$\lvert m(\Lambda_c^+) - 2286.46\rvert < 20\,\mathrm{MeV}$
$K^\mp$	$\chi^2_{IP} < 3$
$\Lambda_c^+ K^\mp$	$\chi^2\_DTF\_PV < 3$
$K^\mp$	$Prob_K > 0.996$
$\Lambda_c^+ K^\mp$	$p_{\mathrm{T}} > 7350$

1-dimensional optimisation. Whilst the signal efficiency is relatively low, a clear increase in the peak purity is observed.

A summary of the selection criteria on the $\Lambda_c^+ K^-$ candidates is shown in Tab. 5.5.

5.9 Clones and multiple candidates

When multiple tracks are reconstructed from one incident particle, it is referred to as a clone. This decay mode is susceptible to clones due to the inclusion of two K^- daughter particles, where one kaon track may be reconstructed twice to generate the bachelor kaon as well as the Λ_c^+ daughter kaon. This can artificially increase the amount of signal candidates, therefore these contributions should be removed. Clones are categorised in two types:

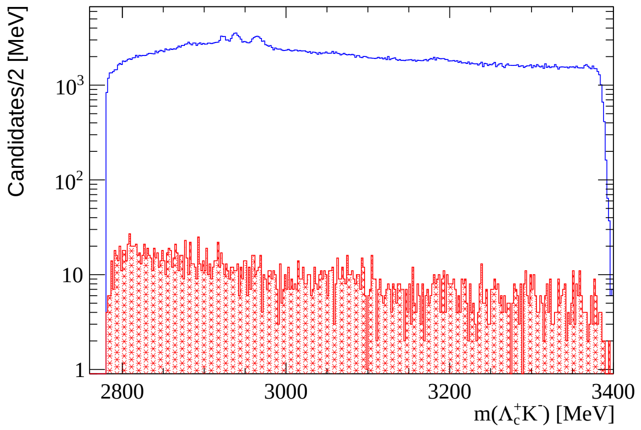

(a) *Type 1 clones*

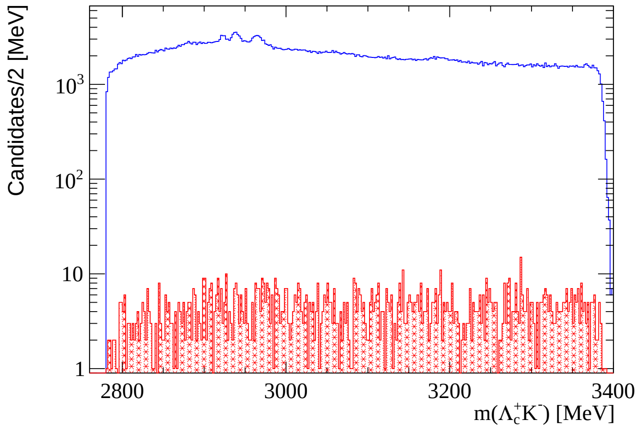

(b) *Type 2 clones*

Figure 5.13 *The distribution of type 1 (top) or type 2 (bottom) clones shown in red compared to the full mass spectrum (blue). Note the logarithmic y-scale.*

- **Type 1:** Multiply used VELO segments. These are rejected using tight requirements on Δtx and Δty, where $tx = px/pz$ and $ty = py/pz$ such that Δtx and Δty can be calculated as the difference between the tracks in consideration. The selection requirements applied are $\Delta tx < 0.0004$ and $\Delta ty < 0.0002$.
- **Type 2:** Long track clones. This type of clones is removed by requiring that $\Delta tx < 0.005$, $\Delta ty < 0.005$ and $\Delta q/p < 10^{-6}$.

Figure 5.13 shows the distribution of type 1 and type 2 clones (red) compared to the full mass spectrum (blue). Note that this plot has a logarithmic y-scale. The contamination of clones is very small in this analysis. The percentage of type 1 clones is 0.53%, and the percentage of type 2 clones is 0.24%. The total number of clones in the sample is 0.77%. The clones are removed from the rest of the analysis.

Furthermore, multiple candidates in the sample need to be dealt with. These occur when one Λ_c^+ baryon has multiple bachelor kaon tracks that could be associated with it. The number of multiple candidates in the ΔM mass difference range of $0 - 300\,\text{MeV}$ is calculated to be 0.88%, where ΔM is defined in Eq. 5.9. These events are kept in the analysis.

5.10 Summary

The selection described in this chapter leads to the mass difference ΔM spectrum shown in Fig. 5.14. The mass difference, ΔM, rather than $m(\Lambda_c^+ K^-)$ is used where ΔM is given by

$$\Delta M = m_{PV}(\Lambda_c^+ K^-) - m_{PV}(\Lambda_c^+) - m_{PDG}(K^-). \tag{5.9}$$

Here, $m_{PV}(\Lambda_c^+ K^-)$ is the invariant mass calculated after applying a PV constraint which requires the Λ_c^+ and the K^- to stem from the position of the associated PV. The associated PV is chosen as the PV with the lowest χ^2_{IP}.

The invariant mass spectrum starts at the kinematic threshold, and shows three clear narrow peaks. To the left of the peaks, a shoulder of additional candidates is observed. The fitting procedure for the obtained mass spectrum is described in detail in the next chapter.

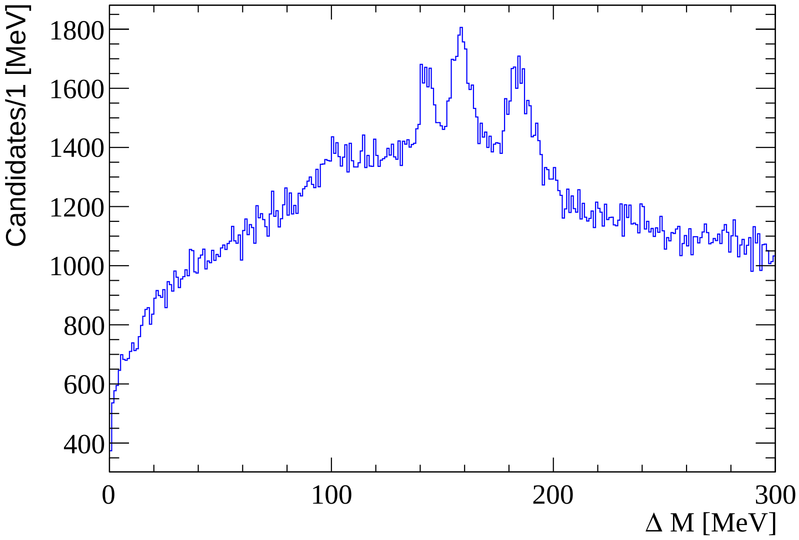

Figure 5.14 *The* ΔM *mass difference spectrum for* $\Lambda_c^+ K^-$ *candidates after all requirements, where* $\Delta M = m_{PV}(\Lambda_c^+ K^-) - m_{PV}(\Lambda_c^+) - m_{PDG}(K^-)$.

Chapter 6

Observation of excited Ξ_c^0 baryons

This chapter will focus on the observation of excited Ξ_c^0 baryons. In the previous chapter, the selection requirements necessary to choose the signal candidates have been discussed. Here we will first mention the simulated data sets required to extract the mass resolution of the states. Afterwards, several background decays are studied. The fit to the mass difference spectrum is explained, leading to the results. The chapter ends with a discussion of these results.

6.1 Mass resolution

The precision at which the detector is capable of measuring a particles mass is referred to as the mass resolution. This quantity needs to be determined, as it affects the measurement of the natural width of a particle. The mass resolution is found by performing a fit to the difference between the generated Ξ_c^{**0} mass and the reconstructed $\Lambda_c^+ K^-$ mass using a PV constraint. This variable is referred to as $\Delta M'$. The fits to $\Delta M'$, for each of the simulated $\Xi_c(X)^0 \to \Lambda_c^+ K^-$ samples described in Tab. 5.1 are shown in Fig. 6.1. In each of these fits, the probability density function (PDF) consists of a Gaussian function and a Crystal Ball function added together with a shared mean. The resolutions can be found in Tab. 6.1, listing the individual widths of the Gaussian function and the Crystal Ball function, σ_G and σ_{CB}, respectively, as well as their weighted mean, σ (Eq. 5.6). The parameters to account for the radiative tail in the Crystal Ball function are given by a_{CB} and n_{CB}, where n_{CB} is fixed to one in each case to

Table 6.1 *Parameters of the fits (Fig. 6.1) to extract the mass resolutions.*

Fit	mean [MeV]	σ_G [MeV]	σ_{CB} [MeV]	σ [MeV]	a_{CB}	n_{CB} (fixed)
(a)	-0.014 ± 0.013	0.39 ± 0.02	1.09 ± 0.12	0.57 ± 0.06	2.39 ± 0.20	1.0
(b)	0.026 ± 0.044	1.46 ± 0.05	3.64 ± 0.68	1.72 ± 0.06	1.81 ± 0.37	1.0
(c)	0.033 ± 0.046	1.48 ± 0.06	4.18 ± 0.47	1.95 ± 0.05	4.97 ± 3.63	1.0
(d)	0.066 ± 0.053	1.63 ± 0.06	4.63 ± 0.51	2.18 ± 0.05	3.27 ± 1.82	1.0
(e)	0.093 ± 0.072	2.21 ± 0.18	4.78 ± 1.17	2.55 ± 0.08	1.32 ± 0.59	1.0

ensure fit stability.

The weighted widths (Eq. 5.6), σ, are then plotted as a function of the ΔM mass, as shown in Fig 6.2. The mass resolution increases with the Q-value (ΔM), which implies that the detectors accuracy to perform mass measurements decreases as more energy is available. A fit is performed to the data points using the function

$$\sigma(\Delta M) = a \times (\Delta M)^b \tag{6.1}$$

where ΔM is given in Eq. 5.9.

The errors on the mass resolution are calculated by propagating the fit errors from the width of the Gaussian function and the width of the Crystal Ball function to the weighted mean. The fit parameters are $a = 0.19 \pm 0.03$ and $b = 0.45 \pm 0.03$. By definition, the fit runs through the origin of the graph.

6.2 Feed-down decays

Decays to $\Lambda_c^+ K^-$ with an additional pion in the final state constitute feed-down decays in this analysis and can produce structures in the ΔM invariant mass spectrum when the pion is missing in the reconstruction. Missing the pion in the reconstruction broadens the shape of the distribution. The probable feed-down decays to affect this analysis are generated using the RapidSim package [57]. RapidSim utilises the TGenPhaseSpace package from the ROOT application [58]. External theoretical fixed-order next-to leading-log calculations [59] are used as inputs to mimic the kinematics of the generated charm and beauty pairs in the production energies used at LHCb, allowing for fast phase space generation of decays with invariant mass resolutions, mass spectra and efficiencies similar to the full LHCb simulated data. The details for several of the feed-down

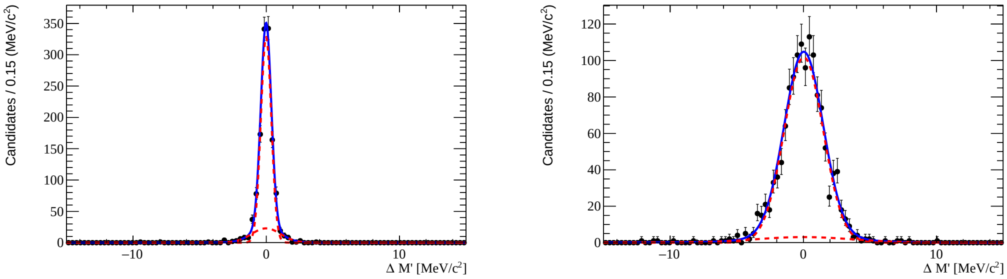

(a) $\Xi_c(2790)^0 \to \Lambda_c^+ K^-$

(b) $\Xi_c(2923)^0 \to \Lambda_c^+ K^-$

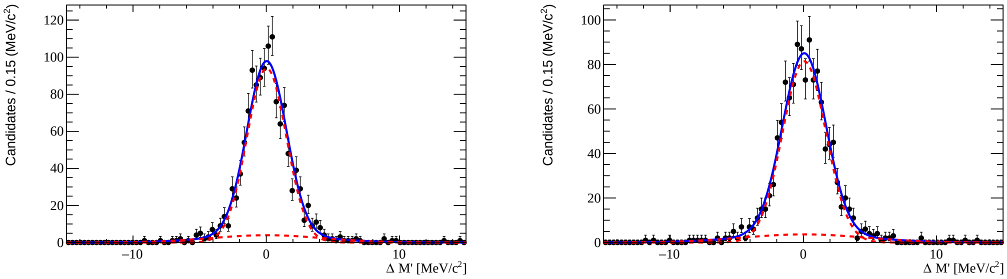

(c) $\Xi_c(2939)^0 \to \Lambda_c^+ K^-$

(d) $\Xi_c(2965)^0 \to \Lambda_c^+ K^-$

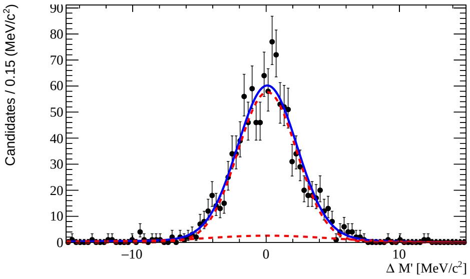

(e) $\Xi_c(3080)^0 \to \Lambda_c^+ K^-$

Figure 6.1 *Mass resolution distributions for different simulated $\Lambda_c^+ K^-$ samples, where the decay used is given below each plot. The observable on the x-axis is the difference between the generated Ξ_c^0 mass and the reconstructed $\Lambda_c^+ K^-$ mass. A fit consisting of two Gaussian functions is superimposed, where the separate Gaussian functions are given by the red dashed lines.*

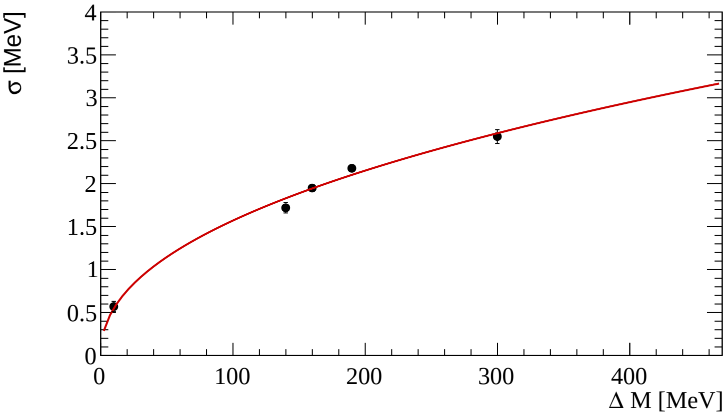

Figure 6.2 *Fit to the mass resolution width as a function of* ΔM*.*

Table 6.2 *Simulated samples using the RapidSim package, where 10000 events are generated for each sample and the collision energy used is 13 TeV.*

Description	Details
$\Xi_c(2965)^+ \to \Sigma_c(2455)^{++}(\to \Lambda_c^+\pi^+)K^-$	π^+invisible
$\Xi_c(3055)^+ \to \Sigma_c(2455)^{++}(\to \Lambda_c^+\pi^+)K^-$	π^+invisible
$\Xi_c(3055)^+ \to \Sigma_c^*(2520)^{++}(\to \Lambda_c^+\pi^+)K^-$	π^+invisible
$\Xi_c(3080)^+ \to \Sigma_c(2455)^{++}(\to \Lambda_c^+\pi^+)K^-$	π^+invisible
$\Xi_c(3080)^+ \to \Sigma_c^*(2520)^{++}(\to \Lambda_c^+\pi^+)K^-$	π^+invisible
$\Xi_c(3055)^0 \to \Sigma_c(2455)^{+}(\to \Lambda_c^+\pi^0)K^-$	π^0invisible
$\Xi_c(3080)^0 \to \Sigma_c(2455)^{+}(\to \Lambda_c^+\pi^0)K^-$	π^0invisible

samples are summarised in Tab. 6.2. These decays each have a Ξ_c^{**+} baryon decaying to a $\Sigma_c^{(*)++}$ baryon and a K^- meson, where the $\Sigma_c^{(*)++}$ baryon decays further into a Λ_c^+ baryon and a positive pion. In each sample, the decay has been partially reconstructed, where the pion is missing such that the $\Lambda_c^+K^-$ mass spectrum can be studied. All kinematically possible decays transitioning through any combination of $\Xi_c(3080)^+$, $\Xi_c(3055)^+$ and $\Xi_c(2965)^+$ combined with $\Sigma_c(2455)^{++}$ or $\Sigma_c^*(2520)^{++}$ are considered. In addition, the decay of the neutral $\Xi_c^{**0} \to \Sigma_c^+(\to \Lambda_c^+\pi^0)K^-$ is considered for two of the decays.

The invariant mass distributions of the first five entries in Tab. 6.2 are shown in Fig 6.3. For three of the samples, a full LHCb simulation sample was requested as these decays were initially found to contribute to the data sample[1]. For these decays, the mass distribution obtained from the LHCb simulation is superimposed

---

[1] It was later found that the $\Xi_c(3080)^+ \to \Sigma_c^*(2520)^{++}K^-$ feed-down decay is not necessary to describe the data.

Table 6.3 *Simulated samples using the RapidSim package, where 10000 events are generated for each sample and the collision energy used is 13 TeV.*

Description	Details
$\Xi_c(2923)^+ \to \Lambda_c^+\pi^+K^-$	π^+invisible
$\Xi_c(2939)^+ \to \Lambda_c^+\pi^+K^-$	π^+invisible
$\Xi_c(2923)^0 \to \Lambda_c^+\pi^0K^-$	π^0invisible
$\Xi_c(2939)^0 \to \Lambda_c^+\pi^0K^-$	π^0invisible

in green. A good agreement between the RapidSim samples and the MC samples is observed. A small discrepancy is seen in Fig 6.3(e), which is due to the fact that not all selection requirements can be applied in RapidSim, since it is a simplified simulation.

Any excited state with mass $m(\Lambda_c^+) + m(K) + m(\pi) < m(\Xi_c(X)) < m(\Sigma_c) + m(K)$ could still decay to the $\Lambda_c^+\pi^+K^-$ (or $\Lambda_c^+\pi^0K^-$) final state according to the phase space. If the π^+ (or π^0) is missed in the reconstruction, these decays will contribute to our data sample at around the $m(\Lambda_c^+) + m(K^-)$ threshold. Usually such feed-downs are quite broad, except when the mass is close to the kinematic threshold (i.e. $m(\Xi_c^{**}) \sim m(\Lambda_c^+) + m(K) + m(\pi)$). The signal peaks observed in the $m(\Lambda_c^+K^-)$ mass spectrum have masses which fit this scenario. Therefore simulated samples are generated using RapidSim[2] (Tab. 6.3) to probe the presence of these feed-downs. Since the excited Ξ_c resonances are new discoveries, the mass and width of these particles are set to the values obtained from a preliminary fit to the data set.

6.3 Fit to the mass spectrum

The invariant mass $\Delta M = m_{PV}(\Lambda_c^+K^-) - m_{PV}(\Lambda_c^+) - m_{PDG}(K^-)$ spectrum, after all the selection criteria are applied, is shown in Fig. 6.4. Three peaks are visible above the combinatorial background. A fit will be performed to ΔM mass difference distribution, which is defined in Eq. 5.9.

---

[2] The generation of such samples using the official LHCb simulation would be time consuming given the smallness of the phase space of the decays. However Fig. 6.3 shows that RapidSim accurately describes the distributions.

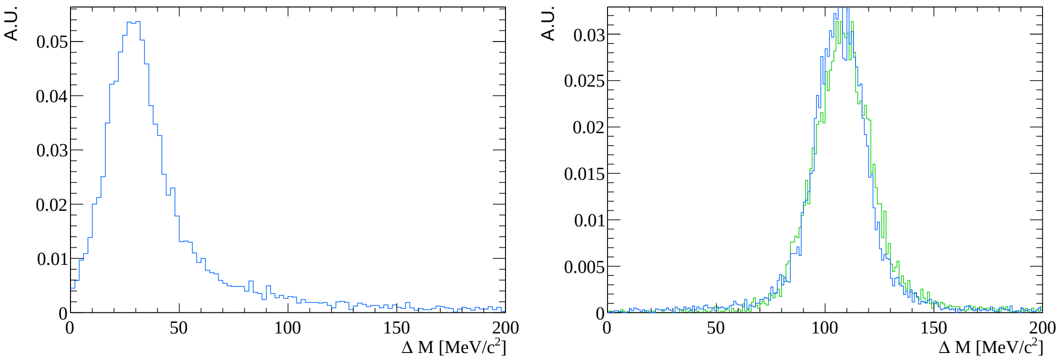

(a) $\Xi_c(2965)^+ \to \Sigma_c(2455)^{++}K^-$ **(b)** $\Xi_c(3055)^+ \to \Sigma_c(2455)^{++}K^-$

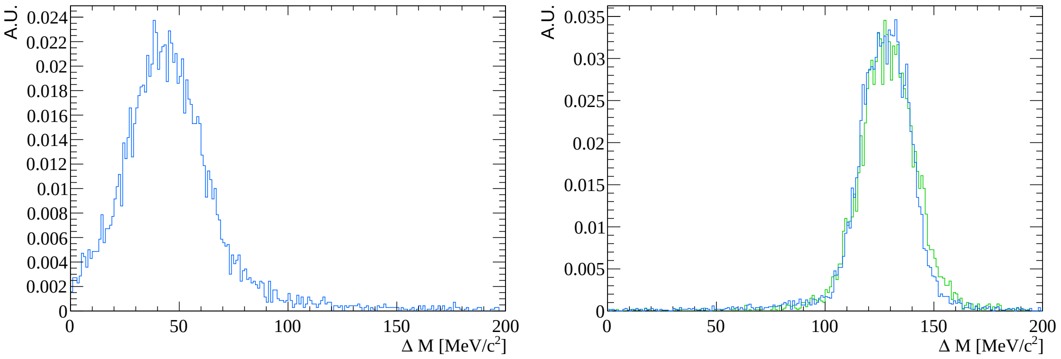

(c) $\Xi_c(3055)^+ \to \Sigma_c^*(2520)^{++}K^-$ **(d)** $\Xi_c(3080)^+ \to \Sigma_c(2455)^{++}K^-$

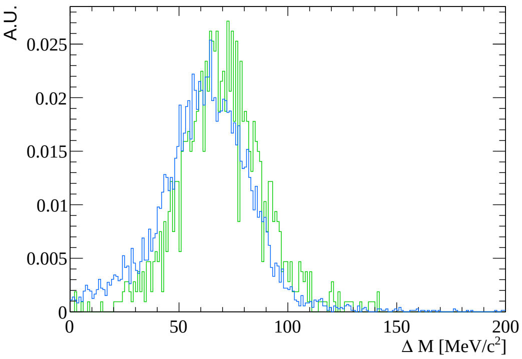

(e) $\Xi_c(3080)^+ \to \Sigma_c^*(2520)^{++}K^-$

Figure 6.3 *Invariant mass distributions for the simulated data samples using the RapidSim package, as a function of ΔM, plotted in blue, where $\Delta M = m_{PV}(\Lambda_c^+ K^-) - m_{PV}(\Lambda_c^+) - m_{PDG}(K^-)$. In each simulated sample, $\Sigma_c(2455)^{++} \to \Lambda_c^+\pi^+$ and $\Sigma_c(2520)^{++} \to \Lambda_c^+\pi^+$. Wherever available, the full LHCb simulation has been superimposed in green.*

6.3.1 Signal shape

The Ξ_c^{**0} signal resonances are parameterised using a relativistic Breit-Wigner (BW) function with angular momentum of L = 0, convoluted with a Gaussian function representing the mass resolution, as studied in Sec. 6.1. The BW function for a resonance of mass M is given as a function of the measured mass m by

$$BW(m) = \frac{q\left(\frac{q}{q_0}\right)^{2L} B'_L(q,q_0)^2}{\left(m^2 - M^2\right)^2 + M^2\Gamma^2(m)}, \tag{6.2}$$

where the BW width is defined as

$$\Gamma(m) = \Gamma\frac{M}{m}\left(\frac{q}{q_0}\right)^{2L+1} B'_L(q,q_0)^2, \tag{6.3}$$

and

$$q = \frac{1}{2m}\sqrt{\left[m^2 - \left(m_{\Lambda_c} + m_K\right)^2\right]\left[m^2 - \left(m_{\Lambda_c} - m_K\right)^2\right]} \tag{6.4}$$

is the definition of the centre-of-mass momentum. The Blatt-Weisskopf barrier factors, $B'_L(q,q_0)^2$, are shown in Tab. 6.4, where $z = (|q|d)^2$ and $z_0 = (|q_0|d)^2$ and d is the radius of the particle.

Table 6.4 *Blatt-Weisskopf barrier factors where* $z = (|q|d)^2$ *and* $z_0 = (|q_0|d)^2$ *[6].*

L	$B_L(q)$	$B'_L(q,q_0)^2$
0	1	1
1	$\sqrt{\frac{2z}{1+z}}$	$\sqrt{\frac{1+z_0}{1+z}}$
2	$\sqrt{\frac{13z^2}{(z-3)^2+9z}}$	$\sqrt{\frac{(z_0-3)^2+9z_0}{(z-3)^2+9z}}$

6.3.2 Background parameterisation

A good understanding of the combinatorial background shape is important as it is necessary to model it in the data sample. Three different methods are considered to describe the background.

- Firstly, the invariant mass distribution of wrong sign (WS) $\Lambda_c^+K^+$ combinations is studied. Since the quark content of such combinations is $cudu\overline{s}$, no conventional baryons are expected in the spectrum and therefore no peaking resonances should be seen. As can be seen in Fig. 6.4 in the orange distribution, the WS model does not follow the expected background shape. This could potentially be explained by the fact that many (broad) states and feed-down decays are expected in this mass region. Similar behaviour (often referred to as "associated production") has been observed in other analyses as well [60, 61]. It would be interesting to see whether this trend is also observed in simulated data sets but currently such samples are not available.

- Secondly, the data in the sidebands of the Λ_c^+ invariant mass spectrum are considered as a model for the combinatorial background. It is shown in red in Fig. 6.4. This method yields a better agreement with the observed combinatorial background shape. However, at low values for ΔM the background model overshoots the signal distribution. A cross check was performed to check that this overshoot can not be explained by the D meson background decays described in Sec. 5.7, as described in App. A.
- Since none of the conventional methods described above yield the desired result, a third method was tested. The Λ_c^+ candidate of each event was combined with the bachelor kaon candidates of the next event to create a $\Lambda_c^+ K^-$ mass distribution. Since the particles stem from different events, no resonant structures are expected. The invariant mass distribution found using this method mimics the WS decay distribution outlined above, as indicated by the green distribution in Fig. 6.4. This distribution is lower in statistics since it is only based on 2016 MD data.

The distributions of all three background methods are normalised to the signal data in the mass region from 500-600 MeV/c.

Many different models have been tried to describe the background:

1. The invariant mass distribution obtained from the $m(\Lambda_c^+)$ sideband, where the distribution has been fitted and the shape is fixed. This background model does not give a good fit result.
2. An addition of the $m(\Lambda_c^+)$ sideband shape and the WS background shape, where both shapes are fixed and the number of $m(\Lambda_c^+)$ sideband is fixed to the expected number of background events in the $m(\Lambda_c^+)$ signal region (Fig. 6.5). Again, this method does not yield a good fit result. Note also the lack of sideband candidates.

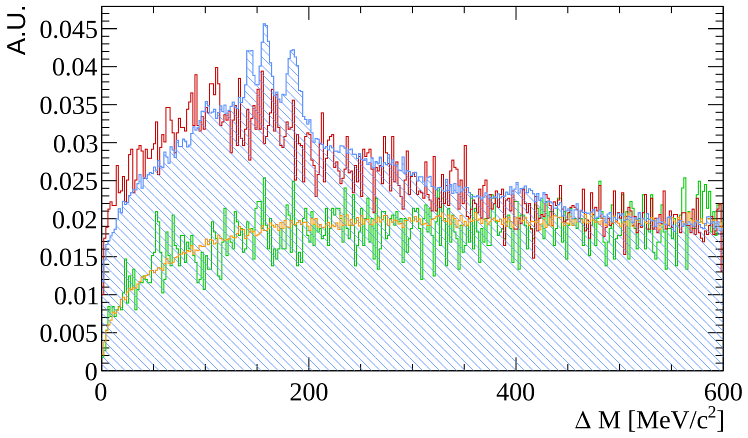

Figure 6.4 *The ΔM invariant mass distribution is shown for (i) signal $\Lambda_c^+ K^-$ candidates (shaded blue), (ii) WS $\Lambda_c^+ K^+$ candidates (orange), (iii) candidates in the Λ_c^+ sidebands (red) and (iv) event mixing where the Λ_c^+ candidate of each event was combined with the bachelor kaon candidates of the next event (green). The distributions are normalised in the mass region from 500-600* MeV*.*

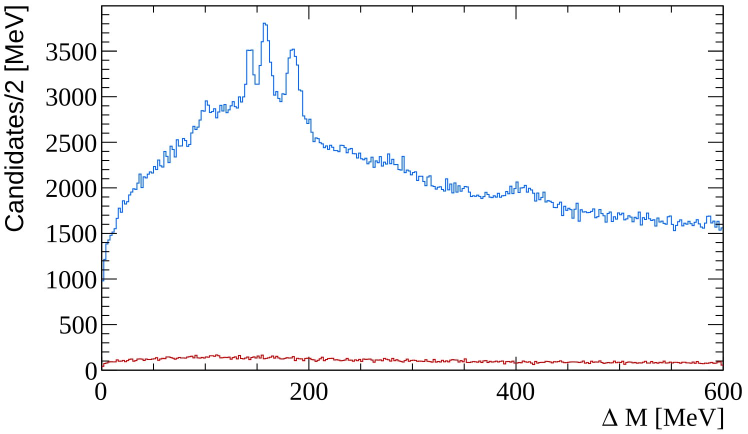

Figure 6.5 *The ΔM invariant mass distribution is shown for the signal candidates and the events in the Λ_c^+ sideband to illustrate the lack of candidates in the sideband.*

3. A combination of the sideband background model shape and the WS background shape, where the shapes are fixed but the fraction between the shapes is left floating was tested. This method yields a good fit result, but the fraction between the two shapes cannot be explained which is why it was not chosen as the nominal fit model. However, this background parameterisation has been included as a systematic uncertainty (Sec. 6.4).
4. Finally, an empirical function of the form $\text{PDF}_{\text{BG}} = (\Delta M)^a \times \exp(-b \times \Delta M)$, where all parameters are free in the fit. This method yields a good result, which is chosen as the nominal fit.

6.3.3 Feed-down fits

In initial fits to the data, all feed-down decays discussed in Sec. 6.2 are allowed to contribute. It was noted that the only feed-down components necessary to describe the data are the $\Xi_c(3080/3055)^0 \to \Sigma_c(2455)^+ K^-$, as well as the $\Xi_c(3080/3055)^+ \to \Sigma_c(2455)^{++} K^-$ components, where the $\Sigma_c(2455)^+$ decays to $\Lambda_c^+ \pi^0$ and the $\Sigma_c(2455)^{++}$ decays to $\Lambda_c^+ \pi^+$. It is possible for the feed-down decays to have an angular dependence due to the spin configurations of the particles involved. This may change the shape of the invariant mass distribution of the feed-down components. This effect has been investigated by M. Mikhasenko using the formalism he developed [62]. There is no angular dependence for the decays included in the fit to the data.

In the fit, the feed-down components have a shape fixed to the MC samples but their yields are left free. The shapes are extracted using the fits shown in Fig. 6.6 by fixing all fit parameters. The $\Xi_c(3080/3055)^0 \to \Sigma_c(2455)^+ K^-$ fit consists of the addition of two Gaussian functions with a shared mean, and the $\Xi_c(3080/3055)^0 \to \Sigma_c(2455)^+ K^-$ fit consists of the addition of three Gaussian functions with separate means and widths.

In addition, each entire feed-down shape is allowed to shift by the uncertainties in the decay masses. These shifts are implemented in the fit as Gaussian constraints.

The feed-down decays of the neutral Ξ_c^0 baryons needs to be taken into consideration as well. However, there is no full LHCb simulation available for the $\Xi_c(3080/3055)^0 \to \Sigma_c(2455)^+ K^-$ components. Generating these events would be very time consuming. Therefore this contribution is assumed to have the same shape as that of the relative $\Xi_c(3080/3055)^+ \to \Sigma_c(2455)^{++} K^-$ component.

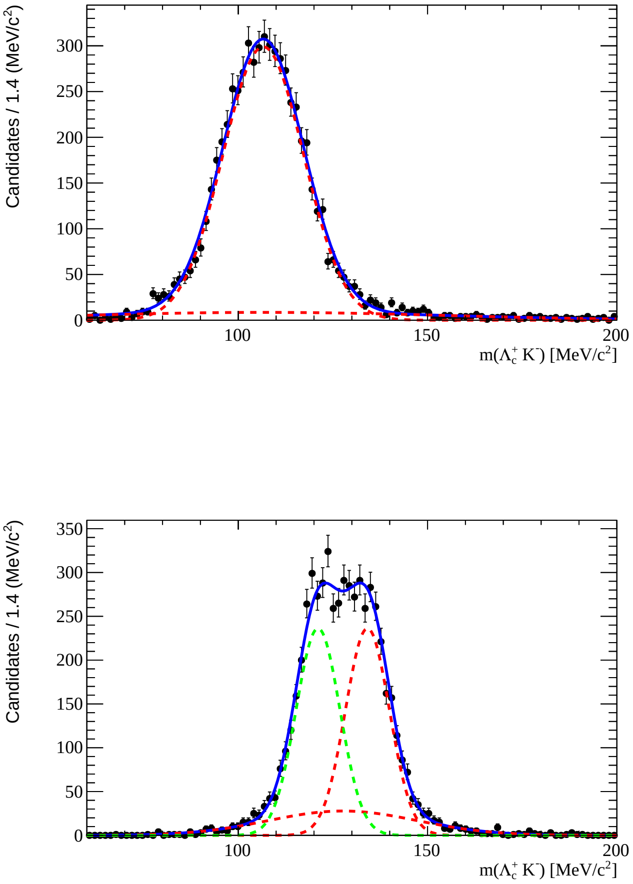

Figure 6.6 *Shown are the* ΔM *invariant mass distributions from feed-down of* $\Xi_c(3080/3055)^+ \to \Sigma_c(2455)^{++}K^-$ *decays, where the* $\Xi_c(3055)^+$ *is on the top and the* $\Xi_c(3080)^+$ *decay on the bottom. The data points are given in black, and a fit to the data is superimposed.*

Furthermore, the yield of the neutral Ξ_c^0 baryons decays are constrained to be half of their π^+ counterpart, as calculated using the Clebsch-Gordan coefficients [6], described in more detail in Appendix B.

Finally, the feed-down components of the $\Xi_c^{**+} \to \Lambda_c^+ K^- \pi^+$ and $\Xi_c^{**0} \to \Lambda_c^+ K^- \pi^0$ decays are generated using RapidSim, where the pion is missing in the reconstruction. These feed-down components fall just above the $\Lambda_c^+ K^-$ mass threshold. The shape of the component is taken from the RapidSim samples (Tab. 6.3), where a histogram of the entries is imported into the fit model. Due to their proximity to the kinematic threshold, these feed-down shapes are not allowed to shift. The only components found to contribute to the fit significantly is the $\Xi_c(2923)^+ \to \Lambda_c^+ K^- \pi^+$. The feed-down components in the fit are summarised in Tab. 6.5.

Table 6.5 *The feed-down components contribution to the fit*

Decay	How is the shape obtained?
$\Xi_c(3080)^+ \to \Sigma_c(2455)^{++} K^-$	LHCb simulation
$\Xi_c(3080)^0 \to \Sigma_c(2455)^+ K^-$	Equal to the charged decay
$\Xi_c(3055)^+ \to \Sigma_c(2455)^{++} K^-$	LHCb simulation
$\Xi_c(3055)^0 \to \Sigma_c(2455)^+ K^-$	Equal to the charged decay
$\Xi_c(2923)^+ \to \Lambda_c^+ K^- \pi^+$	RapiSim simulation

6.3.4 The fit

An unbinned maximum likelihood fit to the data, with three BW signal functions and all the background components described previously, is performed (Fig. 6.7). Above the fit, the pull distribution of the fit compared to the data points is given, showing a good agreement. The fit consists of the signal components, given by the red, brown and magenta dashed lines. The feed-down components are displayed in blue ($\Xi_c(3080) \to \Sigma_c K$) and green ($\Xi_c(3055) \to \Sigma_c K$) and the red shaded component is the $\Xi_c(2923)^+ \to \Lambda_c^+ K^- \pi^+$ where the pion is missing in reconstruction. The combinatorial background is given by the black dashed line. The total fit is shown by the solid blue line. The bottom part of the figure shows a background subtracted version of the data. Three resonances are observed, and the significance of these signal peaks exceeds 5σ largely in every case. Their measured masses and widths with statistical errors are given in Tab. 6.6.

In addition to the unbinned maximum likelihood fit, a binned maximum likelihood fit is performed, where the bin width is 1 MeV. The fit parameters are in

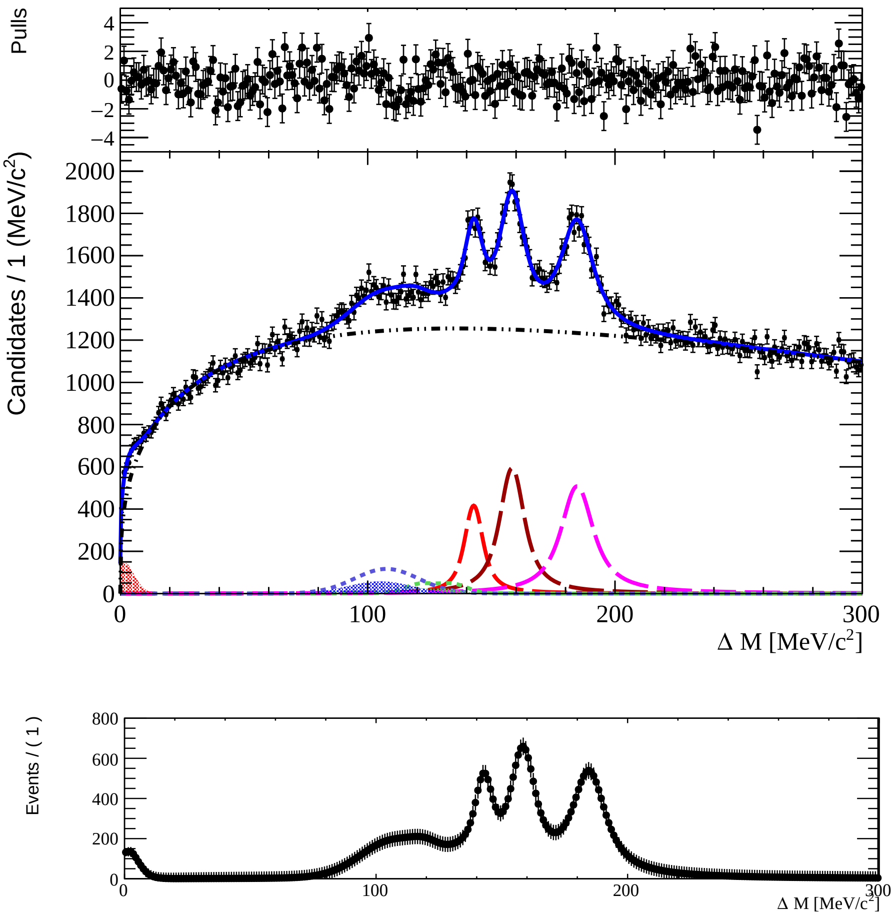

Figure 6.7 *The plot shows the invariant mass difference, ΔM for selected $\Lambda_c^+ K^-$ candidates. A fit, described in the text, is overlaid. The pull distribution is shown at the top. The bottom figure shows the background subtracted distribution.*

Table 6.6 *List of the main parameter results for the fit to the data shown in Fig. 6.7.*

Parameter	Fit value
mean$_1$	142.91 ± 0.25 MeV/c^2
mean$_2$	158.45 ± 0.21 MeV/c^2
mean$_3$	184.75 ± 0.26 MeV/c^2
Γ_1	7.09 ± 0.79 MeV/c^2
Γ_2	10.22 ± 0.77 MeV/c^2
Γ_3	14.07 ± 0.91 MeV/c^2
N(sig1)	5381 ± 425
N(sig2)	10424 ± 552
N(sig3)	11677 ± 552
$\chi^2/NDOF$	1.06478

agreement between the two fits. To further test the stability of the fit parameters, several cross-checks are performed using binned maximum likelihood fits. These include fits where the data are split up according to data taking year, according to magnet polarity and according to the charge of the daughter particles($\Lambda_c^+ K^-$ vs. $\bar{\Lambda}_c^- K^+$). Finally, fits are performed where the selection requirements on the bachelor kaon (Sec. 5.8) are loosened, and the background decays discussed in Sec. 5.7 are removed fully. A good agreement between all fits is found.

6.4 Systematic uncertainties

The main results are the masses and widths of the newly discovered resonances. Here, several sources of systematic uncertainties are investigated. A summary of the systematic uncertainties is given in Tab 6.11 at the end of this section. The total systematic errors are calculated as a sum in quadrature of the separate contributions.

6.4.1 Fit model

Several alternative fit models, detailed in this section, are used to describe the data. The uncertainties on both the mass and the width found by varying the fit model are summarised in Tab. 6.8.Here we discuss the different contributions.

- **Background model:** the PDF used to describe the combinatorial background is changed from an empirical function to the addition of the shape obtained from candidates in the WS data set and the shape from events in the Λ_c^+ sidebands (see Fig. 6.4). The shapes are fixed using the parameters obtained in the fits shown in Fig. 6.8. The fit parameters are listed in Tab. 6.7, where the fit model is described by a threshold function of the shape

  $$\mathrm{PDF} = (\Delta M)^a \times \exp(-b \times \Delta M), \tag{6.5}$$

  where a is the power and b is the slope. The fraction between the shapes is left as a free parameter in the fit. The difference in mass and width measurements between the nominal background model and the model described here is listed in Tab. 6.8.

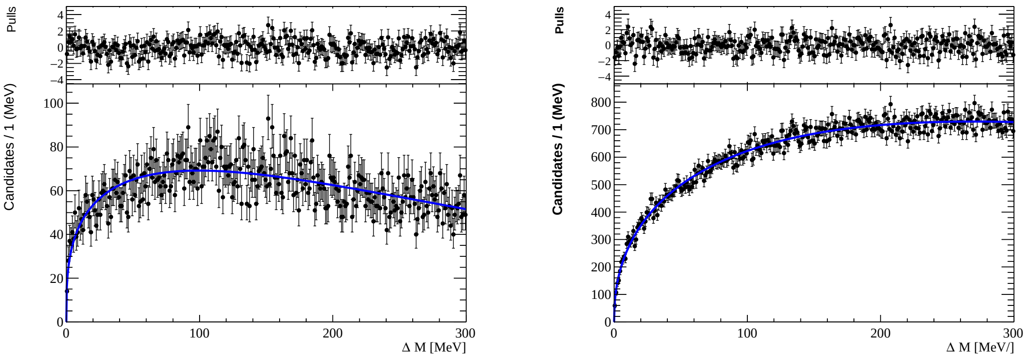

Figure 6.8 *A fit to the combinatorial background mass spectrum, where the events are taken from (left) the Λ_c^+ sidebands, and (right) the WS distribution.*

Table 6.7 *Fit parameters of the fits to the combinatorial background shapes shown in Fig. 6.8.*

BG model	a (power)	b (slope)[MeV^{-1}]	$\chi^2/NDOF$
$m(\Lambda_c^+)$ sideband	0.322 ± 0.019	$(3.238 \pm 0.200) \times 10^{-3}$	0.993117
WS	0.437 ± 0.007	$(1.619 \pm 0.070) \times 10^{-3}$	0.934705

- For each resonance, the **Breit-Wigner function** is changed. An angular momentum of $L = 1$ or $L = 2$ is introduced. In addition, the Blatt-Weisskopf radius r is varied between 2, 3 and 4 GeV $^{-1}$. This yields a total of 6 different fits, listed in Tab. 6.8.

- Finally, the fit model is adapted to include the **feed-down components** discussed in Sec. 6.2 that were found to not contribute to the fit significantly. The first component added is the decay $\Xi_c(2965)^+ \rightarrow \Sigma_c^{++}K^-$. Next, the $\Xi_c(3055) \rightarrow \Sigma_c^* K$ decay was added, where both the neutral and charged component are considered. The ratio between the charged and neutral component is fixed, determined by the expected ratio between the decays calculated using Clebsch-Gordan coefficients. The same procedure is performed for the neutral and charged $\Xi_c(3080) \rightarrow \Sigma_c^* K$ decays. No significant contributions to the fit model systematic error are found from the feed-down components.

- Due to the discrepancy between the data and the fit around $\Delta M = 100$ MeV, a systematic uncertainty studied by adding a fourth component.

The largest of the systematic errors is highlighted in red and is quoted as the systematic uncertainty due to the fit model.

Table 6.8 *Summary of the systematic uncertainties obtained by varying the fit model.*

Source	$\Xi_c(2923)^0$		$\Xi_c(2939)^0$		$\Xi_c(2965)^0$	
	m[MeV]	Γ[MeV]	m[MeV]	Γ[MeV]	m[MeV]	Γ[MeV]
Alternative bkg model	-0.01	0.08	0.01	0.16	0.01	0.10
BW $L = 1$, $r = 2$ GeV^{-1}	-0.01	-0.04	-0.04	-0.11	-0.03	0.27
BW $L = 1$, $r = 3$ GeV^{-1}	-0.01	0.34	0.00	-0.20	-0.02	0.29
BW $L = 1$, $r = 4$ GeV^{-1}	0.00	0.12	0.00	-0.11	-0.01	0.17
BW $L = 2$, $r = 2$ GeV^{-1}	-0.09	-0.45	-0.14	-0.09	-0.04	0.74
BW $L = 2$, $r = 3$ GeV^{-1}	-0.07	-0.35	-0.12	-0.09	-0.04	0.64
BW $L = 2$, $r = 4$ GeV^{-1}	-0.05	-0.65	-0.11	0.01	-0.04	0.46
Feed-down without fit	-0.15	1.05	0.06	-0.09	-0.01	0.16
Feed-down $\Xi_c^{**}(2970) \to \Sigma_c K$	0.00	0.21	0.02	-0.03	0.00	-0.03
Feed-down $\Xi_c^{**}(3055) \to \Sigma_c^* K$	-0.01	-0.62	-0.04	0.23	0.02	-0.14
Feed-down $\Xi_c^{**}(3080) \to \Sigma_c^* K$	-0.01	0.63	0.02	0.34	0.03	1.09
Fourth peak	0.17	1.59	0.13	0.44	0.03	0.10
Largest error	0.17	1.59	-0.14	0.44	-0.04	1.09

Table 6.9 *Contributions to the systematic uncertainty from interference effects between the resonances.*

Source	$\Xi_c(2923)^0$		$\Xi_c(2939)^0$		$\Xi_c(2965)^0$	
	m[MeV]	Γ[MeV]	m[MeV]	Γ[MeV]	m[MeV]	Γ[MeV]
$\Xi_c(2923)^0$-$\Xi_c(2939)^0$	-0.01	0.48	0.06	-0.33	-0.01	0.02
$\Xi_c(2939)^0$-$\Xi_c(2965)^0$	0.08	0.72	0.04	-0.95	-0.11	0.74

6.4.2 Resonance interferences

An interference effect is introduced between two signal resonances, of the form

$$A = a_1|BW_1 + c \times e^{i\phi} BW_2|^2, \tag{6.6}$$

where BW_1 and BW_2 are two complex Breit-Wigner functions and c and ϕ are free parameters in the fit. This systematic uncertainty is necessary as two resonances with equal quantum numbers can interfere. As the quantum numbers of these new states are unknown, this possibility needs to be accounted for. The combination of Breit-Wigner functions will be convoluted with a Gaussian function to model the detector resolution, where the detector resolution used is taken as the average between the resolution of the two individual signals.

The interference effect is introduced between neighbouring signal resonances, such that two separate tests are performed: $\Xi_c(2923)^0$ versus $\Xi_c(2939)^0$ and $\Xi_c(2939)^0$ versus $\Xi_c(2965)^0$. Table 6.9 summarises the results, where a systematic error is given for both the mass and the width measurements.

Table 6.10 *Variances in the width fit parameter of the resonances as an effect of varying the MC mass resolution, in* MeV *and* %.

Source	$\Xi_c(2923)^0$	$\Xi_c(2939)^0$	$\Xi_c(2965)^0$
0.9 × resolution	+0.57 MeV	+0.25 MeV	+0.19 MeV
1.1 × resolution	-0.20 MeV	-0.24 MeV	-0.26 MeV

6.4.3 Momentum scaling uncertainty

A systematic error of 0.03% on the resonance Q-value is employed to account for the mass scale calibration. The track momenta are re-calibrated offline. It was found that b-hadron masses agree with their known values within 0.03% after calibration [63]. Since this uncertainty only affects the mass measurements, no systematic error is applied for the width measurements.

6.4.4 Energy loss

The imperfect modelling of the energy loss in the detector material results in errors in the reconstruction. In previous LHCb analyses, the magnitude of this uncertainty was found to be 0.04 MeV on the mass measurements [51].

6.4.5 Mass resolution

It is known that the simulated data may not replicate the absolute resolution of the LHCb detector perfectly. A systematic error is introduced to account for the variations in the width measurements. The resolution obtained from simulation, as described in Sec. 6.1, is varied by 10%, providing a very conservative measure of any disagreement. This variation is based on previous studies of $D^{*+} \to D^0\pi^+$ decays [64]. The results are shown in Tab. 6.10.

6.4.6 $\mathit{\Lambda}_c^+$ mass uncertainty

Since the fit performed results in a measurement of ΔM, the mass fit parameter need to be converted in a $m(\mathit{\Lambda}_c^+ K^-)$ mass measurements by adding the masses of the $\mathit{\Lambda}_c^+$ and K^- [6]. The uncertainty on the $\mathit{\Lambda}_c^+$ mass measurements as reported by the PDG [6] is cited as a systematic uncertainty. The kaon mass uncertainty

Table 6.11 *Summary of the contributions to the systematic errors on the resonance parameters, where in every case the absolute deviation from the nominal fit is quoted.*

Source	$\Xi_c(2923)^0$		$\Xi_c(2939)^0$		$\Xi_c(2965)^0$	
	m[MeV]	Γ[MeV]	m[MeV]	Γ[MeV]	m[MeV]	Γ[MeV]
Alternative fit model	0.15	1.6	0.14	0.4	0.04	1.1
Resonance interferences	0.08	0.7	0.06	1.0	0.11	0.7
Momentum scaling uncertainty	0.04	–	0.05	–	0.06	–
Energy losses	0.04	–	0.04	–	0.04	–
Data-MC discrepancy	–	0.6	–	0.2	–	0.3
Total	0.20	1.8	0.17	1.1	0.14	1.3

does not need to be taken into account, as the known kaon mass is subtracted to achieve the ΔM variable. The precision of 0.14 MeV on $m(Lc)$ is taken as a systematic uncertainty for each mass measurement.

6.4.7 Summary of systematic errors

The results of the studies on systematic uncertainties are summarised in Tab. 6.11. The results are added in quadrature to calculate the overall systematic uncertainty on the mass and width measurements. The Λ_c^+ mass uncertainty is added separately.

6.5 Results

The $\Lambda_c^+ K^-$ mass spectrum is investigated using $5.57\,\text{fb}^{-1}$ (2016+2017+2018) of data of pp collisions collected by the LHCb detector at center-of-mass energy $\sqrt{s} = 13$ TeV. Three new excited Ξ_c^{**0} states are observed with the following mass difference and natural width parameters:

$$\Delta M(\Xi_c(2923)^0) = 142.91 \pm 0.25\,(\text{stat}) \pm 0.20\,(\text{syst})\ \text{MeV},$$
$$\Gamma(\Xi_c(2923)^0) = 7.09 \pm 0.79\,(\text{stat}) \pm 1.84\,(\text{syst})\ \text{MeV},$$

$$\Delta M(\Xi_c(2939)^0) = 158.45 \pm 0.21\,(\text{stat}) \pm 0.17\,(\text{syst})\ \text{MeV},$$
$$\Gamma(\Xi_c(2939)^0) = 10.22 \pm 0.77\,(\text{stat}) \pm 1.07\,(\text{syst})\ \text{MeV},$$

$$\begin{aligned}\Delta M(\Xi_c(2965)^0) &= 184.75 \pm 0.26\,(\text{stat}) \pm 0.14\,(\text{syst})\ \text{MeV},\\ \Gamma(\Xi_c(2965)^0) &= 14.07 \pm 0.91\,(\text{stat}) \pm 1.34\,(\text{syst})\ \text{MeV},\end{aligned}$$

The measured ΔM from the fit can be converted into a mass measurements by adding the masses of the Λ_c^+ baryon and K^- meson. This yields

$$\begin{aligned}m(\Xi_c(2923)^0) &= 2923.04 \pm 0.25\,(\text{stat}) \pm 0.20\,(\text{syst}) \pm 0.14(\text{PDG})\ \text{MeV},\\ m(\Xi_c(2939)^0) &= 2938.55 \pm 0.21\,(\text{stat}) \pm 0.17\,(\text{syst}) \pm 0.14(\text{PDG})\ \text{MeV},\\ m(\Xi_c(2965)^0) &= 2964.88 \pm 0.26\,(\text{stat}) \pm 0.14\,(\text{syst}) \pm 0.14(\text{PDG})\ \text{MeV},\end{aligned}$$

where the last error quoted is the uncertainty on the measured Λ_c^+ mass [6].

6.6 Discussion

The $\Xi_c(2923)^0$ and $\Xi_c(2939)^0$ resonances have been observed for the first time. The $\Xi_c(2965)^0$ state observed in this analysis is likely a different resonance than the $\Xi_c(2970)^0$ resonance previously reported by Belle and BaBar due to the significant differences in the mass and width measurements. Figure 6.9 shows the experimental knowledge of the charmed baryon spectrum [6], where the newly observed Ξ_c^0 baryons are superimposed as magenta lines.

The observation of the two lightest new baryons $\Xi_c(2923)^0$ and $\Xi_c(2939)^0$ is a very nice development after the observation of the $\Xi_c(2930)^0$ by Belle in $B \to \Lambda_c^+ \overline{\Lambda}_c^- K$ decays [37] outlined in chapter 4, shown in Fig. 4.1(c). As Belle made the observation in a data sample with much lower yields, there were likely insufficient data to resolve the structure of two new baryons. The analysis presented in this thesis determines the existence of two separate Ξ_c^0 baryons.

The natural width and mass of the $\Xi_c(2965)^0$ baryon measured in this analysis is much smaller than the average width and mass of the $\Xi_c(2970)^0$ reported in the PDG. Hence, these might be two different baryons, supported by the fact that many states are predicted in this mass region, as is shown in Fig. 2.7. In the HQET description, strong decays of excited heavy baryons are transitions solely of the light degrees of freedom j_{qq} (Sec. 2.4.2). The state reported in this

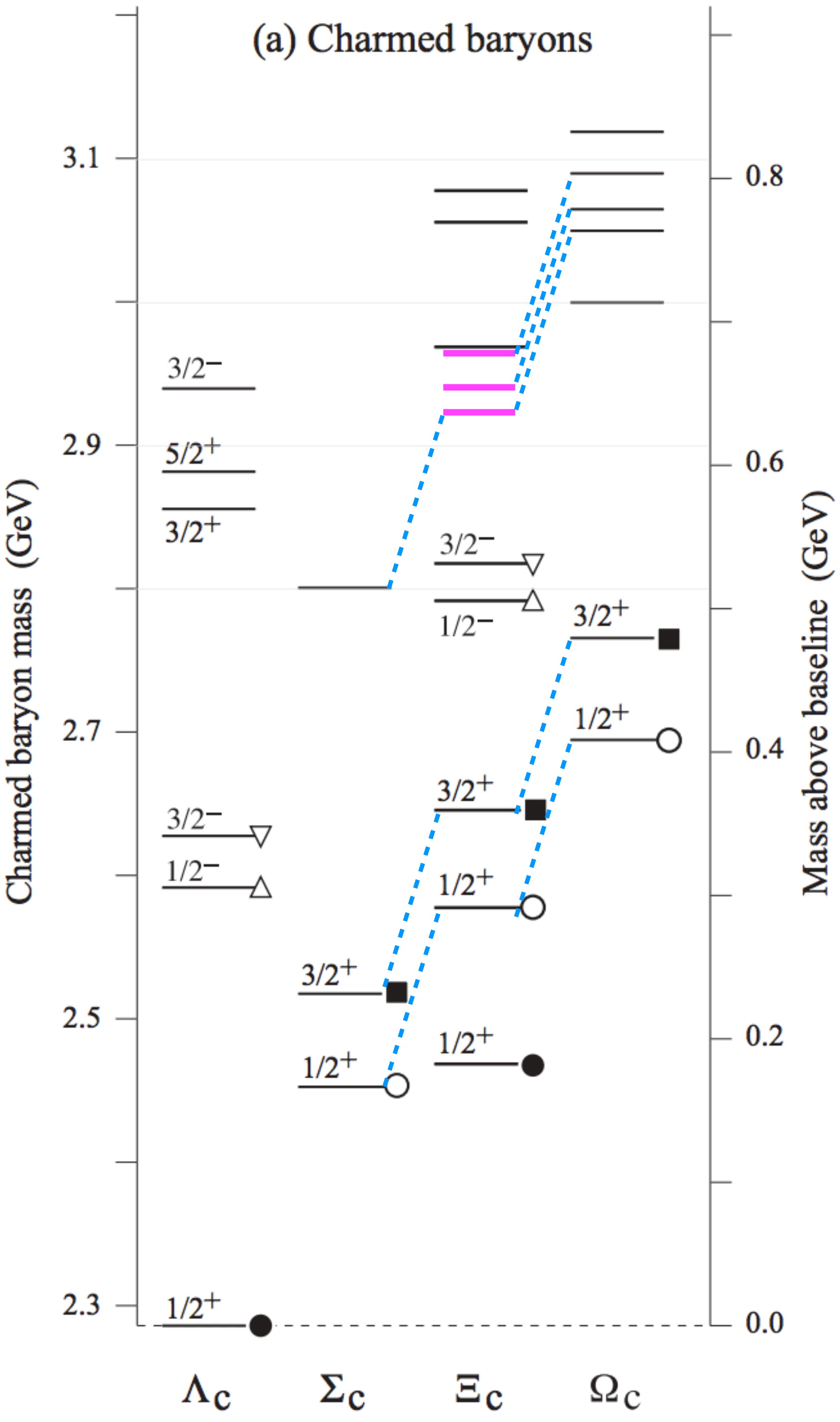

Figure 6.9 *The experimentally observed charmed baryon states are shown. The newly observed excited* Ξ_c^0 *states decaying to* $\Lambda_c^+ K^-$ *indicated by the magenta lines. Furthermore, the equal mass difference between several states is highlighted by the blue dashed lines. Figure adapted from [6].*

analysis decays to the $\mathit{\Lambda}_c^+ K^-$ final state (i.e. $j_{qq} = 0$) while the known state was observed in $\Sigma_c K^-$, $\Xi_c' \pi$ and $\Xi_c(2645)\pi$ (i.e. $j_{qq} = 1$) which further supports the interpretation of a different state. Consequently, the $\Xi_c(2965)^0$ baryon observed in this analysis has been interpreted as a third new state.

Finally it is interesting to notice that the equal spacing rule shows an interesting link to the excited $\mathit{\Omega}_c^0$ states decaying to $\mathit{\Xi}_c^+ K^-$ final state [31]:

$$m(\Omega_c(3050)) - m(\Xi_c(2923)) \simeq m(\Xi_c(2923)) - m(\Sigma_c(2800)) \simeq 125\,\mathrm{MeV}.$$

These states could belong to the same multiplet, as explained in Eq. 4.2. Furthermore,

$$m(\Omega_c(3065)) - m(\Xi_c(2939)) \simeq 125\,\mathrm{MeV}$$

and

$$m(\Omega_c(3090)) - m(\Xi_c(2965)) \simeq 125\,\mathrm{MeV}.$$

These links are shown in Fig. 6.9 by the blue dashed lines. It would seem that the spectrum of states observed in this analysis matches the resonances observed in the $\mathit{\Xi}_c^+ K^-$ spectrum. Measurements of spin parities will be crucial to confirm if they belong to the same multiplets.

Chapter 7

The TORCH Detector

The TORCH (Time Of internally Reflected CHerenkov light) is a research and development (R&D) project, which aims to provide particle identification (PID) of charged particles at low momenta (2-10 GeV/c). It exploits both Ring Imaging Cherenkov technology and the time-of-flight of different particle species over a specific path length. The project has a possible application in an upgrade of the LHCb experiment. It could be installed in the LHC long shutdown 3 (LS3) around 2025.

7.1 Physics of the TORCH project

Particles are classified according to their mass, m, and electric charge. The mass of a particle is defined by Equation 7.1, where p is the relativistic momentum, v is the velocity, $\beta = v/c$, and γ is the Lorentz boost factor $1/\sqrt{1-\beta^2}$, where c refers to the speed of light in vacuum. The mass of a particle can be written as

$$m = \frac{p}{c\beta\gamma}. \tag{7.1}$$

In high energy particle colliders, the momentum of a particle is typically measured using a tracking detectors and a magnet, where the curvature of the particle trajectory induced by the magnetic field B allows to deduce the momentum.

The TORCH detector aids with particle identification by measuring the velocity of particles passing through the detector. If the momentum is known from other detectors, Equation 7.1 can be used to determine the mass of the particle. This section of the chapter explains the two principle methods utilised in TORCH; Ring Imaging Cherenkov light and the time-of-flight technique.

7.1.1 Cherenkov light

Cherenkov radiation is the emission of electromagnetic radiation in the form of photons when a charged particle passes through a dielectric medium at a speed greater than the speed of light in that medium. This effect was first observed experimentally by P.A. Cherenkov in 1934 [65]. Three years later I. Frank and I. Tamm published a theoretical framework for this phenomenon [66].

Cherenkov photons are emitted at an angle with respect to the direction of particle motion. This shape is created by an electromagnetic shockwave stemming from the charged particle travelling through the medium. The photons are emitted at a characteristic angle θ_c, the so-called Cherenkov angle, where $\cos\theta_c = 1/n\beta$ (Eq. 3.1). Here, n is the refractive index of the medium.

The amount of Cherenkov light generated by a particle passing through a dielectric medium is given by the Frank-Tamm formula:

$$\frac{d^2N}{dEdx} = \frac{\alpha}{\hbar c} Z^2 \left(1 - \frac{1}{n^2\beta^2}\right). \tag{7.2}$$

In Equation 7.2, dN indicates the number of photons emitted, dE gives the energy range over a path length dx. The charge of the particle is Z, and α and $\hbar$ are the fine structure constant and the reduced Planck constant, respectively. This formula reduces significantly when assuming a particle charge of $Z = \pm 1$, a straight path and evaluating the constants.

$$\frac{dN}{dE} = 370L\left(1 - \frac{1}{n^2\beta^2}\right) \tag{7.3}$$

Equation 7.3 can be used to calculate the number of photons emitted over a path length L, given in centimeters and E is in eV.

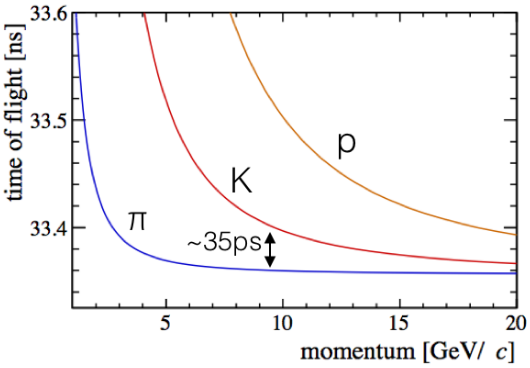

Figure 7.1 *Time-of-flight in nanoseconds between kaons (K), pions (π) and protons (p) over a 9.5 meter flight path. The time-of-flight is given from momenta ranging between 1-20 GeV/c. Figure obtained through internal communication with TORCH Collaboration members.*

7.1.2 Time-of-flight technique

The time-of-flight, t_{TOF}, of a particle over a flight path of length L can be measured by detecting it at two timing stations, after which its velocity can be determined using $\beta = L/ct$. The time-of-flight of a particle is defined as

$$t_{TOF} = \frac{L}{\beta c} = \frac{L}{c}\sqrt{1 + \left(\frac{mc}{p}\right)^2} \approx \frac{L}{c}\left(1 + \frac{1}{2}\left(\frac{mc}{p}\right)^2\right) \tag{7.4}$$

where for the last approximation, $p >> mc$ is required. Using Equation 7.4, the time-of-flight difference of kaons and pions at the same momentum, p, is defined as

$$\Delta t_{TOF(K-\pi)} = |t_{TOF(K)} - t_{TOF(\pi)}| \approx \frac{L}{c}\frac{1}{2p^2}(m_K^2 - m_\pi^2). \tag{7.5}$$

Figure 7.1 shows the time-of-flight difference between kaons, pions and protons over a 9.5 meter flight path. This is indicative of the flight path between the interaction point and TORCH with regards to a possible installation in the LHCb detector (see Figure 7.2), where TORCH is placed in front of the RICH2 subdetector. At a momentum of 10 GeV/c, the time-of-flight difference between kaons and pions over a 9.5 m flight path is about 35 picoseconds. This value establishes the requirements with regards to positive particle identification using the TORCH detector. These requirements are detailed in the next section.

7.1.3 Time resolution requirements

As mentioned previously, the time-of-flight difference between kaons and pions over a 9.5 m flight path at a momentum of 10 GeV/c is about 35 picoseconds. To get a 3σ separation between the two particle species, a per track resolution of about 12 ps is required. Simulations have shown that the expected number of Cherenkov photons detected using the TORCH detector is ~30. This leads to a single photon time resolution requirement of 12 ps $\times\sqrt{30}$ which is ~70 ps.

The two main contributions to the single photon time resolution are the intrinsic photon arrival time resolution of the detector and the time of propagation resolution. The single photon arrival time at the MCP-PMT includes the transit time spread (TTS) of the MCP as well as the jitter on the readout electronics. To achieve the required time resolution of the TORCH detector, the single photon arrival time is required to be 50 ps. This requirement has already been demonstrated using commercially available MCP-PMTs [67]. Furthermore, a precise knowledge of the time of propagation of the Cherenkov photons is necessary. Chromatic dispersion in the quartz spreads the time of propagation measurement. A precise measurement of the Cherenkov angle is used to correct for chromatic dispersion such that a resolution of 50 ps can be achieved.

The intrinsic time resolution and the time of propagation resolution are combined in quadrature, yielding an overall single photon time resolution of ~70 ps.

7.2 Design of the TORCH detector

Figure 7.2 shows the proposed location of the TORCH detector within the LHCb detector at the LHC. This section describes the TORCH detector.

The TORCH detector is based on the principles mentioned in Sec. 7.1.1 and Sec. 7.1.2, which are exploited in the BABAR DIRC detector [68] and the Belle II ToP detector [69]. The main difference between the TORCH detector and the BABAR DIRC detector is that TORCH utilises the Cherenkov angle to improve the single photon timing resolution, the BABAR DIRC measures only the Cherenkov angle using the track angle and momentum from the drift chambers. The Belle II TOP detector employs only one of the principles of the TORCH detector, namely the arrival time of the photons is used to extract the PID

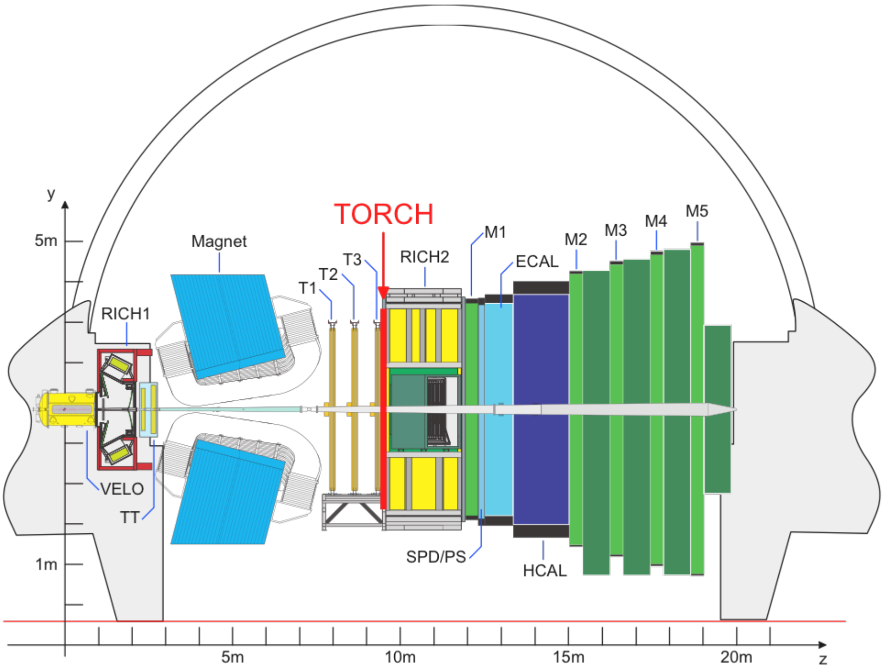

Figure 7.2 *Schematic overview of the LHCb detector where the proposed placement of the TORCH detector is indicated in red. Figure adapted from [25].*

information.

7.2.1 The TORCH modules

The TORCH detector consists of 18 modules as shown in Fig. 7.3. Each module is made up of a quartz plate of dimension $1 \times 66 \times 250$ cm^3 and a focusing block. The focusing elements and photon detectors line the top and bottom edges of the full detector. The dimensions are derived from the LHCb acceptance, which is ±300 mrad horizontally and ±250 mrad vertically. At 10 m downstream from the interaction point, this leads to a surface of 5×6 m^2 which is covered by 18 TORCH modules.

Each TORCH module consists of two main parts - the quartz radiator plate and the focusing block. These are described in more detail in Sec. 7.2.2 and Sec. 7.2.3.

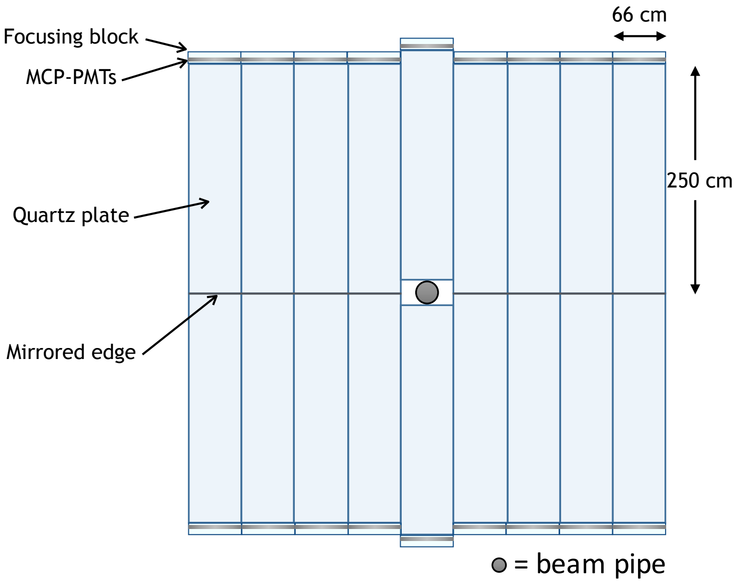

Figure 7.3 *Modular design of the TORCH detector. Each module is connected to a focusing block at the top or bottom edge with 11 MCP-PMT's to read out the data. Figure adapted from [70].*

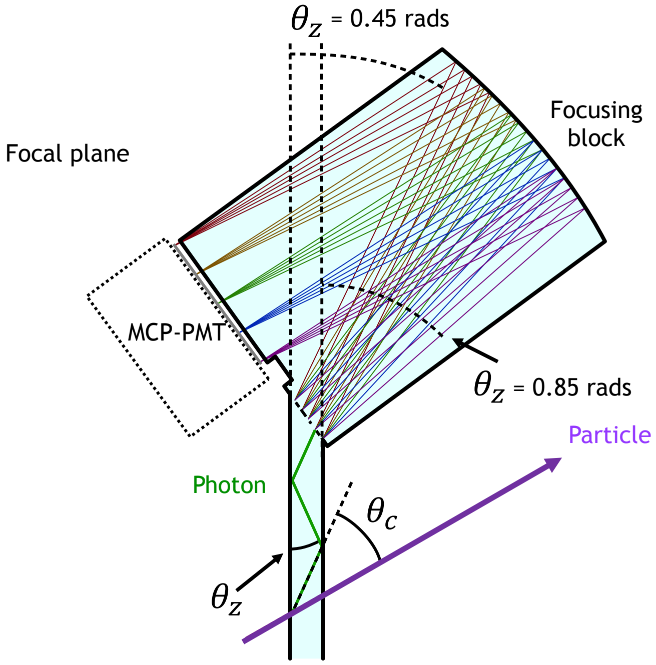

Figure 7.4 *A schematic cross section of a TORCH module. The quartz plate is attached to the focusing block using Pactan 8030 glue. The definition of the angle, θ_z is shown along with the focusing of five different photon angles ranging from 0.45 - 0.85 rad. Figure adapted from [70].*

7.2.2 The quartz plate

The quartz plate generates Cherenkov photons when a relativistic charged particle passes through, as explained in Sec. 7.1.1. The Cherenkov photons are transported towards the focusing block through total internal reflection (TIR). The angular requirement for TIR can be calculated using Snell's law and is defined by the refractive index of the quartz. Photons travelling in the opposite direction to the focusing block will be reflected by the mirrored edge and will thus reach the MCP-PMT's at a later time.

The angle θ_z is shown in Fig. 7.4 and is defined by the path length, L_{path} and the h, the distance between the point where the Cherenkov photon is emitted and the focusing block by Eq. 7.6. In simulations, the photon emission point is assumed to be halfway through the 1 cm thick radiator plate.

$$L_{path} = \frac{h}{\cos\theta_z}. \tag{7.6}$$

Two sources of scattering occur in the quartz radiator plate. Firstly, scattering due to the surface roughness and secondly Rayleigh scattering in the bulk material. The photon losses incurred in these processed are further described in Sec. 9.1.

7.2.3 The Focusing Block

The focusing block maps the angle θ_z onto the focal plane, as shown in Fig. 7.4. Similarly to the radiator plate, the focusing block is made of quartz, with a cylindrically mirrored surface used to focus the photons onto the MCP-PMT plane. The angular range covered is 0.45 - 0.85 mrad, which correspond to the smallest possible angle that fulfils the TIR requirements and the largest possible Cherenkov angle, respectively. The light is focused on the focal plane, where the focal point has been chosen to be 2 mm away from the focusing block exit window to account for the detector window thickness.

The focusing block and the quartz plate are glued together using Pactan 8030 glue, with transmission shown in Fig. 9.4. This choice of glue along with its implications are detailed in Sec. 9.1. The glue chosen affects the number of photons reaching the focusing block. In addition, the mirror reflectivity is dependent on photon energy and is accounted for in simulation. Details of the photon loss factors are further discussed in Sec. 9.1.

7.3 Photon detectors and Electronics

This section focuses on the Micro-Channel Plate Photonmultiplier Tubes (MCP-PMTs) used in TORCH as well as the electronics developed to read out the signals.

7.3.1 Micro-Channel Plate Photonmultiplier Tubes

The Micro-Channel Plate Photo-multiplier Tubes (MCP-PMTs) used in TORCH were specifically developed for the project by Photek[1]. TORCH sets conditions on the MCP-PMTs. These requirements include an excellent timing resolution with a single photon timing accuracy of 50 ps, high granularity and a long lifetime [71].

Fig 7.5 displays a schematic overview of an MCP-PMT. A photon hits the detector window, and gets converted into an electron at the photocathode. The voltage difference between the photocathode and the anode causes the electron to accelerate. The two microchannel plates are lined up such that the channels form a chevron pattern in order to maximise electron amplification and minimise ion feedback. The charge signal created by the amplification process reaches the anode, where it is measured.

The Cherenkov photons travelling through the TORCH detector undergo chromatic dispersion. A 1 mrad precision is required in the determination of the spatial angles in the TORCH detector to prevent this effect from being a leading source of uncertainty. Using simulation, it was found that the angular range of 400 mrad in the detector implies the need of 128 channels to achieve an uncertainty of 0.96 mrad on the angle θ_z. Within the TORCH segmentation of a 53×53 mm^2 active area, Fig. 7.6, a spatial resolution of 6.6 mm and 0.4 mm in the horizontal and vertical directions, respectively is required.

The lifetime requirement ensures that the MCP device can survive the high occupancy LHC requirement for several years. The MCPs used in the TORCH

---

[1] 26 Castleham Road, St. Leonards on Sea, East Sussex, TN38 9NS, United Kingdom, http://www.photek.com/

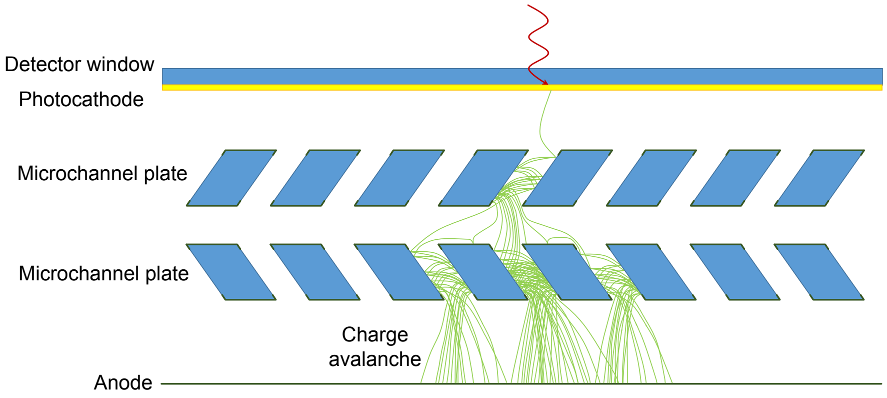

Figure 7.5 *Schematic overview of an MCP-PMT where a photon (red) is converted into an electron (green) creating a charge avalanche to highlight the working principle of the MCP-PMTs. Figure obtained through private communication with M. van Dijk [72].*

PMTs use an Atomic Layer Deposition (ALD) coating to meet the lifetime condition of at least 5 C/cm^2.

The MCP-PMTs described in this subsection combine the required properties.

The baseline TORCH design segmentation is 128x8 pixels on a 2 inch square tube, with an active area of 53x53 mm^2 as is displayed in Figure 7.6. On a 0.414 mm vertical pixel pitch, the cross talk between pixels needs to be considered. A thin dielectric is introduced between the charge collection and readout (AC coupling), shown in Figure 7.7. This allows to tune the spread of the MCP charge avalanche. A centroiding algorithm is used to reconstruct the photon position. With a charge readout on each anode pad, charge sharing precisely determines the photon position on the MCP-PMT through Eq 7.7, where X_γ is the position of the photon hit in the x-direction, x_i is the anode position of pixel i, q_i is the charge collected on pixel i and Q is the total charge detected on all pixels.

$$X_\gamma = \sum_{i=0}^{n} x_i \frac{q_i}{Q} \tag{7.7}$$

7.3.2 Readout electronics

The readout electronics developed for the MCP-PMTs are discussed in this section. There are employed by a prototype TORCH detector, from here on referred to as mini-TORCH, shown in Figure 8.7(a) in Section 8.3. The readout

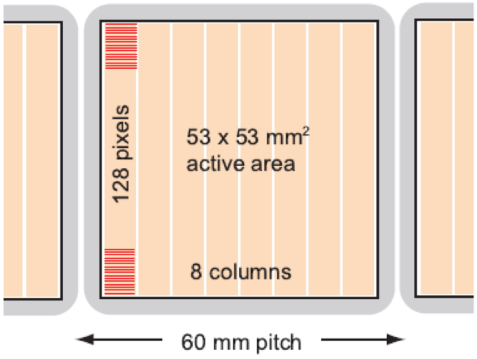

Figure 7.6 *Baseline TORCH design segmentation of the MCP-PMTs [73].*

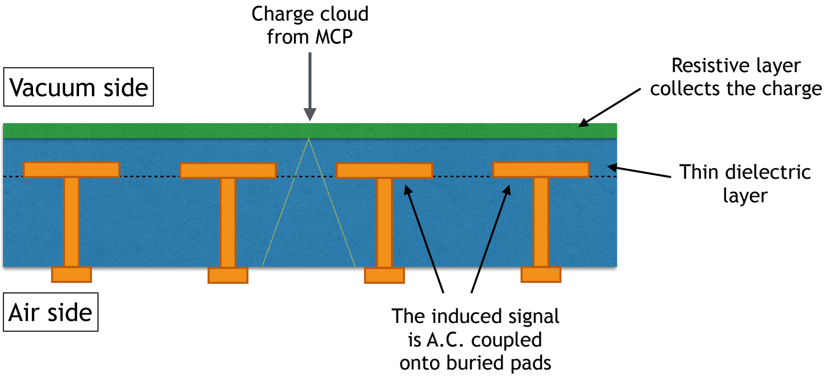

Figure 7.7 *Schematic overview of the MCP wall, including the AC coupling with a thin dielectric to help achieve the required granularity. Figure recreated from [72].*

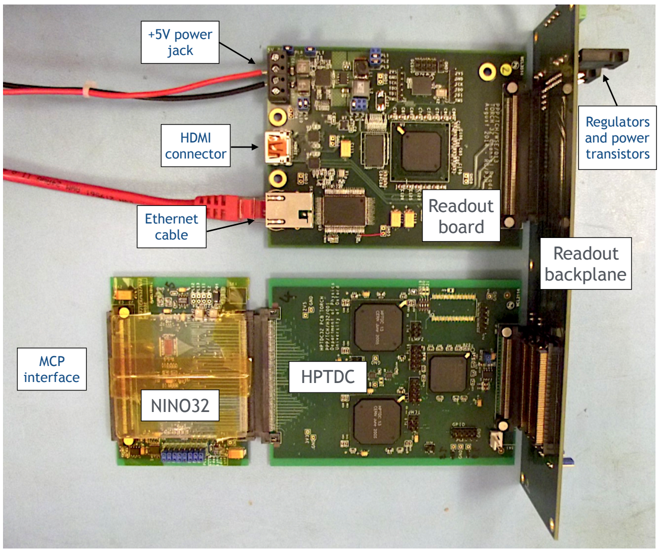

Figure 7.8 *The readout electronics used for the Phase III MCP-PMTs in miniTORCH.*

electronics are essential in achieving the desired timing resolution with the TORCH detector. A picture of the electronics is shown in Fig. 7.8.

The readout system consists of four customised boards: a front-end printed circuit board (PCB) with two 32-channel NINO boards [74] directly connecting to a 64×4-channel MCP-PMT. This links to a second PCB equipped with two high-performance time-to-digital converter chips (HPTDC) [75]. Finally, a readout back plane routes the HPTDC output signals to a readout board. The readout board connects to a HDMI cable (I/O) and an ethernet cable (I/O). The HDMI connector supplies the fan-out clock and trigger, which are received from the AIDA mini-Trigger Logic Unit (TLU) [76]. The mini-TLU was also successfully used during beam tests, linking for example to the Cherenkov counters and tracking telescope.

The NINO board used in the TORCH detector is based on the front-end chips developed for the Alice ToF system [21]. The MCP-PMT provides analogue signals which are amplified and discriminated by the NINO chip, as shown in Fig 7.9. This allows to output low voltage differential signals (LVDS). This is important since TORCH aims to measure single photon signals giving rise to small charges of typically 160 fC (about 1 million electrons) shared between 3-4 pixels. The output NINO pulse width will range from 2 ns to 7 ns. This signal is stretched by 10 ns such that the HPTDC can digitise both the leading edge and the trailing edge, as the HPTDC requires at least 6.25 ns before it can digitise a second signal.

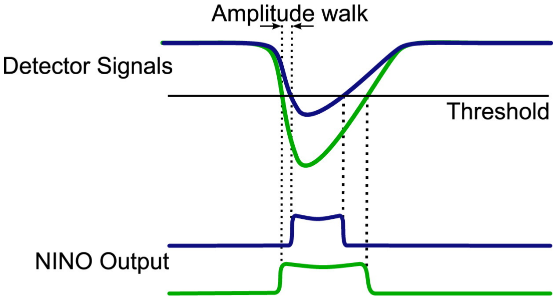

Figure 7.9 *The NINO working principle as an amplifier discriminator, converting the analogue input into a flat pulse [77].*

The HPTDC uses the NINO time-over-threshold approach to digitise the signals. Each HPTDC chip has 32 channels and digitises the signals in 100 ps time bins. The variations in gain affect the width, when measured as a time-over-threshold by the HPTDC. This is accounted for in data analysis by using a timewalk correction. In addition, a correction is required to account for the non-uniformity of the time bins in the HPTDC. This is referred to as the integral non-linearity calibration. The final correction required before performing data analysis is a charge to width calibration. The width of the output signal measured by the readout electronics depend on the charge measured at the anode. These three calibrations are discussed in further detail below.

7.3.3 Charge to width calibration

To perform the centroiding algorithm to use charge sharing, a charge to width calibration is required. The charge can be extracted through the width of the NINO signal, as the NINO channel response should only depend on the charge threshold settings. This calibration can be performed in a laboratory setting where a charge source is injected into the NINO to mimic and MCP-PMT response. The width of the signal can be measured. This calibration is expected to be the same for every pixel.

7.3.4 Time walk calibration

The NINO threshold setting determine whether a charge signal falls over the threshold yielding a LVDS signal corresponding to the length of the signal. However, the timing of the leading edges varies depending on the signal width. This effect needs to be eliminated, which is done using the time walk correction.

A per pixel calibration is necessary, which can be performed in the laboratory by measuring the time and width of laser signals.

7.3.5 Integral non-linearity calibration

The HPTDC chips split the 40 MHz clock into eight parts, each of which is divided into 32 bins of 100 ps, yielding a 10.24 GHz clock. The bins are expected to be of the same effective length, but this is not the case. To account for the difference in bin length, a large data sample of time stamps which are uncorrelated with the clock is required. The bins are expected to be filled evenly. To perform the calibration, each bin can be corrected by its deviation to the average number of entries in a bin.

Chapter 8

TORCH laboratory work and beam test activities

This section describes work that I performed in the laboratory at CERN, including a description of the point spread function measurement and quantum efficiency measurements. The chapter ends with a summary of the test beam campaigns that I was involved in.

8.1 Point Spread Function measurements

Using a setup available at CERN, shown in Fig 8.1, the gain and the point spread function (PSF) of the MCP-PMT used in the November 2017 beam test were measured. The gain directly relates to the number of electrons in the avalanche created within the MCP-PMT. The PSF is a measurement of the spatial spread of the electron avalanche measured with the MCP-PMT using a point source.

The setup used to measure the gain and the PSF is shown in Fig 8.1. Blue light from a pulsed laser diode is transported through a mono-mode optical fibre into a light-tight box. It travels through a lens and a neutral density filters before reaching the MCP-PMT. During the measurement, the point laser beam, creating a point-like light spot onto the MCP-PMT, was moved across 4 pixels (pixel pitch of 0.828 mm) in steps of 0.2 mm. The step size was chosen to avoid shining the light exactly on a pixel edge. The neutral density (ND) filters used are $d = 1.0$, $d = 0.8$ and $d = 0.7$, creating an overall density filter with optical

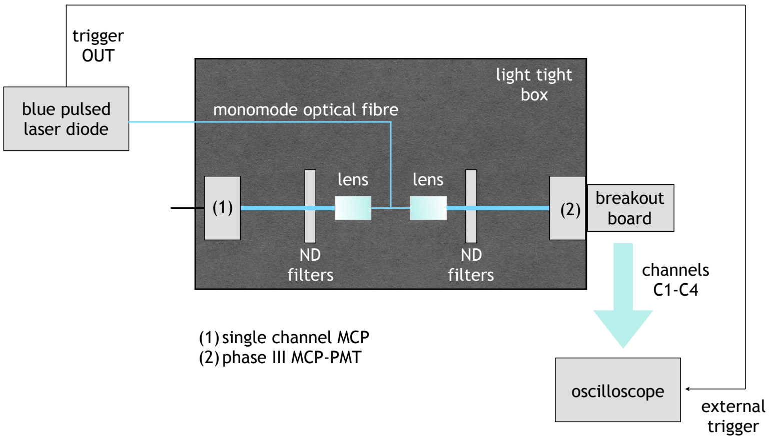

Figure 8.1 *Test setup at CERN for measurements with an oscilloscope. Blue light is pulsed through a mono-mode optical fibre into a light-tight box. It is split in two and travels through a lens and neutral densisty (ND) filters before it impinges onto the MCP-PMT. A breakout board allows recording the captured light on selected pixels on the oscilloscope.*

density $d = 1.0 + 0.8 + 0.7$. ND filters modify the intensity of the light. For a filter with optical density d, the fraction of light transmitted through the filter is defined as

$$\text{Fractional transmittance} \equiv \frac{I}{I_0} = 10^{-d}. \tag{8.1}$$

In Eq 8.1, I_0 is the light intensity before the filter and I is the intensity after the light passed through the filter. In a scenario where the light passes through three filters with optical densities d_1, d_2 and d_3, the optical densities are added together. In our case, the light is attenuated by roughly a factor of 300.

The 4 adjacent pixels on which the measurement is performed are connected to the scope through a breakout board. The 2 neighbouring pixels on either side are grounded using a 50 Ω resistor.

The charge measured in each pixel is recorded in a histogram, an example of which can be seen in Fig. 8.2. At every laser beam position, a histogram is created for the charge detected on each pixel. The fit consists of a Gaussian distribution to model the pedestal peak added to a second Gaussian function to account for the first photoelectron peak. The pedestal can be seen on the right hand side in Fig. 8.2, and it comes from the noise fluctuation measured when no photon is

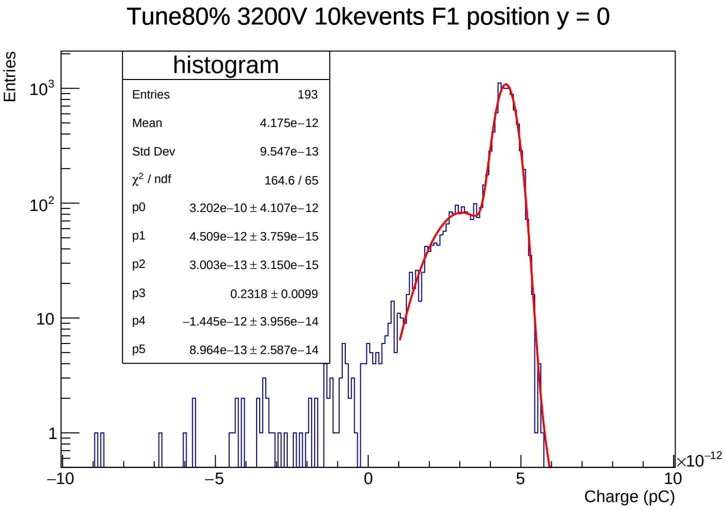

Figure 8.2 *A histogram showing the charge measured on pixel 1, where the pedestal has been fitted with a Gaussian distribution, indicated by a red line.*

detected.

When a photon is detected and multiplied in the MCP-PMT, the amount of charge detected depends on the gain. The gain of a PMT is defined as the average number of electrons generated in an electron avalanche from a single photon. The gain is susceptible to fluctuations due to several factors, including, but not limited to whether the electron goes into a hole in the micro-channel plate and the angle at which it hits the micro-channel plate.

The probability density function used to model the pedestal of the charge histograms is given in Eq. 8.2,

$$\mathrm{PDF} = \frac{A_0}{\sigma_0}\exp\left(\frac{-(x-x_0)^2}{2\sigma_0^2}\right) \tag{8.2}$$

where A_0, σ_0 and x_0 are the amplitude, standard deviation and mean of the pedestal peak, respectively. The first photo-electron peak in the charge histogram can be modelled using a second Gaussian function. The fit model should include such a Gaussian component for the peak created when one photon hits the MCP-PMT and possibly a second peak for when two photons are captured at the same time. The aim is to extract the charge collected on the MCP-PMT by measuring the difference in charge between the pedestal peak and the first photoelectron peak. The following steps outline the charge measurement:

- The expected number of photoelectrons emitted by the laser is given by a Poisson distribution, and can be changed by tuning the value of μ, which is the average number of photoelectrons that is emitted and amplified:

  $$P_\mu(N) = \frac{e^{-\mu}\mu^N}{N!} \tag{8.3}$$

  A low value for μ implies that the second photoelectron peak can safely be neglected.

- Since not much occurrence of two photoelectrons hitting the MCP-PMT is expected, the histogram mean provides a good estimate for the charge collected. The histogram mean is given in Eq 8.4, where $< Q >$ is the mean, Q_0 and S_0 are the pedestal charge and surface area, respectively. Similarly, Q_1 and S_1 are the photoelectron peak charge and surface area. Higher order contributions are neglected.

  $$< Q >= \frac{Q_0 S_0 + Q_1 S_1 + ...}{S_0 + S_1 + ...} \tag{8.4}$$

- Looking at the charge histogram in Fig. 8.2 it is easy to observe that the pedestal peak, Q_0, is not centered around 0. This must be corrected for. The corrected value of $< Q >$ is given by $< Q >_{\text{corr}}$. Neglecting higher order contributions, the pedestal charge from the average of the histogram is subtracted to calculate the charge of the photoelectron avalanche, as done in Eq. 8.5.

  $$< Q >_{\text{corr}} \approx \frac{Q_0 S_0 + Q_1 S_1}{S_0 + S_1} - Q_0 = \frac{(Q_1 - Q_0) S_1}{S_0 + S_1} \tag{8.5}$$

It should also be noted that μ can be inferred from the charge histogram, as S_1/S_0.

With this method, a plot of the charge per pixel, $< Q >_{\text{corr}}$, compared to the laser position is made, as is shown in Fig. 8.3. A Gaussian distribution is fitted for each pixel, of which the numerical results are listed in Table 8.1. It can be seen that the Gaussian functions do not tend to zero in the tails, which is an artefact of back-scattering of electrons on the MCP. The point spread function used in further analysis, such as described in Sec. 9, is the average of the four pixels, which is 0.746 mm. Ideally this measurement would be performed for every pixel, but since this measurement is a time intensive process, the assumption that the point spread function is uniform across the MCP-PMT was made.

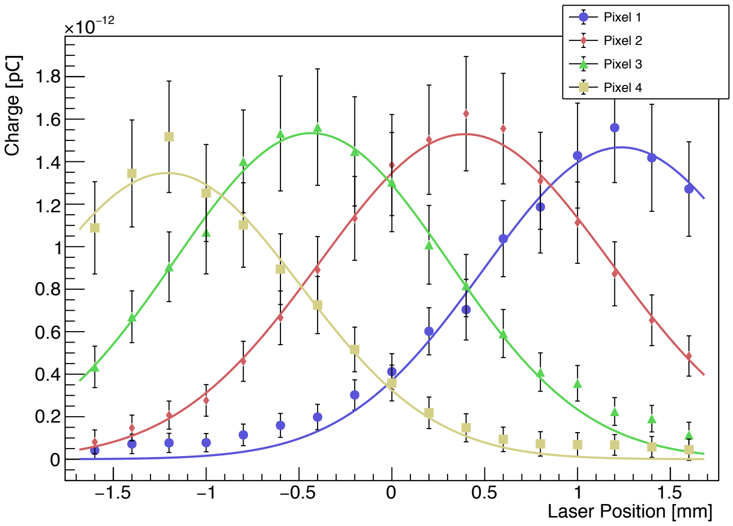

Figure 8.3 *A plot of the charge per pixel, given in pC, versus the laser position in mm. For each charge spread, a Gaussian distribution is fitted. The error bars stem from Poisson statistics.*

Table 8.1 *The numerical results from the Gaussian distributions fitted to the point spread function measurement, where σ is the resolution of the Gaussian distribution and is given in mm.*

	Pixel 1	Pixel 2	Pixel 3	Pixel 4
σ [mm]	0.74 ± 0.15	0.78 ± 0.04	0.74 ± 0.05	0.72 ± 0.13

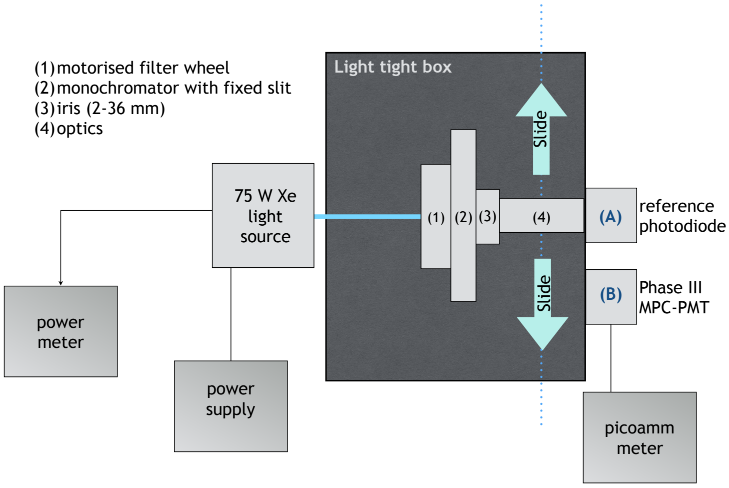

Figure 8.4 *The lab setup used to measure the QE of the MCP-PMTs. A tunable light source is used to send single photons onto either the reference photodiode or the Phase III MCP-PMT.*

8.2 Quantum Efficiency measurements

One source of photon losses in the TORCH system stems from the quantum efficiency of the MCP-PMTs. The quantum efficiency (QE) of an MCP is defined as the ratio of incident photons that are converted into electrons over the total number of photons hitting the tube input window. This measurement includes Fresnel losses.

The setup used in the laboratory to measure the QE is shown in the diagram in Fig 8.4. It consists of three separate elements, a tunable light source, a power meter and a reference photodiode. The tunable light source used is the TLS-300XU, consisting of the components in the turquoise box in Fig 8.4. The source used has some modifications to better fit our needs. The light source is a 75 W Xenon source. In addition, the monochromator gratings are optimised for near UV light to better match the Cherenkov wavelength spectrum. Measurements are taken from 200 - 800 nm wavelength. The tunable light source allows the user to very precisely adjust the amount of light let through, as well as its wavelength. The reference photodiode is the 818-UV/DB model. It is used to calibrate the amount of light seen and to measure its stability from the light source. The power meter utilised is model 1918-R. This model has since been phased out. The power meter is capable of measuring the power from pW to μW.

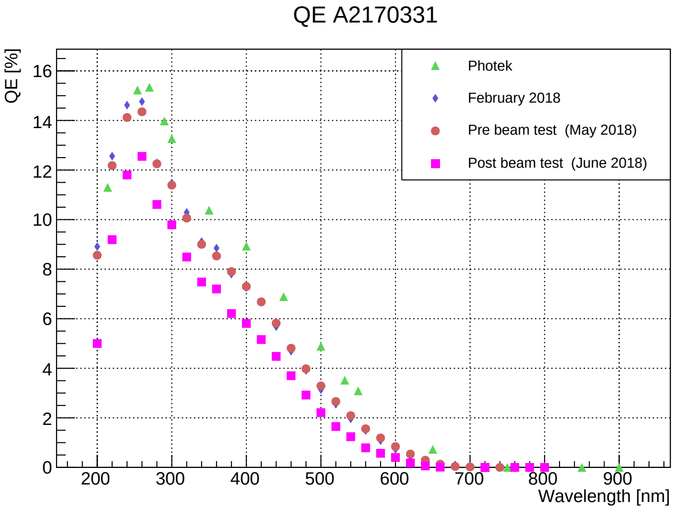

Figure 8.5 *The QE of the MCP-PMT used in the June 2018 beam test as a percentage as a function of the wavelength in nm, measured at different points in time.*

Using this setup, the QE of several MCPPMT prototypes was measured, including those used in the beam tests. Fig 8.5 shows the results of several QE measurements performed on the MCP-PMT used in the June 2018 beam test. The measurements are performed at different points in time. The green triangles display the QE as measured by the manufacturer, Photek. The blue diamonds show the measurement performed at CERN as soon as the MCP-PMT was delivered. A slightly lower performance than the performance measured by Photek was noticed, albeit within the contractual guidelines. It was remeasured immediately before the beam test performed in June 2018, as shown by the red circles. The QE remained stable between February and May. However, after the beam test the QE was measured again, indicated by the magenta squares. A clear degradation in the QE performance was observed after utilising the MCP-PMT in the beam test. It is not currently clear what caused this degradation. This could cause complications in the future as the MCP-PMTs need to be able to withstand High-Luminosity LHC conditions for several years. The manufacturer is aware of the behaviour and is investigating its cause.

Figure 8.6 shows the quantum efficiency of the MCP-PMT used in the November 2017 beam test. Unfortunately the QE of this MCP-PMT was not measured before the beam test due to time constraints. Similarly to Fig. 8.5, the green triangles indicate the QE as measured by Photek. However, the blue diamonds now show the QE measurement after the beamtest, performed in the center of the tube. In addition, a measurement was performed 16 mm off-axis, on the side

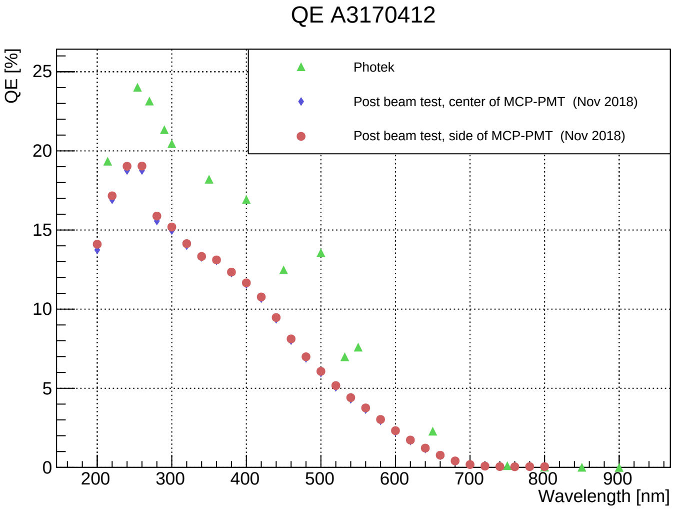

Figure 8.6 *The QE of the MCP-PMT used in the November 2017 beam test as a percentage as a function of the wavelength in nm, measured at different points in time.*

of the tube. This measurement is given by the red dots and is performed to test the QE uniformity of the MCP-PMT. Due to the overlapping measurement of the central measurement and the off-axis measurement, several of the blue diamonds are not visible. This indicates a very good agreement between the central and off-axis measurements. Another observation is that the measurements performed at CERN show a much lower QE than the data taken by Photek. This could be due to a degradation of the QE during the beam test, as was observed with the MCP-PMT used in the June 2018 beam test. However, due to a missing measurement before beam test this cannot be confirmed. Future measurements with different MCP-PMTs should give more insight.

8.3 Summary of beam test campaigns

Using the latest prototype of the MCP-PMTs, three successful beam test campaigns have been carried out at the East Hall T9 facility at CERN. During each beam test, a three week period was available. The beam tests in November 2017 and June 2018 used a small prototype called “mini-TORCH” (see Figure 8.7(a)). The quartz plate dimensions of this module is $120 \times 350 \times 10$ mm^3, and the module can accommodate two MCP-PMTs. The latest beam test, performed in October 2018 used a full-width, half-length TORCH module, referred to as “proto-TORCH”, with quartz dimensions of $660 \times 1250 \times 10$ mm^3

(a) *mini-TORCH* **(b)** *proto-TORCH*

Figure 8.7 *Photographs of mini-TORCH (a), used in the November 2017 and June 2018 beam tests and proto-TORCH (b), used in the October 2018 beam test.*

(see Figure 8.7(b)), which can be instrumented with 10 MCP-PMTs. In the October 2018 beam test, two MCP-PMTs were mounted in proto-TORCH.

Chapter 9

Photon Counting

The timing resolution measurement is an obvious benchmark in determining the performance of the time-of-flight TORCH prototype. However, to get a more complete overview it is essential that the photon yield is studied as well. This section describes the work I performed regarding the TORCH photon yield on data collected in the November 2017 and June 2018 beam tests carried out at the Proton Synchotron at CERN, as described in Sec. 8.3. The aim of the analysis is to compare the number of photons measured per particle passing through the detector using beam test data with the expected number of photons from simulated data.

To display the data, hits measured with the MCP-PMT are collected on a hitmap, as shown in Fig. 9.1. A hit is defined as a pixel on the MCP-PMT picking up a charge signal above threshold. Here Fig. 9.1(a) shows the November 2017 data and Fig. 9.1(b) is generated using the June 2018 data. In both figures, the top part of the MCP-PMT, above pixel number 40, has been removed since no light is observed in this area. The x-coordinate defines the pixel rows, and the y-coordinate gives the pixel columns. These hitmaps show the pattern of detected MCP-PMT hits. Since the Cherenkov photons are emitted in a cone, the reflections in the quartz radiator are captured on the MCP-PMT in hyperbola-like patterns. Reflections off the side of the quartz module give rise to a folding of this pattern. The beam test data are performed using a beam which has been positioned 5 mm from the edge of the quartz plate below the MCP-PMT, in the vertical middle. This position folds the pattern as cleanly as possible, such that pattern reconstruction is possible. The width of the observed bands in the

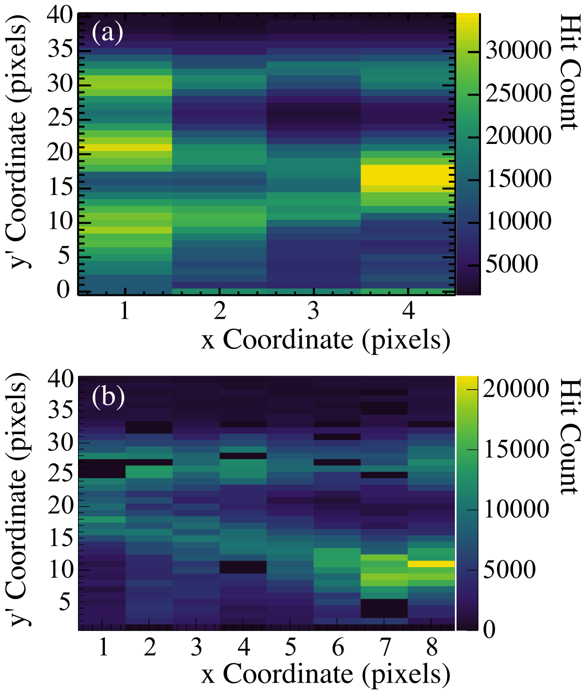

Figure 9.1 *Hitmaps showing the number of hits per pixel measured in the beam tests of November 2017 (a) and June 2018 (b). The black pixels in (b) indicate the channel is dead and does not receive any light. In both plots, the top part of the MCP-PMT, above pixel number 40, has been removed since no light is observed in this area.*

pattern in an artefact of chromatic dispersion in the quartz.

Fig. 9.1(b) shows the distributions of pixel hits in the June 2018 beam test. The dead pixels are coloured black. It has to be noted that the black pixels with y-coordinate 32 are actually time-reference channels rather than dead channels. This MCP-PMT used suffered from a relatively large number of dead pixels where no light was captured. This is attributed to broken wire bonds of the NINO board. This occurred since the NINO board where being developed simultaneously with the MCP-PMTs. Therefore careful testing before the beam test was not possible. However, this issue has been resolved in a later beam test (although not described in this thesis).

9.1 Simulation

A *GEANT*4 [47] simulation of the mini-TORCH prototype was initially developed in a thesis where a detailed description can be found [72]. This simulation is run to estimate the number of photons captured per particle passing through the detector. A pencil beam of 8000 particles is aimed 5 mm from the side of the quartz plate at the vertical center, positioned similarly to the conditions at which data during the beam test were taken. The beam momentum is set to 5 GeV/c^2. To further simulate the test beam conditions, the beam consists of 2/3 protons and 1/3 pions.

The critical challenge in analysing data is to correctly quantify the photon losses, caused by scattering and absorption effects. The main loss factors and how they have been implemented in the simulation are described below.

Surface roughness: The surface roughness of the quartz plate determines what fraction of Cherenkov photons is scattered. This is heavily dependent on the degree of polishing of the radiator plate. Since every single photon in TORCH will undergo around 100 reflections, the scattering probability needs to be small in order to preserve a good number of photons. The Rayleigh smallness criterion [78] states that if $2\pi\sigma/\lambda << 1$, a statistical interpretation of the scattering probability can be used. In this formula, σ indicates the size of the bumps on the surface, i.e. the surface roughness, and λ is the wavelength of the incoming light.

The contractual surface roughness requirement for the quartz plate used in mini-TORCH is 1.5 nm. An inteferometric measurement of the surface roughness performed by the manufacturer, Schott[1], shows a surface roughness of 1 to 1.2 nm. The BABAR DIRC has a surface roughness of 0.3 nm [68] and the Belle II TOP surface roughness is 0.5 nm [69].

Figure 9.2 shows the effect of the surface roughness on the photon yield, tested using simulated data where the surface roughness is the only variable that is varied among the simulated data samples. Even though the variations in photon yield are minimal (note the suppressed y-axis scale), a larger surface roughness means more scattering and thus the average photon yield is lower. The remainder of this chapter uses a simulated data set where the surface roughness is set to 1.2 nm, as this is the value given by the manufacturer.

Rayleigh scattering: As a photon passes through a medium, it could elastically scatter off small particles in this medium. This phenomenon is called Rayleigh scattering. Within mini-TORCH we expect to only lose a small amount ($< 5\%$) of photons due to this effect. This is modelled within the *GEANT*4 simulation,

---

[1] SCHOTT AG Lighting and Imaging. Otto-Schott-Strasse 2, 55127 Mainz, Germany. www.schott.com/lightingimaging

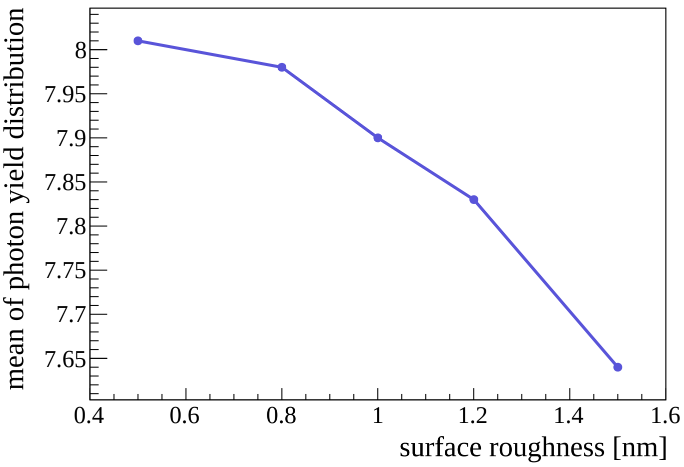

Figure 9.2 *The average photon yield in terms of the surface roughness in mini-TORCH, as estimated from simulated data. Note the suppressed y-axis scale.*

as it is a standard process that is implemented in the program.

Mirror reflectivity: The cylindrical surface of the focusing block acts as a mirror to focus the photons onto the focal plane where they can be read out with MCP-PMTs. The mirror reflectivity has been studied at CERN using a Suprasil quartz sample covered with 0.120 nm of aluminium where the angle of incidence of the photons is 30 degrees [79]. The results are shown in Fig 9.3.

The mirror reflectivity is fairly constant over the full energy range and has been added to the mini-TORCH simulation. It is not known how accurately these measurements represent the actual photon losses within mini-TORCH and an updated measurement would be desirable.

Gluing of the quartz plate to the focusing block: The choice of glue to bind the quartz plate and the focusing block is Pactan 8030. It is a silicon based adhesive with transmission characteristics up to 6 eV, which is higher than most other marketed glues. It has not been extensively tested so many of its properties are unknown. Most notably, the characteristics regarding the refractive index of this material are unknown. However, it is chosen since it does not set rigidly and therefore retains the option to re-glue to prototype if necessary. The transmission curve of the adhesive is shown in Fig 9.4.

Quantum efficiency: The quantum efficiency is measured according to the procedure described in Sec. 8.2. The quantum efficiency varies from tube to tube

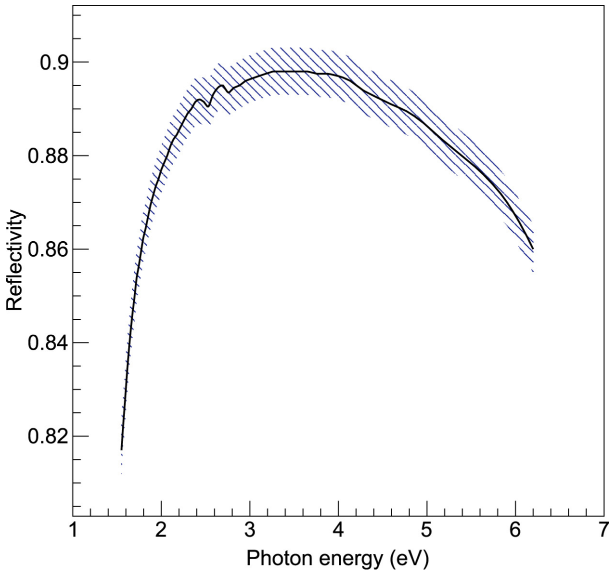

Figure 9.3 *The mirror reflectivity given as a function of photon energy, measured using a Suprasil quartz sample with a 0.120 nm layer of aluminium, where the angle of incidence is 30 degrees. The estimated measurement error is roughly 0.5%, indicated by the shaded area. Note the suppressed vertical scale. Plot taken from [79].*

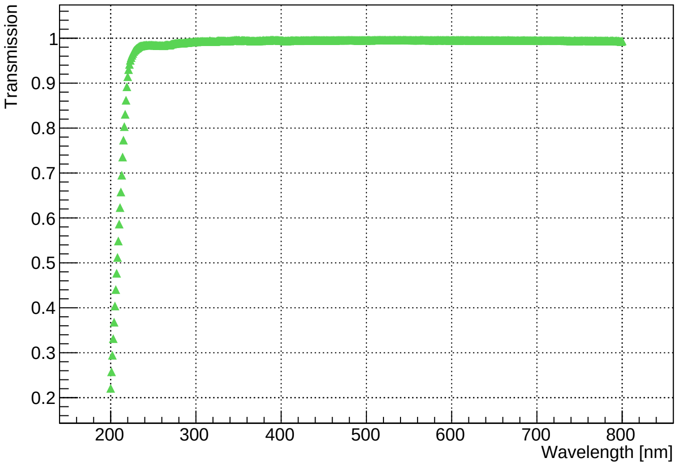

Figure 9.4 *The transmission curve of Pactan 8030 adhesive, used to glue the quartz plate and focusing block together. Plot adapted from [80].*

and therefore needs to be updated depending on the tube used during data taking.

The November 2017 data analysis is performed on a 4x64 MCP-PMT, for which the QE measurement is discussed in Section 8.2, see Fig. 8.6. The efficiency correction applied to simulation are the data points taken at the center of the MCP-PMT, given by the blue diamonds in the figure. The efficiency correction to the simulated data stemming from the QE for the June 2018 test beam data is the data taken after the beam test, given by the magenta squares in Fig. 8.5.

Geometric efficiency: The TORCH MCP-PMT's are 60×60 mm^2 in size, with an active area of 53×53 mm^2 [71]. The MCP-PMT's are placed linearly in one row within the TORCH detector, as shown in Fig. 7.6. Due to this configuration, the factor to account for the geometric efficiency is given by 53/60. This factor is applied to the number of photons captured by the detector in simulation.

Collection efficiency: The collection efficiency (CE) is defined as the probability that a photoelectron emitted from the photocathode will fall into a channel and results in the development of an electron avalanche in the MCP. The CE depends on many MCP-PMT properties, including, but not limited to the voltage at which the MCP-PMT is operated, the depth of the electrode penetration into the channels, and above all, the open area ratio (OAR). The OAR is defined at the surface of the channel holes divided by the total surface of the MCP-PMT. The open area ratio of the MCP-PMTs used in the TORCH detector is 0.59.

The collection efficiency of a MCP-PMT is difficult to measure in the laboratory. Therefore, no accurate measurements of the MCP-PMTs used in the TORCH detector exists. Photek is planning to provide the TORCH collaboration with these measurements in the future. Nevertheless, the collection efficiency is an important factor to take into account for the photon yield analysis since it will likely be one of the main contributors to photon losses. The collection efficiency used for the analysis presented in this chapter is based on the findings summarised in two papers.

The first paper measures the CE of a large sample of MCP-PMTs produced in Russia [81]. In addition, the CE of a conventional dynode PMT is measured for verification. The OAR of the tubes considered is approximately 0.6. The CE distribution for the MCP-PMTs tested is given in Fig. 9.5. The average CE observed is close to the OAR of the PMTs considered. However, a large performance spread of measured CE values is found. This leads to the conclusion that to get an accurate value for the CE every MCP-PMT should be measured

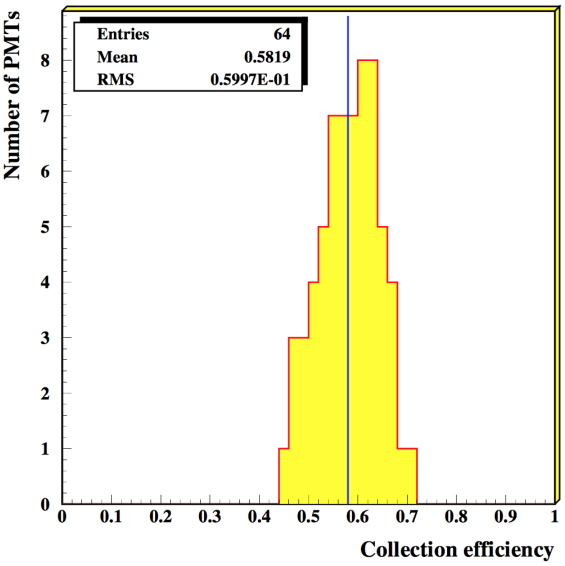

Figure 9.5 *The CE distribution for 64 MCP-PMTs produced and tested in Russia. Figure taken from [81].*

separately.

A second paper discusses the so-called 'high collection efficiency' (Hi-CE) MCP-PMTs in comparison to conventional MCP-PMTs [82]. The OAR of both type of MCP-PMTs is roughly 0.64. The paper concludes that the Hi-CE MCP-PMTs have a CE greater than 90%, but a slight degradation in transit time spread (TTS) is observed. The transit time is of great importance for the TORCH project. Conventional MCP-PMTs tested have a CE close to the OAR.

The MCP-PMTs used in the TORCH project have been treated by an atomic layer deposition (ALD) coating. This offers several performance advantages to the MCP-PMTs, among which an increase of the CE of the MCP-PMTs by approximately 20% according to Photek. The ALD coating improves secondary emission yield on to the MCP, increasing the CE and the gain of the MCP-PMT. A 20% increase in CE would bring the TORCH MCP-PMTs up to a similar level to the Hi-CE MCP-PMTs. Photek furthermore expects to see no deterioration in the timing performance due to the ALD coating. However, since no absolute measurements in support of this claim exist, a collection efficiency of 0.59 is applied to the simulated data. This value is equal to the OAR of the MCPs.

Protons vs. pions: As a cross-check, the difference in photon yield between protons and pions is investigated. Figure 9.6 displays the difference in photons seen per event between protons and pions, where the protons are shown in red

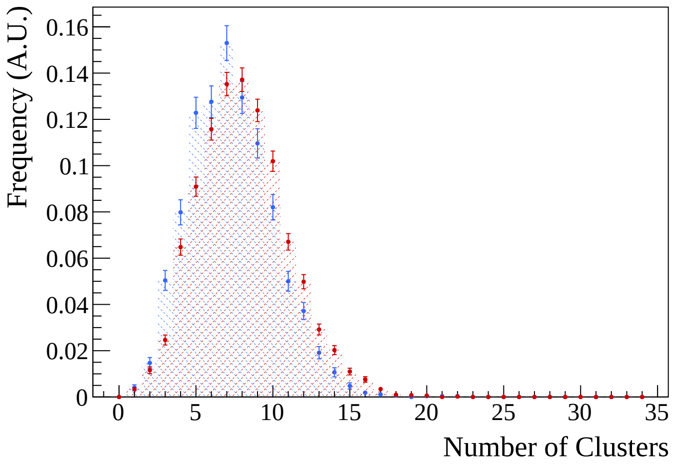

Figure 9.6 *Comparison of the normalised number of photons observed per event, depending on whether the particle passing through the detector is a proton (blue) or a pion (red). The histograms have been normalised.*

and the pions in blue. The histograms are normalised for ease of comparison. The mean of the histogram displaying the photon yield for pions is 8.08 ± 0.04, whereas the mean of the proton photon yield histogram is 7.35 ± 0.05. A slightly larger number of photons is observed when a pion passes through the detector compared to the number of protons. This is a marginal difference that can be tracked back to the number of Cherenkov photons generated in the quartz plate when the particles pass through the detector. It stems from the fact that pion tracks at a momentum of 5 GeV are slightly more relativistic than those of protons. Numerically, their velocity β_π is closer to one than β_p, resulting in a higher number of emitted Cherenkov photons, which is calculated using Eq. 7.3.

Clustering in the simulation: As explained in Sec. 7.3.1, a single incident photon will create a charge avalanche and give hits on several neighbouring pixels, after which the photon hit position can be reconstructed using a charge sharing algorithm. Thus, during data analysis, hits which are close together in time and space are clustered to reconstruct single photon hits. The clustering algorithm adheres to the following criteria:

- The hits must fall within the same pixel column.
- The hits must be in neighbouring pixel rows.
- The arrival time of the hits must be within 1 ns of each other.

Separate hits will only be clustered together if, and only if all three criteria outlined above are fulfilled. The MCP-PMT used in the June 2018 beam test suffered from a number of dead channels, as indicated by the black pixels in Fig. 9.1. To account for this, the clustering algorithm has been modified slightly. If two clusters fall on either side of a dead channel and the hits are measured to be within 2 ns of each other, the clusters are merged together. It is possible for two photons that hit the detector close enough together in time and space to be clustered together. How often this occurs can be derived from simulation.

Based on the gain and the point spread function of the MCP-PMT, the size of the charge avalanche can be calculated. Signal discrimination is applied in the NINO chip, such that charges below threshold are not registered. The threshold is set at 30 fC. The point spread function of the MCP-PMT used in the November 2017 beam test has been measured in the lab, as outlined in Sec. 8.1. The gain of the MCP-PMT is dependent on the number of electrons created in the electron avalanche. The gain will fluctuate with each photon that hits the PMT and depends on the final number of electrons in the charge avalanche and the voltage at which the MCP-PMT is operated. The gain fluctuations are not taken into account in this part of the analysis. The gain used stems from a measurement performed on the MCP-PMT from the November 2017 beam test done at CERN, and is 1.82×10^6 electrons, corresponding to a charge of 291 fC. Figure 9.7 displays the number of pixels that should receive a hit depending on the position of the photon hitting the detector for the November 2017 beam test MCP-PMT. In the x-direction (pixel columns) we should observe only one pixel with a hit, unless the photon hit is close to the side, in which case two pixels will receive a hit. The y-direction corresponds to the pixel rows, which are much smaller. Therefore a photon will create a hit on 3 or 4 pixels, depending on its incident position.

Since a different MCP-PMT has been used in the June 2018 beam test, the difference in PSF needs to be accounted for. Due to time constraints the PSF of the MCP-PMT used in the June 2018 beam test was not measured. One of the main factors affecting the size of the charge avalanche is the thickness of the dielectric layer burying the anode contact pads in the MCP-PMT. The MCP-PMT used in the June 2018 beam test has a dielectic layer thickness of 0.3 mm, whereas the November 2017 beam test MCP-PMT has a dielectric thickness of 0.5 mm. An internal study performed by Photek shows that the PSF for MCP-PMTs with a dielectric thickness of 0.5 mm has a PSF 18% larger than that of a MCP-PMT with a dielectric layer of 0.3 mm thick. This number was utilised to extrapolate the expected PSF for the MCP-PMT used in the June 2018 beam

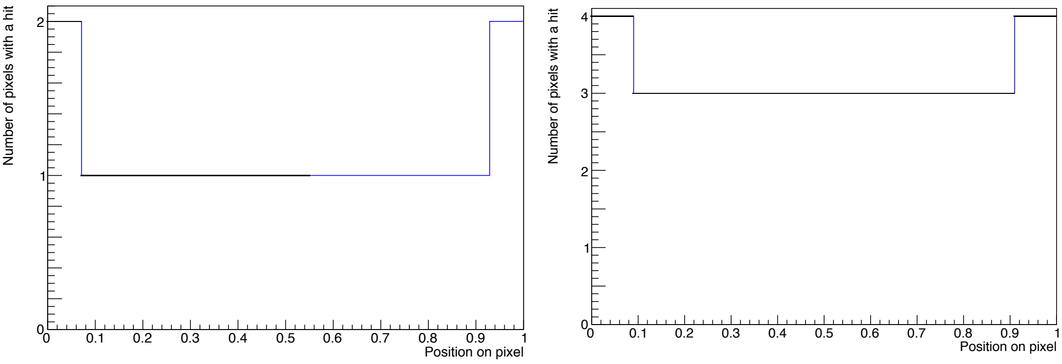

(a) *x-direction* **(b)** *y-direction*

Figure 9.7 *Number of pixels affected by a photon hitting the* 4×64 *pixel MCP-PMT in the x-direction (a) and the y-direction (b).*

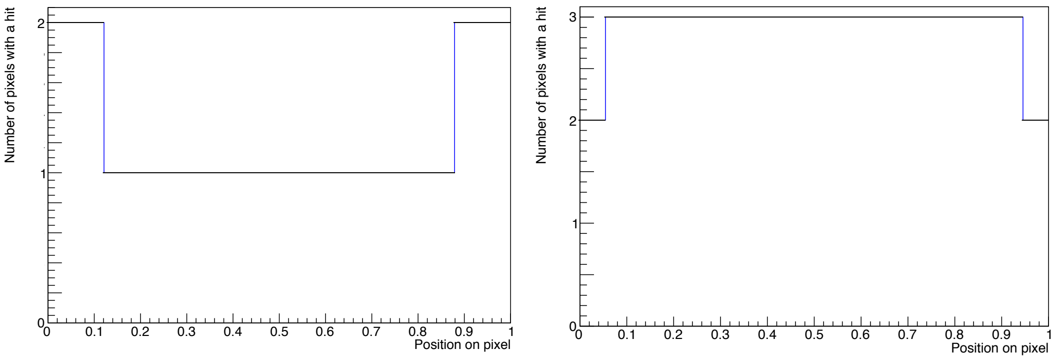

(a) *x-direction* **(b)** *y-direction*

Figure 9.8 *Number of pixels affected by a photon hitting the* 8×64 *pixel MCP-PMT in the x-direction (a) and the y-direction (b).*

test. Using the information of the decreased pixel size in the column direction and PSF we can recalculate the expected number of pixels affected by a photon hitting the MCP-PMT for the June 2018 beam test. Figure 9.8 displays the number of pixels that should receive a hit depending on the position of the photon hitting the detector for the June 2018 beam test MCP-PMT.

Using this information, a hitmap is simulated for every particle event. These are displayed in Fig. 9.9 and in Fig. 9.10 for the MCP-PMT used in November 2017 and June 2018, respectively. The black cross indicates the position where the photon hits the MCP-PMT and the coloured pixels show which pixels are likely to receive a hit. Most photon hit clusters are easy to distinguish although these plots nicely illustrate that photons hits close together in space occur reasonably often.

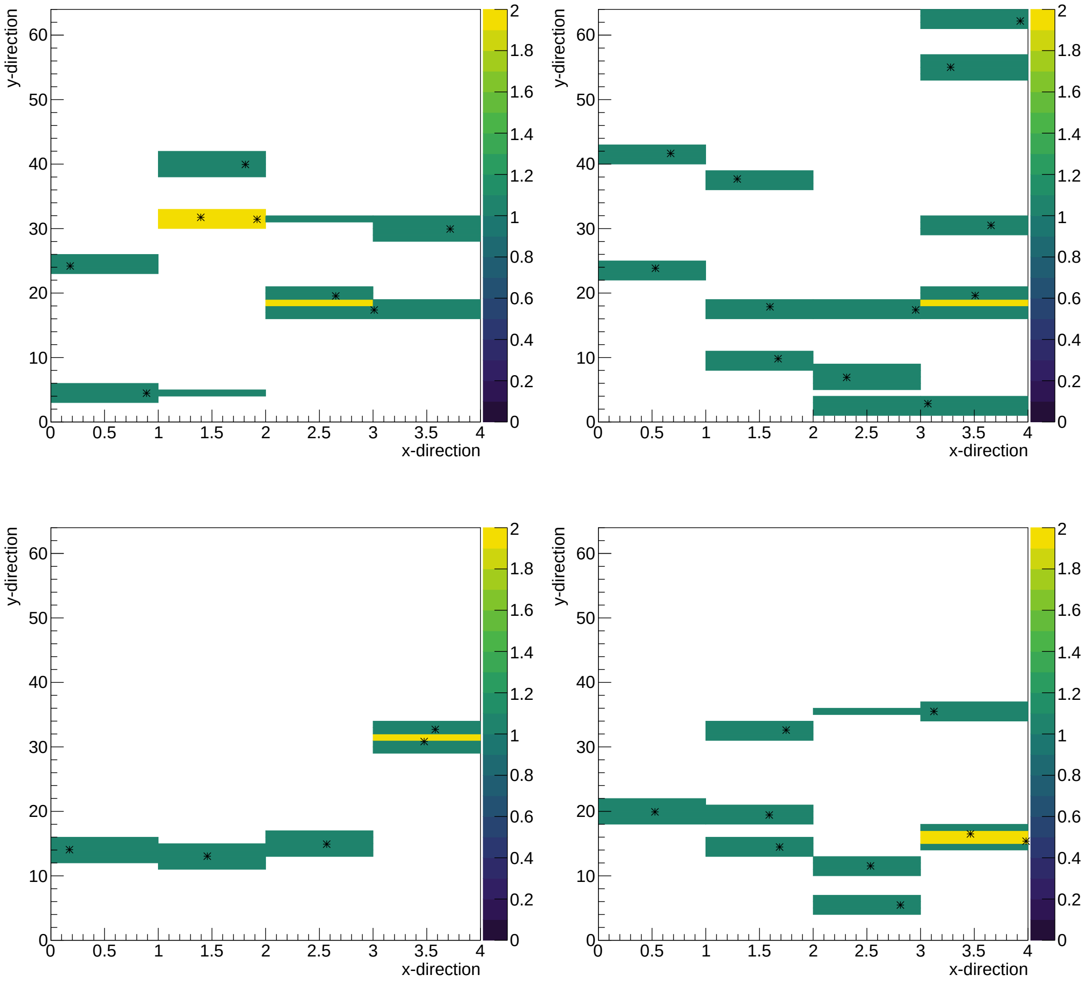

Figure 9.9 *Simulated hitmaps of the 4 × 64 MCP-PMT used in the November 2017 beam test when calculating the expected charge avalanche around each hit.*

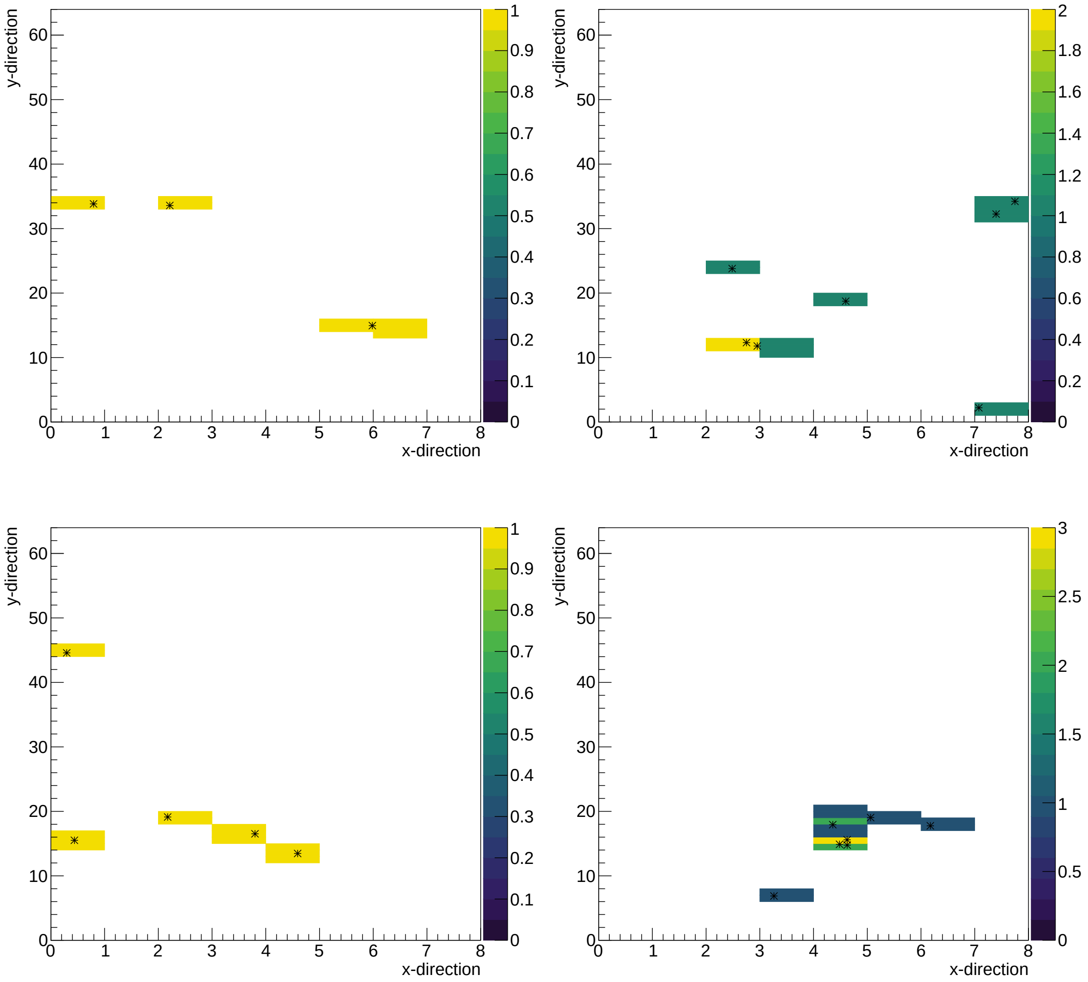

Figure 9.10 *Simulated hitmaps of the* 8×64 *MCP-PMT used in the June 2018 beam test when calculating the expected charge avalanche around each hit.*

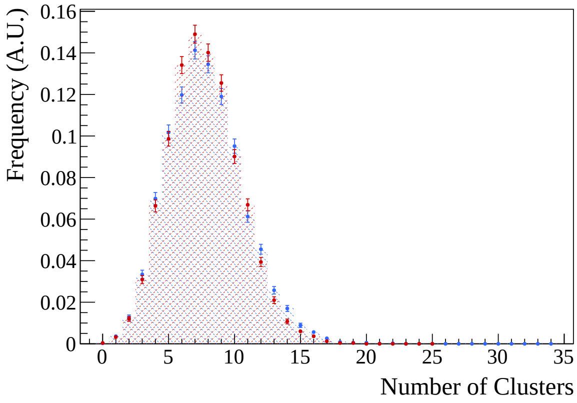

(a) *November 2017 MCP-PMT*

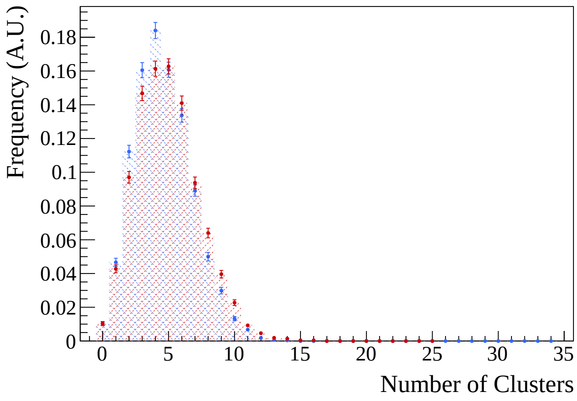

(b) *June 2018 MCP-PMT*

Figure 9.11 *Raw number of photons captured by the MCP-PMT (blue) and number of photons when clustering is applied (red) for simulated data for the test beams in November 2017 (top) and June 2018 (bottom).*

When considering the timing of these hits and applying the clustering algorithm, we can compare the number of raw photon hits with the number of clustered photons. This is illustrated for simulated events in Fig. 9.11, and the numerical results are given in Tab. 9.1.

Using the November 2017 beam test MCP-PMT, the average number of photon hits seen in simulation after the clustering algorithm is applied is slightly lower than the raw number of photon hits. The average number of photons seen only reduces a little, indicating that not many photons are lost due to the requirements of the clustering algorithm. Looking at the June 2018 results, the number of raw photon hits is 4.62 ± 0.02, whereas the mean number of clustered photons is 4.96 ± 0.03. Contrary to the trend seen in the 4×64 pixel MCP-PMT, here the

Table 9.1 *Simulated raw number of photons captured by the MCP-PMT and the number of photons when clustering is applied.*

	Raw	Clustered
November 2017	7.83 ± 0.03	7.69 ± 0.03
June 2018	4.62 ± 0.02	4.95 ± 0.03

average number of photon clusters increases when compared to the raw number of photon hits. This has several reasons. Firstly, the smaller pixel pitch in the column direction implies that it is more likely for a photon cluster to be spread among two columns, thus being split into two separate clusters. Secondly, the smaller PSF of the MCP-PMT used in the June 2018 beam test means that the charge avalanche created in by the electron multiplying within the MCP is smaller, and therefore it is less likely for two photon hits to be clustered together. The results obtained in this subsection are as we would expect.

9.2 Data Analysis

The data gathered in the beam test are analysed by forming clusters according to the clustering algorithm described above. Initially it is of interest to look at the amount of hits that generally make up a cluster. In figure 9.12 the number of hits seen per cluster are displayed. A clear peak of clusters of size one can be seen in the November 2017 beam test data. These can be explained by two phenomena. Firstly, a faulty hit is produced by the electronics in the MCP-PMT stemming. Secondly, it is possible that an electron has a smaller gain within the MCP-PMT, therefore only creating a single pixel hit. The June 2018 data clustersizes are shown in Figure 9.12(b). The peaking structure seen in the data gathered at the November test beam has disappeared. This may be due to the fact that the June 8 × 64 MCP-PMT uses a different set of electronics. The distribution from the June 2018 beam test data matches the expected Poissonian distribution. The difference can be attributed to a difference in electronics used between the two data sets.

A comparison between the photon yield including and excluding the clusters of size one is shown in Fig. 9.13. The numerical results are given in Tab. 9.2. As expected, a clear decrease in the number of photons observed per particle passing through the detector is seen when the clusters of size one are removed from the

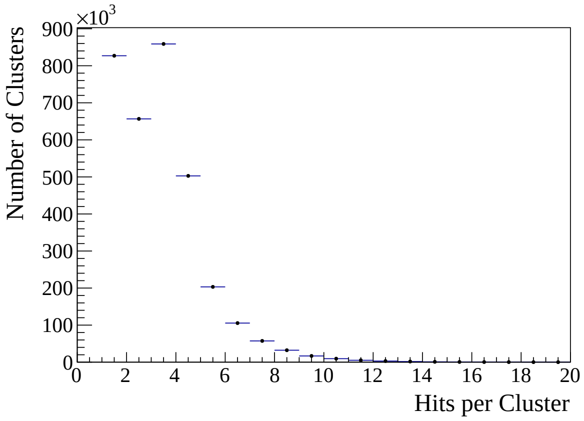

(a) *November 2017 beam test*

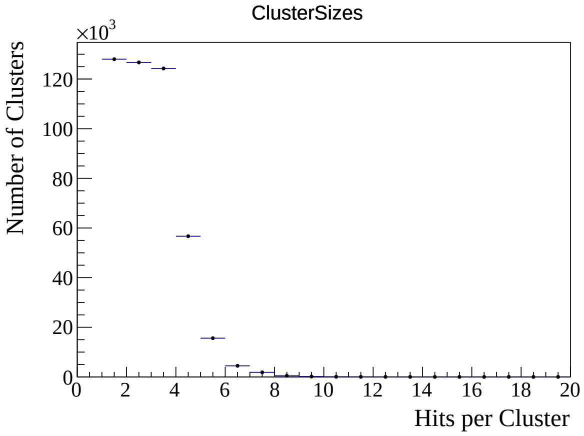

(b) *June 2018 beam test*

Figure 9.12 *The number of hits in each cluster from the November 2017 data (top) and June 2018 data (bottom).*

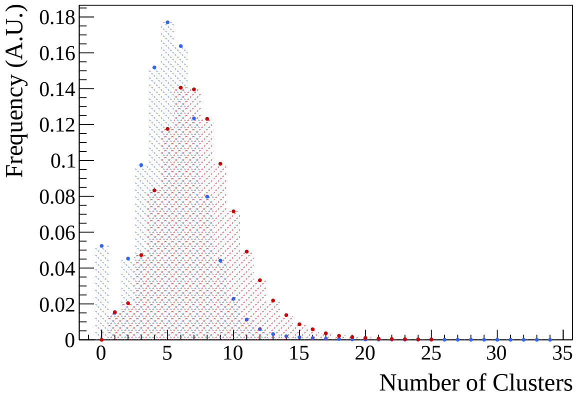

(a) *November 2017 beam test*

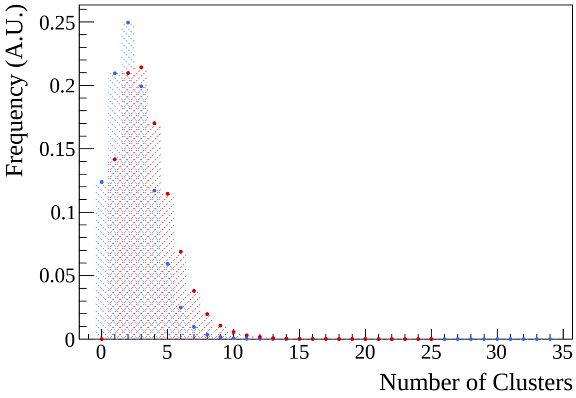

(b) *June 2018 beam test*

Figure 9.13 *Number of observed photons per event from data including (red) or excluding (blue) clusters composed of one hit using data from the beam tests in November 2017 (top) and June 2018 (bottom).*

analysis. The ratio between the histogram mean including and excluding clusters of size one is comparable between the two data sets.

As a cross-check, the photon yield is calculated per MCP-PMT column. Naively one would expect roughly the same amount of photons in each column, which added together amounts to the total number of photons seen per event. Figure 9.14 shows the distributions of the photon yield as separated by column. The plot shown in red, corresponds to x-coordinate 1 in Fig. 9.1(a) and has a mean of 1.78. The two middle columns, labelled as the green (x-pixel 2) and magenta (x-pixel 3) histograms, have means of 2.05 and 1.47 respectively. The last column (blue, x-coordinate 4) has a mean of 1.85. The errors on the average number of photons per column are negligible. The observed number of photons per column is consistent and accumulate to the number seen in the blue curve

Table 9.2 *Average number of photons seen in Fig. 9.13 using test beam data, where clusters made up of one hit are included or excluded*

	With clusters of size 1	Without clusters of size 1
November 2017	7.36 ± 0.00	5.35 ± 0.00
June 2018	3.53 ± 0.01	2.35 ± 0.00

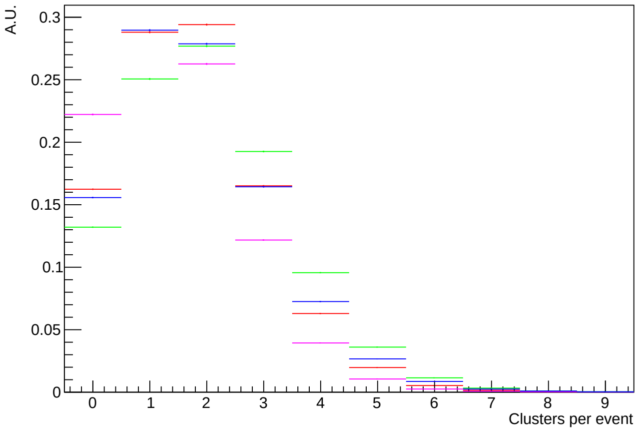

Figure 9.14 *The photon yield per MCP-PMT column using the data from the November 2017 beam test. The first column is shown by the red histogram, the middle columns are given in green and magenta, respectively. The final column is given by the blue histogram.*

in Fig. 9.13. The slightly lower number of photons captured by the column with x-coordinate 3 can be explained by the slightly lower light yield of this column, as can be seen by eye in the hitmap of Fig. 9.1(a).

9.3 Results

Figure 9.15 shows the comparison between data and simulation using the data taken in the November 2017 beam test. The data have been clustered and the decision was made to include the clusters of size one. Although this may slightly overestimate the number of photons seen per event, we expect to see photon hits which only illuminate one pixel and these need to be included. For the November 2017 data analysis, the QE of the MCP-PMT used in the November beam test was measured after the beam test. This quantitative efficiency has been applied to the simulated data. As shown in Fig. 8.5, a large degradation of the QE of the MCP-PMT used in this beam test was noticed. The lower QE measured post

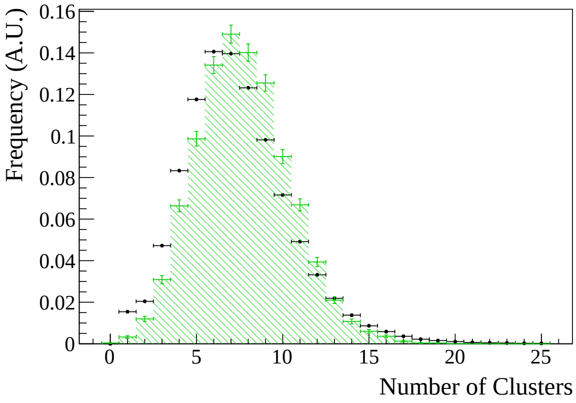

(a) *November 2017 beam test*

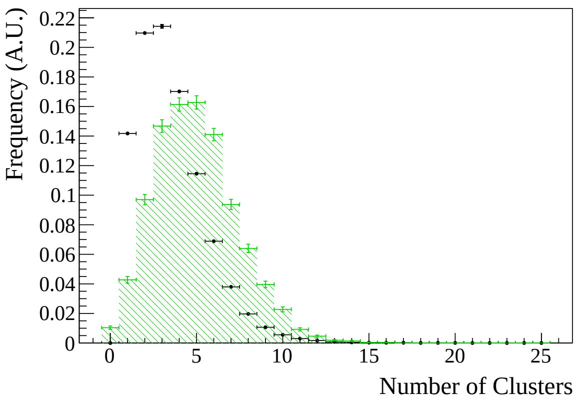

(b) *June 2018 beam test*

Figure 9.15 *Number of photons observed per event in data (black points) and simulation (green shaded histogram) using the data obtained in the November 2017 beam test (top) and June 2018 beam test (bottom).*

beam test is applied to the simulated data for the June 2018 data analysis. The clustering algorithm has been applied to the simulation for both analyses. The results for both beam test campaigns are shown in Fig. 9.15, and the numerical comparison is given in Tab. 9.3.

Fig 9.15 and Tab. 9.3 show a good agreement between data and simulation for the November 2017 beam test, where the ratio between data and simulation is 0.96. The June 2018 analysis has a discrepancy between data and simulation, as 29% fewer photons are seen in data compared to simulation.

It has to be noted that the TORCH project is in its development stage, and there are many factors which may not be fully understood. For example, the collection efficiency of the MCP-PMTs is not known, as was outlined earlier in this

Table 9.3 *Average photon yield, along with the ratio of data compared to simulation.*

	Simulation	Data	Ratio
November 2017	7.69 ± 0.03	7.36 ± 0.00	0.96
June 2018	4.94 ± 0.03	3.53 ± 0.01	0.71

chapter. It may differ greatly from tube to tube [81], such that a time-consuming measurement for each tube would be required to accurately analyse the data. In addition, we do not know how the glue transmission curve changes over time, as no ageing tests on the glue used have been performed. Furthermore, the photon yields depend strongly on the MCP-PMT gains and the NINO thresholds, for which the estimated values were used in the simulated data. Other unknown factors include the mirror reflectivity, the uniformity of the QE across the MCP-PMT, and the uniformity of the gain of a MCP-PMT. To summarise these unknown factors, the MCP-PMTs and the electronics used for the read out of the data are being developed simultaneously with the detector prototypes. This makes it very difficult to track down any inconsistencies in the factors contributing to the photon loss. Nevertheless, the photon yield of the November 2017 MCP-PMT shows great agreement between data and simulation.

9.3.1 Lower photon yield in June 2018 data

A significantly lower number of photons was observed in the June 2018 data. This can be attributed to the lower QE of the MCP-PMT used in this beam test. Figure 9.16 shows the number of photons captured per particle from simulated data. The only difference between the curves is the quantum efficiency that has been applied. The magenta curve shows the expected number of photons with the QE of the November beam test MCP-PMT, which has a mean of 7.84 ± 0.03. The green and red curves show the expected number of photons where the QE pre and post June beam test has been applied, respectively. The pre beam test QE mean is 5.59 ± 0.03, and where the QE that was measured post beam test has been applied, the mean is 4.67 ± 0.02. Using these averages, a scaling factor to quantify the difference between the curves can be calculated. The curve generated using the pre June beam test QE is 0.71 times smaller than that generated using the November beam test QE. Similarly, the difference between the post June beam test QE and the November result is 0.60.

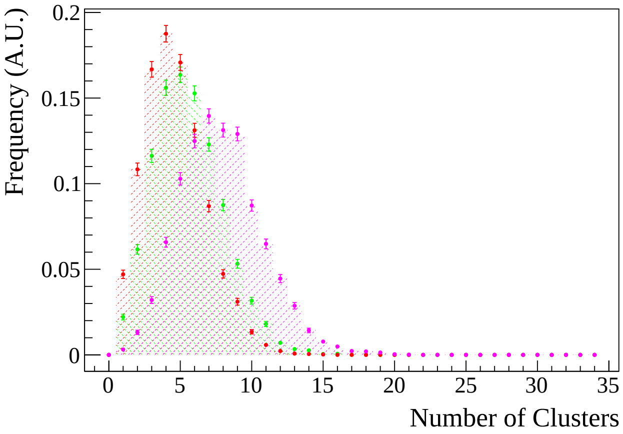

Figure 9.16 *The effect of the QE on the photon yield is shown using simulated data. The magenta curve shows the expected number of photons with the QE of the November beam test MCP-PMT. The green and red curves show the expected number of photons where the QE pre and post June beam test has been applied, respectively.*

The analysis of the June 2018 test beam data has been performed using the QE measured after the beam test. Figure 9.17 shows a comparison between the number of photons seen in data in November where the QE of the November 2017 tube is applied with the same curve scaled down by 0.60, as this was found to be the difference in photon yield generated by the difference in QE between the two MCP-PMTs. The mean of the photon yield curve generated using June 2018 beam test data is 3.53 and the scaled down histogram of the November 2017 beam test has a mean of 4.42. Therefore we can conclude that the difference in photon yield observed in data between the two beam test campaigns can mostly be attributed to using MCP-PMTs with different QEs.

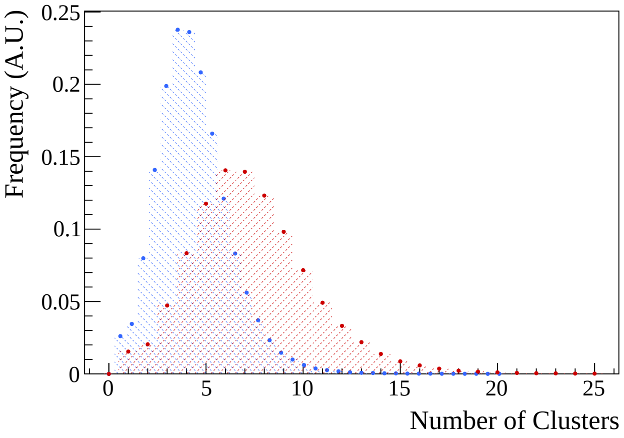

Figure 9.17 *The November 2017 beam test data photon yield curve (red) is scaled down relative to the difference generated by using MCP-PMTs with different QEs (blue).*

Chapter 10

Conclusion and outlook

This research presented in this thesis focuses on two separate subjects; the search for exited $\mathit{\Xi}_c^0$ states decaying to $\mathit{\Lambda}_c^+ K^-$, and detector development of the TORCH time-of-flight detector.

Three new $\mathit{\Xi}_c^0$ baryons are discovered in their decay to a $\mathit{\Lambda}_c^+$ baryon and a K^- meson, the $\Xi_c(2923)^0$, the $\Xi_c(2939)^0$ and the $\Xi_c(2965)^0$. Their masses and natural widths are measured to be

$$m(\Xi_c(2923)^0) = 2923.04 \pm 0.25\,(\text{stat}) \pm 0.20\,(\text{syst}) \pm 0.14(\text{PDG})\ \text{MeV},$$
$$\Gamma(\Xi_c(2923)^0) = 7.09 \pm 0.79\,(\text{stat}) \pm 1.84\,(\text{syst})\ \text{MeV},$$

$$m(\Xi_c(2939)^0) = 2938.55 \pm 0.21\,(\text{stat}) \pm 0.17\,(\text{syst}) \pm 0.14(\text{PDG})\ \text{MeV},$$
$$\Gamma(\Xi_c(2939)^0) = 10.22 \pm 0.77\,(\text{stat}) \pm 1.07\,(\text{syst})\ \text{MeV},$$

$$m(\Xi_c(2965)^0) = 2964.88 \pm 0.26\,(\text{stat}) \pm 0.14\,(\text{syst}) \pm 0.14(\text{PDG})\ \text{MeV},$$
$$\Gamma(\Xi_c(2965)^0) = 14.07 \pm 0.91\,(\text{stat}) \pm 1.34\,(\text{syst})\ \text{MeV},$$

where the first error is statistical, the second is systematic and the third error in the mass measurements is due to the uncertainty in the $\mathit{\Lambda}_c^+$ mass measurement [6].

These results can aid in the understanding of HQET, and as such could lead to further theoretical predictions or experimental discoveries of excited baryons. The b-factories, Belle and Babar may look for these states as a confirmation of their existence. Furthermore, spin measurements of the new states are essential analyses to be performed in the future. Additionally, these states can be searched for in other decay modes.

Secondly, this thesis describes the status of the research and development of the TORCH time-of-flight detector. The studies in this thesis outline the laboratory testing of the MCP-PMT's used in the project, where the quantum efficiency and point spread function measurements are explained. Results from several beam test campaigns, detailed in a recent paper [1], are described. An agreement between data and simulation within $\sim 5\%(30\%)$ is found for the 4×64 (8×64) MCP-PMT used in the November 2017 (June 2018) beam test, respectively.

Currently, no data are being taken at the LHC as many detector upgrades are being performed, which is why no more beam test campaigns have been initiated. Nevertheless, the data from the beam test completed in June 2018 with proto-TORCH are being analysed. Furthermore, the TORCH detector is being integrated in LHCb simulation, allowing for further studies regarding the improved physics performance of the detector [83]. Details of the current status of the TORCH project can be found in recent conference proceedings [84], [85].

Appendix A

Vetoing the D meson decay backgrounds

It was checked whether the overshoot at low mass in the Λ_c^+ sideband sample in the ΔM invariant mass spectrum can be attributed to an excess of D meson background decays, which are described in Sec. 5.7. These contributions are fully removed in both the Λ_c^+ signal and Λ_c^+ sideband sample. The candidates are required to have a $m(\pi^+K^-K^+)$ invariant mass less than 1850 MeV and higher than 1890 MeV. In addition, the $m(\pi^+\pi^+K^-)$ mass has to be smaller than 1860 MeV, between 1880 and 1950 MeV or larger than 1990 MeV. These cuts result in a low signal efficiency and thus have not been implemented on the main analysis.

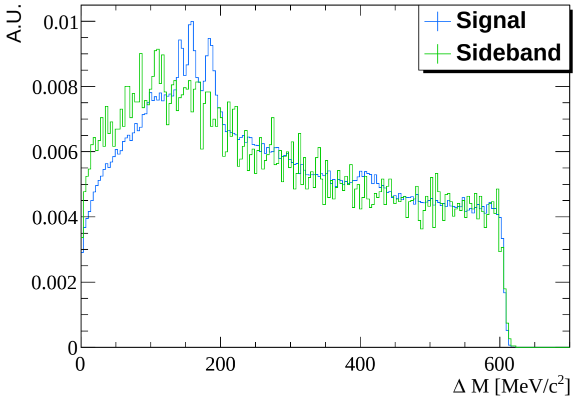

Figure A.1 *The ΔM mass spectrum for the signal region (blue) and Λ_c^+ sideband region (green).*

The comparison between the ΔM distributions is shown in Fig. A.1. A clear overshoot of events can be seen at low masses between $0\,\mathrm{MeV} < \Delta M < 100\,\mathrm{MeV}$, indicating that this overshoot cannot be explained by the D meson background decays.

Appendix B

Clebsch Gordan coefficients

We want to check whether either of the decays $\Xi_c^{**+} \to \Sigma_c^{++} K^-$ and $\Xi_c^{**0} \to \Sigma_c^{+} K^-$ suffer a suppression in branching ratio due to the isospin. This can be done using the Clebsch-Gordon coefficients, which are looked up in Tables provided by the Particle Data Group (PDG) [6]. The decays along with the isospin, I, as well as the third component of the isospin, I_3 for each of the particles is given in Fig. B.1. One can easily see that I_3 is a conserved quantity, and it is given by

$$I_3 = \frac{1}{2}(n_u - n_d), \tag{B.1}$$

where n_u is the number of up quarks and n_d is the number of down quarks. All other quark flavours are assigned a value of $I_3 = 0$.

Considering the decays of interest in this derivation, the daughter particles have isospin $I = 1$ and $I = \frac{1}{2}$. Hence we want to consider the Clebsch-Gordan coefficient table corresponding to the $1 \times \frac{1}{2}$ configuration, as shown in Fig. B.2. The notation is the table refers to angular momentum, however this can easily be extended to isospin. Doing this, we substitute J with I, the isospin of the parent particle, and M with I_3 of the parent particle. Similarly, m_1 and m_2 are the I_3 of the daughter particles.

Using the table, we read that:

$$|\frac{1}{2}, +\frac{1}{2}\rangle = \sqrt{\frac{2}{3}}| +1, -\frac{1}{2}\rangle - \sqrt{\frac{1}{3}}|0, +\frac{1}{2}\rangle, \tag{B.2}$$

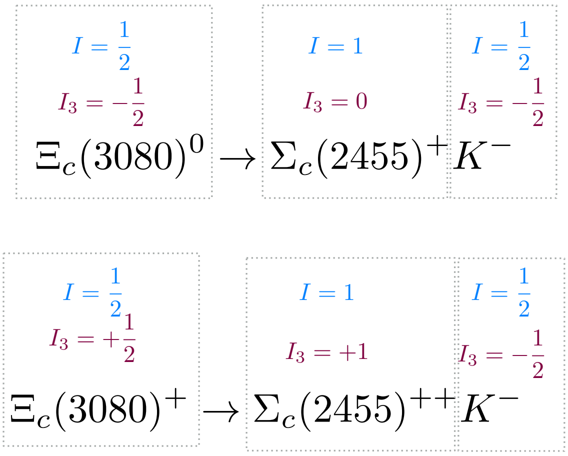

Figure B.1 *The decays along with the isospin, I, in blue, as well as the third component of the isospin, I_3, in maroon for each of the particles.*

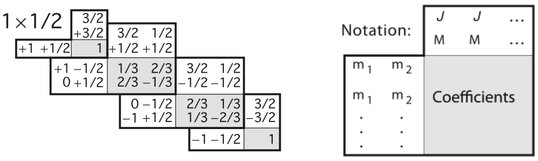

Figure B.2 *The Clebsch-Gordan coefficients for $1 \times \frac{1}{2}$. Note that a square-root sign is to be understood over every coefficient which are given in the shaded boxes. The minus sign is excluded from the square-root. Figure taken from [6].*

and

$$|\frac{1}{2}, -\frac{1}{2}\rangle = \sqrt{\frac{1}{3}}|0, -\frac{1}{2}\rangle - \sqrt{\frac{2}{3}}|-1, +\frac{1}{2}\rangle. \tag{B.3}$$

In each of these expansions, the decays we are considering correspond to the first term, since those number correspond to the I_3 of the daughter particles. The coefficient in front of the $\Xi_c^{**+} \rightarrow \Sigma_c^{++} K^-$ expansion is double that of the $\Xi_c^{**0} \rightarrow \Sigma_c^{+} K^-$ decay. Hence, using the Clebsch-Gordan coefficients, we expect the yield of the $\Xi_c^{**+} \rightarrow \Sigma_c^{++} K^-$ decay to be twice as large as the $\Xi_c^{**0} \rightarrow \Sigma_c^{+} K^-$ decay (assuming identical production rates).

Appendix C

CP violation in $B_s^0 \to \phi\phi$ and the search for $B^0 \to \phi\phi$ decay.

In addition to the work presented in the main body of this thesis, I performed part of the analysis of CP violation in $B_s^0 \to \phi\phi$ decays and the search for the $B^0 \to \phi\phi$ decay, where $\phi \to K^-K^+$. The analysis is performed on pp collision data corresponding to an integrated luminosity of $5.0\,\mathrm{fb}^{-1}$, collected with the LHCb experiment at centre-of-mass energies $\sqrt{s} = 7$ TeV in 2011, 8 TeV in 2012, and 13 TeV from 2015 to 2016. This work was published in reference [2]. In this appendix a summary is presented.

The time-dependent angular analysis of the $B_s^0 \to \phi\phi$ candidates to extract the CP-violating phase $\phi_s^{\bar{s}s\bar{s}}$, as well as the time-integrated triple-product asymmetries were performed by other members of the analysis group, and will not be discussed here. Described in this appendix are the event selection for the $B_s^0 \to \phi\phi$ and the $B^0 \to \phi\phi$ candidates, as well as the search for the $B^0 \to \phi\phi$ branching ratio.

The $B^0 \to \phi\phi$ decay has not been observed so far. In the SM, this decay is heavily suppressed by the OZI rule. This rule was formulated independently by S. Okubo [86], G. Zweig [87] and J. Iizuka [88] and explains why certain decay modes are suppressed as a consequence of QCD. According to the OZI rule, any particle decay occurring through the strong force will be suppressed if the Feynman diagram can be divided into two separate diagrams by removing the internal gluon lines, where one diagram comprises all initial-state particles and the final-state particles make up the second diagram. The expected branching fraction of the decay, based on theoretical predictions is in the range (0.1 −

$3.0) \times 10^{-8}$ [89–92]. Certain beyond the SM models allow for a higher branching fraction, up to 10^{-7} [90].

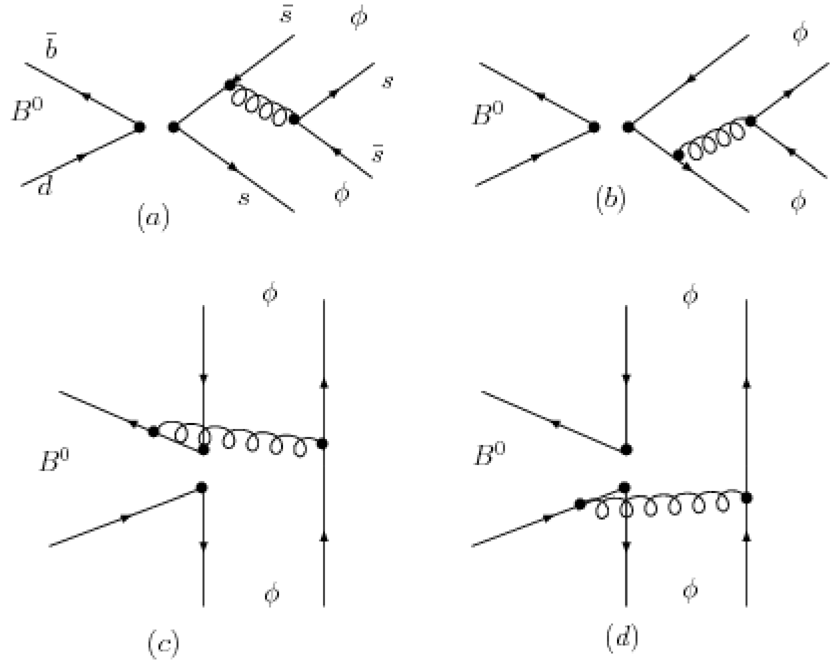

Figure C.1 *Leading order Feynman diagrams for the decay $B^0 \to \phi\phi$ [89].*

The event selection uses the LHCb HLT trigger to select signal candidates, where selection requirements are based on the fit quality of the four-kaon vertex and the χ^2_{IP} of the tracks. Furthermore, the p_{T} of the particles is considered, and the reconstructed K^+K^- mass is required to be within 25 MeV from the ϕ mass. Several loose pre-selection requirements are implemented. Examples of observables used are the decay time of the B meson as well as the $m(K^+K^-)$ invariant mass to selected ϕ candidates. A multi-variate selection is performed using the TMVA toolkit [53]. The variables using in the multi-variate selection are the p_{T} and pseudorapidity, η, of the B_s^0 candidate, each ϕ candidate and the kaon tracks. The cosine of the direction angle is also used, along with the maximum track χ^2. For the time-dependent analysis of $B_s^0 \to \phi\phi$ candidates, the optimal selection criterion on the multi-variate BDT variable is optimised using $S/\sqrt{S+B}$ as FoM. The search for the $B^0 \to \phi\phi$ decay uses the same multivariate selection, but with a more stringent selection requirement, calculated using the Punzi FoM [56]. Furthermore, a veto is employed to reduce the $B^0 \to \phi K^*$ decay background.

The invariant mass $m(K^+K^-K^+K^-)$ for the selected data is shown in Fig. C.2. The full Run 1 and 2015 and 2016 data samples are used. A fit is superimposed. The red dashed peak shows the $B_s^0 \to \phi\phi$ events, and it consists of a Gaussian function and a Student-T function added together with a shared mean. The magenta, long-dashed contribution shows a $\Lambda_b \to \phi p K$ reflection, where the yield has been fixed. The green contribution gives the $B^0 \to \phi\phi$ candidates. The $B^0 \to \phi\phi$ peak consists of a Student-T function and a Crystal Ball function added together, where all parameters except the mean and widths are fixed to the B_s^0 peak values. The B^0 mass is fixed with respect to the fitted B_s^0 mass such that $M_{B_s^0} - M_{B^0} = 87.2$ MeV. Furthermore, the resolution of the B^0 curve components are fixed to the values obtained through B_s^0 simulated data, up to a scaling factor :

$$\alpha = \frac{M_{B^0} - 4M_K}{M_{B_s^0} - 4M_K} = 0.97, \tag{C.1}$$

where M_K is the kaon mass. A total of 4453 ± 69 events of $B_s^0 \to \phi\phi$ is observed, along with a $B^0 \to \phi\phi$ signal yield of 0.5 ± 9.2 events. The data is consistent with no significant $B^0 \to \phi\phi$ contribution.

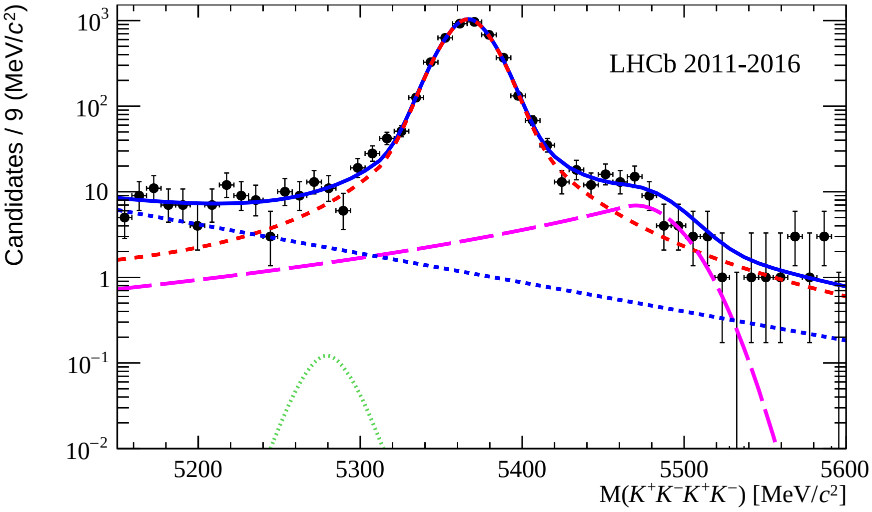

Figure C.2 *The $m(K^-K^+K^-K^+)$ invariant mass is shown, with a fit superimposed. The total PDF as described in the text is shown as a blue solid line, $B_s^0 \to \phi\phi$ as a red dashed line, $B^0 \to \phi\phi$ as a green dotted line, the $\Lambda_b \to \phi p K$ reflection as a magenta long-dashed line and the combinatorial background as a blue short-dashed line.*

The CL_s method is used to set an improved limit on the highly suppressed $B^0 \to \phi\phi$ decay. The CLs method dates back to the initial Higgs searches at the LEP [93]. The method utilises a test statistic scanned across multiple toy distributions. Toy distributions are used due to the low statistics available for this analysis. Based on a fit to the data, toy models are generated. This is done for multiple hypotheses where the number of $B^0 \to \phi\phi$ events is scanned. The test statistic used is defined as

$$t = -2log\left(\frac{\mathcal{L}(f_{s+b}(x))}{\mathcal{L}(f_b(x))}\right), \tag{C.2}$$

where $\mathcal{L}(f_{s+b}(x))$ is the likelihood of the signal plus background PDF, f_{s+b}, and $\mathcal{L}(f_b(x))$ is the likelihood calculated from the background only PDF, f_b. The set of parameters required by the PDF are represented by x, and t_{obs} is defined as the value of the test statistic observed in the data. The method compares a distribution without a signal to another distribution where we test a given hypothesis based on a toy model for that hypothesis. Using these model we can quantify which model is more likely to occur. With this method, the ratio of the p-value of the signal plus background hypothesis and the background only hypothesis the CLs variable is determined using Equation C.3:

$$CL_s = \frac{CL_{s+b}}{CL_b} \tag{C.3}$$

CL_{s+b} is the p-value of the signal plus background hypothesis and it is defined as $CL_{s+b} = \int_{t_{obs}}^{\infty} g(t; s+b)dt$ and CL_b is found using $1 - CL_b = \int_{-\infty}^{t_{obs}} g(t; b)dt$. The functions $g(t; s+b)$ and $g(t; b)$ are test statistic distributions and are generated for different values of the signal yield, using 10,000 toys for f_{s+b} and f_b each. For each generated set of toys, the value of CL_s is determined from Eq. C.3 using the method outlined above.

The branching fraction is calculated using the Eq. C.4.

$$\mathcal{B}(B^0 \to \phi\phi) = N_{B^0_d} \times \frac{\mathcal{B}(B^0_s \to \phi\phi) \times f_s/f_d}{N_{B^0_s \to \phi\phi}} \tag{C.4}$$

$N_{B^0_d}$ is the limit on the $B^0 \to \phi\phi$ yield, and $N_{B^0_s \to \phi\phi}$ is the number of B^0_s candidates in the fit shown in Fig. C.2. The fragmentation ratio, $f_s/f_d = 0.259$ account for the difference in production of B^0 mesons compared to B^0_s mesons. The fragmentation fraction and the $\mathcal{B}(B^0_s \to \phi\phi) = 1.84 \pm 0.05(\text{stat}) \pm 0.07(\text{syst}) \pm 0.11(f_s/f_d) \pm 0.12(\text{norm}) \times 10^{-5}$ branching fraction are external inputs taken from [94] and [95], respectively. The uncertainties on the $B^0_s \to \phi\phi$ branching fraction are propagated, where the f_s/f_d component is ignored to avoid double counting this error.

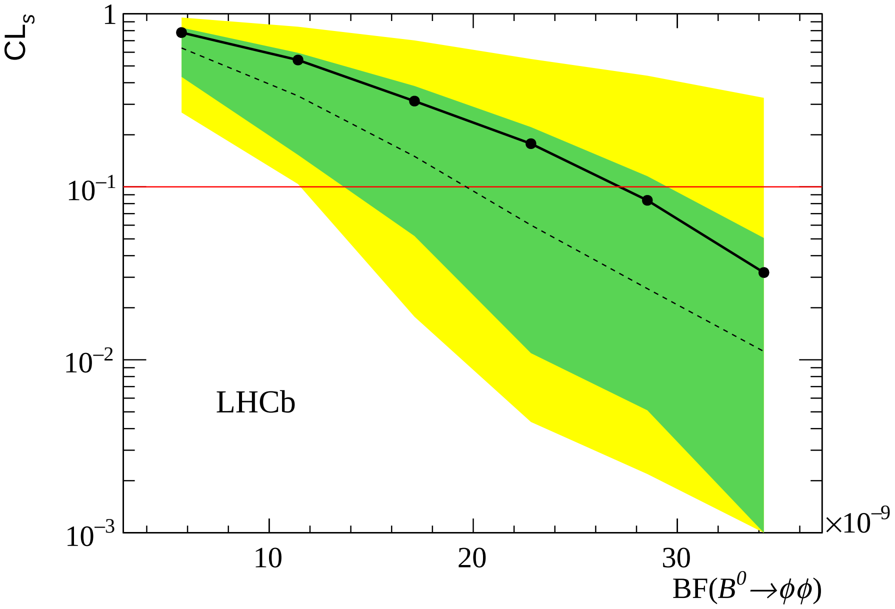

Figure C.3 *Results of the* CL_s *scan as a function of* $N_{B_d^0}$*. The solid black line shows the observed* CL_s *distribution, while the dotted black line indicates the expected distribution. The green (yellow) band marks the* 1σ *(*2σ*) confidence region on the expected* CL_s*.*

An earlier paper searched for $B^0 \to \phi\phi$ using only the Run 1 data set [95] and obtained a limit on the branching fraction of 2.8×10^{-8} at 90 % confidence level. The updated limit from this measurement is calculated to be

$$\mathcal{B}(B^0 \to \phi\phi) < 2.7\,(3.0) \times 10^{-8}\,\text{at}\,90\,\%\,(95\,\%)\,\text{CL},$$

and it supersedes the previous best limit.

The improvement on the branching fraction limit is less than naively expected compared to the previous analysis [95]. This could be due to two reasons. Firstly, the limits are close to the upper range of the theoretical predictions and it is possible that a small signal is observed. Secondly, the amount of background events per bin in this analysis is larger than in the prervious analysis, which may suppress the sensitivity of this measurement.

Bibliography

[1] S. Bhasin et al. Test-beam studies of a small-scale TORCH time-of-flight demonstrator. 2020.

[2] R. Aaij et al. Measurement of *CP* violation in the $B_s^0 \to \phi\phi$ decay and search for the $B^0 \to \phi\phi$ decay. *JHEP*, 12:155, 2019.

[3] R. Aaij et al. Observation of $J/\psi p$ resonances consistent with pentaquark states in $\Lambda_b^0 \to J/\psi p K^-$ decays. *Phys. Rev. Lett.*, 115:072001, 2015.

[4] R. Aaij et al. Test of lepton universality with $B^0 \to K^{*0}\ell^+\ell^-$ decays. *JHEP*, 08:055, 2017.

[5] R. Aaij et al. Search for lepton-universality violation in $B^+ \to K^+\ell^+\ell^-$ decays. *Phys. Rev. Lett.*, 122:191801, 2019.

[6] M. Tanabashi et al. Review of particle physics. *Phys. Rev.*, D98:030001, 2018.

[7] Robert B. Mann. *An introduction to particle physics and the standard model.* CRC Press, Boca Raton, FL, 2010.

[8] M. Tanabashi et al. Review of particle physics. *Phys. Rev. D*, 98:030001, Aug 2018.

[9] W. Roberts and Muslema Pervin. Heavy baryons in a quark model. *International Journal of Modern Physics A*, 23(19):2817–2860, 2008.

[10] Hua-Xing Chen et al. p-wave charmed baryons from qcd sum rules. *Phys. Rev. D*, 91:054034, Mar 2015.

[11] M. Padmanath et al. Excited-state spectroscopy of singly, doubly and triply-charmed baryons from lattice QCD. In *Proceedings, 6th International Workshop on Charm Physics (Charm 2013): Manchester, UK, August 31-September 4, 2013*, 2013.

[12] O. S. Brüning et al. *LHC Design Report.* CERN Yellow Reports: Monographs. CERN, Geneva, 2004.

[13] *LEP Design Report: Vol.2. The LEP Main Ring.* CERN, Geneva, 1984.

[14] E. Mobs. The CERN accelerator complex - August 2018. Complexe des accélérateurs du CERN - Aot 2018. Aug 2018. General Photo.

[15] N Abgrall et al. NA61/SHINE facility at the CERN SPS: beams and detector system. *Journal of Instrumentation*, 9(06):P06005–P06005, jun 2014.

[16] E. C. Gil et al. The beam and detector of the NA62 experiment at CERN. *Journal of Instrumentation*, 12(05):P05025–P05025, may 2017.

[17] P. Abbon et al. The compass experiment at cern. *Nuclear Instruments and Methods in Physics Research Section A: Accelerators, Spectrometers, Detectors and Associated Equipment*, 577(3):455 – 518, 2007.

[18] E. Gschwendtner et al. Awake, the advanced proton driven plasma wakefield acceleration experiment at cern. *Nuclear Instruments and Methods in Physics Research Section A: Accelerators, Spectrometers, Detectors and Associated Equipment*, 829:76 – 82, 2016. 2nd European Advanced Accelerator Concepts Workshop - EAAC 2015.

[19] S. Chatrchyan et al. The CMS Experiment at the CERN LHC. *JINST*, 3:S08004, 2008.

[20] G. Aad et al. The ATLAS Experiment at the CERN Large Hadron Collider. *JINST*, 3:S08003, 2008.

[21] The ALICE Collaboration, K. Aamodt, et al. The ALICE experiment at the CERN LHC. *Journal of Instrumentation*, 3(08):S08002–S08002, aug 2008.

[22] G. Anelli et al. The TOTEM experiment at the CERN Large Hadron Collider. *JINST*, 3:S08007, 2008.

[23] O. Adriani et al. The LHCf detector at the CERN Large Hadron Collider. *JINST*, 3:S08006, 2008.

[24] A. Mitsou Vasiliki et al. The MoEDAL experiment at the LHC: status and results. *Journal of Physics: Conference Series*, 873:012010, jul 2017.

[25] A Augusto Alves et al. The LHCb Detector at the LHC. *JINST*, 3(LHCb-DP-2008-001. CERN-LHCb-DP-2008-001):S08005, 2008. Also published by CERN Geneva in 2010.

[26] R Aaij et al. Performance of the lhcb vertex locator. *Journal of Instrumentation*, 9(09):P09007P09007, Sep 2014.

[27] Lhcb detector performance. *International Journal of Modern Physics A*, 30(07):1530022, 2015.

[28] *Journal of Instrumentation*, 9(01):P01002P01002, Jan 2014.

[29] Murdo Thomas Traill. Searches for Doubly Charmed Baryons at LHCb, 2019. Presented 17 Sep 2019.

[30] R. Aaij et al. Design and performance of the LHCb trigger and full real-time reconstruction in Run 2 of the LHC. *JINST*, 14(04):P04013, 2019.

[31] R. Aaij et al. Observation of five new narrow $\varOmega_c^0$ states decaying to $\varXi_c^+ K^-$. *Phys. Rev. Lett.*, 118:182001, 2017.

[32] G. Chiladze and A. F. Falk. Phenomenology of new baryons with charm and strangeness. *Phys. Rev.*, D56:R6738–R6741, 1997.

[33] M. Karliner and J. L. Rosner. Very narrow excited Ω_c baryons. *Phys. Rev.*, D95(11):114012, 2017.

[34] B. Aubert et al. Study of $\overline{B} \to \Xi_c \overline{\Lambda}_c^-$ and $\overline{B} \to \Lambda_c^+ \overline{\Lambda}_c^- \overline{K}$ decays at babar. *Phys. Rev. D*, 77:031101, Feb 2008.

[35] B. Aubert et al. Study of excited charm-strange baryons with evidence for new baryons $\Xi_c(3055)^+$ and $\Xi_c(3123)^+$. *Phys. Rev. D*, 77:012002, Jan 2008.

[36] Y. B. Li et al. Evidence of a structure in $\bar{K}^0 \Lambda_c^+$ consistent with a charged $\Xi_c(2930)^+$, and updated measurement of $\bar{B}^0 \to \bar{K}^0 \Lambda_c^+ \bar{\Lambda}_c^-$ at Belle. *Eur. Phys. J.*, C78(11):928, 2018.

[37] Y. B. Li et al. Observation of $\Xi_c(2930)^0$ and updated measurement of $B^- \to K^- \Lambda_c^+ \bar{\Lambda}_c^-$ at belle. *The European Physical Journal C*, 78(3):252, Mar 2018.

[38] Y. Kato et al. Studies of charmed strange baryons in the ΛD final state at belle. *Phys. Rev. D*, 94:032002, Aug 2016.

[39] R. Chistov et al. Observation of new states decaying into $\Lambda_c^+ K^- \pi^+$ and $\Lambda_c^+ K_S^0 \pi^-$. *Phys. Rev. Lett.*, 97:162001, Oct 2006.

[40] B. Aubert et al. Study of excited charm-strange baryons with evidence for new baryons $\Xi_c(3055)^+$ and $\Xi_c(3123)^+$. *Phys. Rev. D*, 77:012002, Jan 2008.

[41] T. Lesiak et al. Measurement of masses of the $\Xi_c(2645)$ and $\Xi_c(2815)$ baryons and observation of $\Xi_c(2980) \to \Xi_c(2645)\pi$. *Physics Letters B*, 665(1):9 – 15, 2008.

[42] J. Yelton et al. Study of excited Ξ_c states decaying into Ξ_c^0 and Ξ_c^+ baryons. *Phys. Rev. D*, 94:052011, Sep 2016.

[43] M. Gell-Mann. The eightfold way: A theory of strong interaction symmetry. 3 1961.

[44] Susumu Okubo. Note on unitary symmetry in strong interactions. *Prog. Theor. Phys.*, 27:949–966, 1962.

[45] Torbjorn Sjostrand, Stephen Mrenna, and Peter Z. Skands. A Brief Introduction to PYTHIA 8.1. *Comput. Phys. Commun.*, 178:852–867, 2008.

[46] David J. Lange. The evtgen particle decay simulation package. *Nuclear Instruments and Methods in Physics Research Section A: Accelerators, Spectrometers, Detectors and Associated Equipment*, 462(1):152 – 155, 2001. BEAUTY2000, Proceedings of the 7th Int. Conf. on B-Physics at Hadron Machines.

[47] S. Agostinelli et al. Geant4a simulation toolkit. *Nuclear Instruments and Methods in Physics Research Section A: Accelerators, Spectrometers, Detectors and Associated Equipment*, 506(3):250 – 303, 2003.

[48] R. Aaij et al. A comprehensive real-time analysis model at the LHCb experiment. *JINST*, 14(arXiv:1903.01360. 04):P04006. 15 p, Mar 2019.

[49] Wouter D. Hulsbergen. Decay chain fitting with a Kalman filter. *Nucl. Instrum. Meth.*, A552:566–575, 2005.

[50] R Aaij et al. Precision measurement of D meson mass differences. *JHEP*, 06:065, 2013.

[51] R. Aaij et al. Measurement of b-hadron masses. *Phys. Lett.*, B708:241, 2012.

[52] Crystal ball function. `https://en.wikipedia.org/wiki/Crystal_Ball_function`. Accessed: 2019-10-09.

[53] Andreas Hoecker et al. TMVA 4 — Toolkit for Multivariate Data Analysis with ROOT. Users Guide. 2009.

[54] R. Brun and F. Rademakers. Root an object oriented data analysis framework. *Nuclear Instruments and Methods in Physics Research Section A: Accelerators, Spectrometers, Detectors and Associated Equipment*, 389(1):81 – 86, 1997. New Computing Techniques in Physics Research V.

[55] M. Pivk and F.R. Le Diberder. : A statistical tool to unfold data distributions. *Nuclear Instruments and Methods in Physics Research Section A: Accelerators, Spectrometers, Detectors and Associated Equipment*, 555(1-2):356369, Dec 2005.

[56] G. Punzi. Sensitivity of searches for new signals and its optimization. *eConf*, C030908:MODT002, 2003.

[57] G.A. Cowan, D.C. Craik, and M.D. Needham. Rapidsim: An application for the fast simulation of heavy-quark hadron decays. *Computer Physics Communications*, 214:239 – 246, 2017.

[58] Rene Brun and Fons Rademakers. Root an object oriented data analysis framework. *Nuclear Instruments and Methods in Physics Research Section A: Accelerators, Spectrometers, Detectors and Associated Equipment*, 389(1):81 – 86, 1997. New Computing Techniques in Physics Research V.

[59] Matteo Cacciari, Mario Greco, and Paolo Nason. The pt spectrum in heavy-flavour hadroproduction. *Journal of High Energy Physics*, 1998(05):007007, May 1998.

[60] R Aaij et al. Study of D_J meson decays to $D^+\pi^-$, $D^0\pi^+$ and $D^{*+}\pi^-$ final states in pp collision. *JHEP*, 09:145, 2013.

[61] R. Aaij et al. Precise measurements of the properties of the $B_1(5721)^{0,+}$ and $B_2^*(5747)^{0,+}$ states and observation of $B^{+,0}\pi^{-,+}$ mass structures. *JHEP*, 04:024, 2015.

[62] M. Mikhasenko et al. Dalitz-plot decomposition for three-body decays. 2019.

[63] R. Aaij et al. Precision measurement of D meson mass differences. *JHEP*, 06:065, 2013.

[64] R. Aaij et al. Precision measurement of the mass and lifetime of the Ξ_b^- baryon. *Phys. Rev. Lett.*, 113:242002, 2014.

[65] P. A. Cherenkov. Visible emission of clean liquids by action of γ radiation. *Doklady Akademii Nauk SSSR*, 2:451, 1934.

[66] I. M. Frank and I. E. Tamm. Coherent visible radiation of fast electrons passing through matter. *Compt. Rend. Acad. Sci. URSS*, 14(3):109–114, 1937. [Usp. Fiz. Nauk93,no.2,388(1967)].

[67] L. Castillo Garca. Testing micro-channel plate detectors for the particle identification upgrade of lhcb. *Nuclear Instruments and Methods in Physics Research Section A: Accelerators, Spectrometers, Detectors and Associated Equipment*, 695:398 – 402, 2012. New Developments in Photodetection NDIP11.

[68] I. Adam et al. The DIRC particle identification system for the BaBar experiment. *Nucl. Instrum. Meth.*, A538:281–357, 2005.

[69] Belle ii technical design report. 2010.

[70] N. Harnew, N. Brook, L. [Castillo Garca], D. Cussans, K. Fhl, R. Forty, C. Frei, R. Gao, T. Gys, D. Piedigrossi, J. Rademacker, A. [Ros Garcia], and M. [van Dijk]. The torch time-of-flight detector. *Nuclear Instruments and Methods in Physics Research Section A: Accelerators, Spectrometers, Detectors and Associated Equipment*, 824:106 – 110, 2016. Frontier Detectors for Frontier Physics: Proceedings of the 13th Pisa Meeting on Advanced Detectors.

[71] T.M. Conneely et al. The TORCH PMT: a close packing, multi-anode, long life MCP-PMT for cherenkov applications. *Journal of Instrumentation*, 10(05):C05003–C05003, may 2015.

[72] M Van Dijk, N. Brook, and J. Rademacker. Design of the TORCH detector: A Cherenkov based Time-of-Flight system for particle identification, Jan 2016. Presented 24 Feb 2016.

[73] Letter of Intent for the LHCb Upgrade. Technical Report CERN-LHCC-2011-001. LHCC-I-018, CERN, Geneva, Mar 2011.

[74] M. Despeisse et al. Multi-channel amplifier-discriminator for highly time-resolved detection. *IEEE Transactions on Nuclear Science*, 58(1):202–208, Feb 2011.

[75] J. Christiansen. Hptdc: High performance time to digital converter. 2004.

[76] P. Baesso, D. Cussans, and J. Goldstein. The AIDA-2020 TLU: a Flexible Trigger Logic Unit for Test Beam Facilities. *Journal of Instrumentation*, 14(AIDA-2020-PUB-2019-012. P09019), Sep 2019.

[77] T.M. Conneely, J.S. Lapington, and J. Milnes. Detector and electronics r&d for picosecond resolution, single photon detection and imaging. *Nuclear Instruments and Methods in Physics Research Section A: Accelerators, Spectrometers, Detectors and Associated Equipment*, 639(1):151 – 154, 2011. Proceedings of the Seventh International Workshop on Ring Imaging Cherenkov Detectors.

[78] F.G. Bass, I.M. Fuks, C.B. Vesecky, and J.F. Vesecky. *Wave Scattering from Statistically Rough Surfaces*. International series in natural philosophy. Elsevier Science & Technology, 1979.

[79] N.H. Brook et al. Testbeam studies of a torch prototype detector. *Nuclear Instruments and Methods in Physics Research Section A: Accelerators, Spectrometers, Detectors and Associated Equipment*, 908:256 – 268, 2018.

[80] L. Castillo Garca et al. Micro-channel plate photon detector studies for the torch detector. *Nuclear Instruments and Methods in Physics Research Section A: Accelerators, Spectrometers, Detectors and Associated Equipment*, 787:197 – 202, 2015. New Developments in Photodetection NDIP14.

[81] A.Yu. Barnyakov et al. Measurement of the photoelectron collection efficiency in MCP PMT. *Journal of Instrumentation*, 12(03):P03027–P03027, mar 2017.

[82] D.A. Orlov et al. High collection efficiency MCPs for photon counting detectors. *Journal of Instrumentation*, 13(01):C01047–C01047, jan 2018.

[83] T. Hadavizadeh et al. TORCH physics performance: improving low-momentum PID performance during Upgrade IB and beyond. Technical Report LHCb-INT-2019-006. CERN-LHCb-INT-2019-006, CERN, Geneva, Feb 2019.

[84] T.H. Hancock et al. Beam tests of a large-scale torch time-of-flight demonstrator. *Nuclear Instruments and Methods in Physics Research Section A: Accelerators, Spectrometers, Detectors and Associated Equipment*, 958:162060, 2020. Proceedings of the Vienna Conference on Instrumentation 2019.

[85] N. Harnew et al. Status of the torch time-of-flight project. *Nuclear Instruments and Methods in Physics Research Section A: Accelerators, Spectrometers, Detectors and Associated Equipment*, 952:161692, 2020. 10th International Workshop on Ring Imaging Cherenkov Detectors (RICH 2018).

[86] S. Okubo. Phi meson and unitary symmetry model. *Phys. Lett.*, 5:165–168, 1963.

[87] G. Zweig. An SU(3) model for strong interaction symmetry and its breaking. Version 2. In D.B. Lichtenberg and Simon Peter Rosen, editors, *DEVELOPMENTS IN THE QUARK THEORY OF HADRONS. VOL. 1. 1964 - 1978*, pages 22–101. 1964.

[88] J. Iizuka. A Systematics and Phenomenology of Meson Family*. *Progress of Theoretical Physics Supplement*, 37-38:21–34, 03 1966.

[89] C. Lu, Y. Shen, and J. Zhu. $B^0 \to \phi\phi$ decay in perturbative QCD approach. *Eur. Phys. J.*, C41:311–317, 2005.

[90] S. Bar-Shalom, G. Eilam, and Y. Yang. $B \to \phi\pi$ and $B^0 \to \phi\phi$ in the standard model and new bounds on R parity violation. *Phys. Rev.*, D67:014007, 2003.

[91] M. Beneke, J. Rohrer, and D. Yang. Branching fractions, polarisation and asymmetries of $B \to VV$ decays. *Nucl. Phys.*, B774:64–101, 2007.

[92] M. Bartsch, G. Buchalla, and C. Kraus. $B \to V_L V_L$ decays at next-to-leading order in QCD. 2008.

[93] A. L. Read. Presentation of search results: the CL_s technique. *Journal of Physics G: Nuclear and Particle Physics*, 28(10):2693, 2002.

[94] R. Aaij et al. Measurement of the fragmentation fraction ratio f_s/f_d and its dependence on B meson kinematics. *JHEP*, 04:001, 2013.

[95] R. Aaij et al. Measurement of the $B_s^0 \to \phi\phi$ branching fraction and search for the decay $B^0 \to \phi\phi$. *JHEP*, 10:053, 2015.